Mesoscopic disorder and intrinsic charge instability in oxide heterostructures

Niccoló Scopigno

Supervisor: **Prof. Marco Grilli**
Prof. Sergio Caprara

Department of Physics
University of Roma Sapienza

This dissertation is submitted for the degree of
Doctor of Philosophy

February 2017

Abstract

After Ohtomo and Hwang detected a high-mobility two-dimensional electron gas (2DEG) at the interface between the two insulating perovskite oxides Strontium Titanate ($SrTiO_3$) and Lanthanum Aluminate ($LaAlO_3$) [77], an increasingly intense theoretical and experimental investigation has been devoted to these systems.

Oxide heterostructures are of great interest for both fundamental and applicative reasons. In particular, the two-dimensional electron gas at the $LaAlO_3/SrTiO_3$ (LAO/STO) interfaces displays many different properties and functionalities. It can be made superconducting when its carrier density is tuned by means of a gate voltage [87, 30], thus opening the way to voltage-driven superconducting devices. Also, it exhibits magnetic properties [2, 67, 5, 37, 73, 6]; displays a strong and tunable [29, 27] Rashba spin-orbit coupling; it is extremely two-dimensional, having a lateral extension $\approx 5\,\mathrm{nm}$, thereby enhancing the effect of disorder due to extrinsic and/or intrinsic sources. Similar results hold true also for other oxides such as $LaTiO_3/SrTiO_3$ [10, 9], where the role of Lanthanum Aluminate is taken by Lanthanum Titanate $LaTiO_3$ (LTO). In these kind of systems, superconductivity is possibly related to the presence of high-mobility carriers (HMC) and low-mobility carriers (LMC), which presence is revealed by magneto-transport experiments, and seems to develop as soon as high-mobility carriers appear [9], when the carrier density is tuned above a threshold value by means of gate voltage, V_g.

Along with these intriguing physical properties, there are clear experimental indications that the interface electronic state is strongly inhomogeneous, as revealed in various magnetic experiments [2, 67, 5, 6], in tunneling spectra [89], and possibly in piezoforce microscopy [7]. It seems that inhomogeneities at nanometric scale coexist with larger (e.g., micrometric) scale inhomogeneities, revealed by the occurrence of striped textures in the current distribution [60] and in the surface potential [54].

The inhomogeneous character of the 2DEG may be responsible of the anomalously large width of the superconducting transition, which is not compatible with any reasonable superconducting fluctuations (e.g., Aslamazov-Larkin contribution to the paraconductivity) [26], but instead it is well accounted for assuming that the 2DEG consists of superconducting “puddles ” embedded in weakly localizing metallic background. This scenario could also

help to explain the measurements carried out at low carrier density, showing a saturation plateau with finite resistance, a clear signature of the percolating character of the metal-to-superconductor transition.

The aim of the present thesis is to assemble all these experimental evidences into a coherent overall theoretical framework. The outline is as follows.
In chapter 1 we review some of the experimental facts about LAO/STO and LTO/STO interface, stressing our attention on the peculiar transport properties, both in the normal and in the superconducting state.
In chapter 2 we first provide new, compelling evidences of the inhomogeneous character of the 2DEG. We consider the phenomenological assumption that the electron gas consists of a metallic sea, where only LMC are present, hosting metallic islands, where LMC and HMC coexist and become superconducting below a randomly distributed critical temperature. Basing on this idea, we extend previous multicarrier analyses of magneto-transport measurements to deal with inhomogeneous systems and show how Hall resistivity, superfluid density and tunneling spectra measurements can be explained within this scenario. The connection between superconductivity and the appearing of the high-mobility carriers is also investigated.
Chapter 3 is devoted to formulate a possible justification of the inhomogeneous scenario and the appearing of two type of carriers whose distribution is not uniform in space. The mechanism that we propose is based on the quantum confinement experienced by the 2DEG because of the strong electric field perpendicular to the interface. We will show that such an *intrinsic* mechanism is due to the fact that the confining potential well depends on the electron density, therefore giving rise to a non-rigid band structure which evolves as a function of the electron density too. In a wide range of reasonable parameters, compatible with the experiments, the non-rigidity determines a negative compressibility in the uniform system, which it avoids by phase separation. The densities of the phase separated regions are thus found by Maxwell construction and depend on the doping level. The phase separation scenario also naturally explains the inhomogeneous distribution of low- and high-mobility carriers, and their behavior as a function of the doping level.
In chapter 4 we explore the fluctuations of the superconducting order parameter in the vicinity of the metal-to-superconductor phase transition, that is reached as the gate voltage is changed. In the case of superconductivity, the order parameter has an amplitude and a phase, which can both fluctuate according to well identified scenarios. We address the possibility that a new type of fluctuations occurs in the superconducting 2DEG at LAO/STO and LTO/STO interfaces, with an anomalous dynamics. In particular, we show that the superconducting-to-metal

quantum phase transition displays anomalous scaling properties, which can be explained by density driven superconducting critical fluctuations.
Finally, the concluding remarks will be given in chapter 5. We will critically discuss the merits and limitations of our approach and provide a brief outlook on future work.

Table of contents

List of figures

Chapter 1

Overview on oxide heterostructures

In this chapter we briefly review the main features of the $LaAlO_3$/$SrTiO_3$, $LaTiO_3$/$SrTiO_3$ interfaces (generically referred as LXO/STO). Since $LaAlO_3$ (LAO), $LaTiO_3$ (LTO) and $SrTiO_3$ (STO) are insulators oxides of the Perovskite type, Perovskite structure is explained in section 1.1. According to the experimental evidence that the 2DEG resides in the Strontium Titanate side of the heterostructure, in section 1.2 we describe the band structure and the dielectric properties of $SrTiO_3$. Although the argument is still on debate, in section 1.3 we discuss the origin of the interfacial electrons, considering polarity catastrophe and the occurrence of oxygen vacancies as possible sources of the 2DEG. The remain of the chapter is devoted to the 2DEG's properties: the presence of electron inhomogeneities (section 1.4), the transport measurements (section 1.5) both in the metallic and in the superconducting state, and finally the quantum critical behavior that it is shown by the gas when driven to the metal-to-superconductor transition by an external magnetic field (section 1.6).

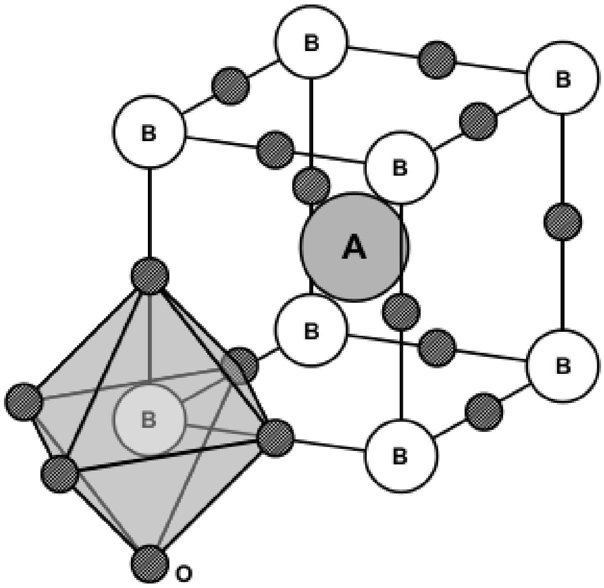

Fig. 1.1 Perovskite structure, ABO_3. Oxygen is the black filled circles (see main text).

1.1 Perovskite structure

Perovskite oxides have attracted much attention in the last decades thanks to their rich spectrum of functionalities and the possibility to achieve hight quality interfaces involving these materials. They appear as a unique system to study the coexistence of various phases, due to the competition of different interactions, enhanced by the reduction of the dimensionality. The two-dimensional electron gas (2DEG) at the $LaAlO_3/SrTiO_3$, $LaTiO_3/SrTiO_3$ (henceforth LXO/STO) interfaces is one of these new features: the 2DEG, although these compounds are insulating, shows high mobility, superconductivity, magnetic properties.

Perovskite oxides are a large family of extremely diversified compounds. Their general formula is ABC_3, A and B being cations and C is an anion. In the cases studied in this thesis, the role of the cation is played by the oxygen, so the general formula is ABO_3. The ideal structure is cubic, with B at the vertexes and A at the center of the cube. The oxygens are placed at the center of the edges, forming a octahedron around the B cations (figure 1.1). This structure is, in general, extremely ionic, the oxygen anions having a formal charge of -2 and the cations a formal charge of $Q_A + Q_B = +6$. The possible combinations are thus A^{4+} B^{2+} , A^{3+} B^{3+} , A^{2+} B^{4+} , and A^{1+} B^{5+}.

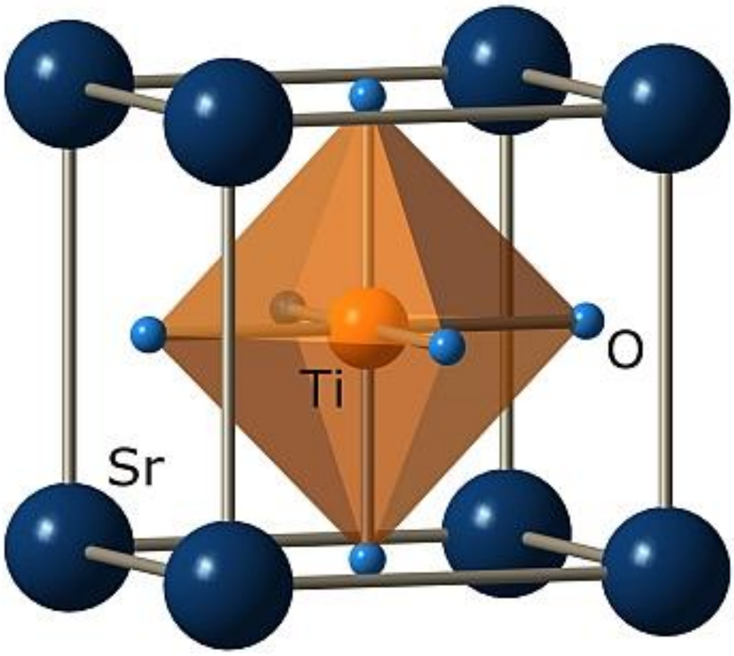

Fig. 1.2 Perovskite structure of Strontium Titanate.

1.2 Strontium titanate

Many arguments support the idea that the 2DEG at the LAO/STO interface mainly resides in the Strontium Titanate conduction band [104]. $SrTiO_3$ (STO) is a band insulator, with a large band gap of $3.2eV$. It is widely used as a substrate to grow a wide kinds of materials, ranging from high-Tc superconductors to multiferroics, because of its compatible lattice parameter, structure and relatively low chemical reactivity [61]. The Perovskite structure of $SrTiO_3$ is shown in figure 1.2.

Band structure

The valence band of the strontium titanate comes from the $2p$ orbitals of oxygen while the conduction band of comes from the titanium $3d$ orbitals [58]. Because of the crystal field, the latter split in a high energy doublet e_g and a low energy triplet t_{2g} (figure 1.3 (a)). The conduction is formed by the triplet and corresponds to d_{xy}, d_{xz}, d_{yz} orbitals. They have strong or small overlap depending on the bonding direction; for example (see figure 1.3 (b)), the d_{xy} has high overlap in the $xy-$plane and a small one along the z direction. According to that, the geometry of the conduction band is strongly anisotropic and there are two different effective masses at the Γ point: a light mass ranging from 0.5 to 1.5 m_0 and a heavy mass

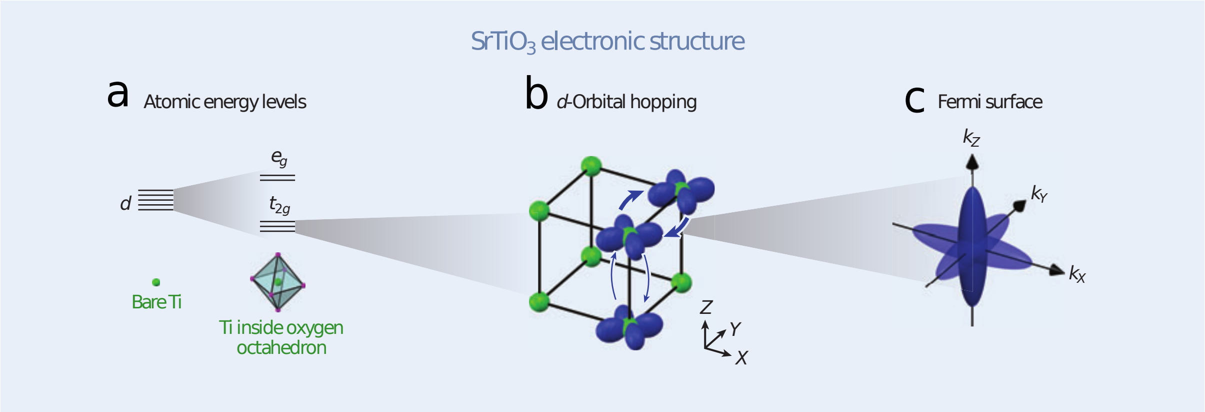

Fig. 1.3 (a) The electronic orbitals near the Fermi energy in $SrTiO_3$ are the five-fold titanium d-orbitals. Once the titanium is surrounded by the oxygen octahedron, the d-orbitals are split into a higher energy doublet (the e_g states) and a lower energy triplet (t_{2g} states). (b) Electrons located in the t_{2g} orbitals (d_{xy},d_{xz},d_{yz}) are coupled to identical orbitals on neighboring lattice sites. Hopping matrix elements are much larger in the plane of an orbital's lobes than in the perpendicular direction. This is illustrated by the thickness of the arrows which indicates that hopping between d_{xy} orbitals (blue) is stronger along the x and y directions (light effective mass) than along the z direction (heavy effective mass). (c) The corresponding Fermi surface. Figure is taken from [100].

ranging from 10 to 20 m_0. This results in a light band along the x, y directions, and a heavy band along the z direction. The Fermi surface is shown in figure 1.3 (c).

At high temperature, the cubic symmetry imposes that the three bands has the same energy at the Γ point, while at low temperature, due to a tetragonal transition and the spin orbit coupling, the degeneracy is lifted.

When the $SrTiO_3$ is used as a substrate in an heterostructure, its spectrum has to change locally in order to preserve the continuity of the wave function at the interface. Typically, the bands are bend and a quantum well is formed between the two parent compounds. In figure 1.4 (a) the band bending is sketched for a LAO/STO interface. In $LaAlO_3$ the valence band is derived from p orbitals and it has an energy that is similar to $SrTiO_3$ valence band (fig. 1.4), but the gap with the conduction band is larger. As a result, most of the band discontinuity between LAO and STO resides in the conduction band, which is lower in $SrTiO_3$.

Quantum paraferroelectric

The strontium titanate has peculiar dielectric properties. At low temperatures the $SrTiO_3$ is close to a ferroelectric transition: the stable position of the titanium atom at the center of the oxygen octahedron becomes unstable and two new energy minima develop. The material is

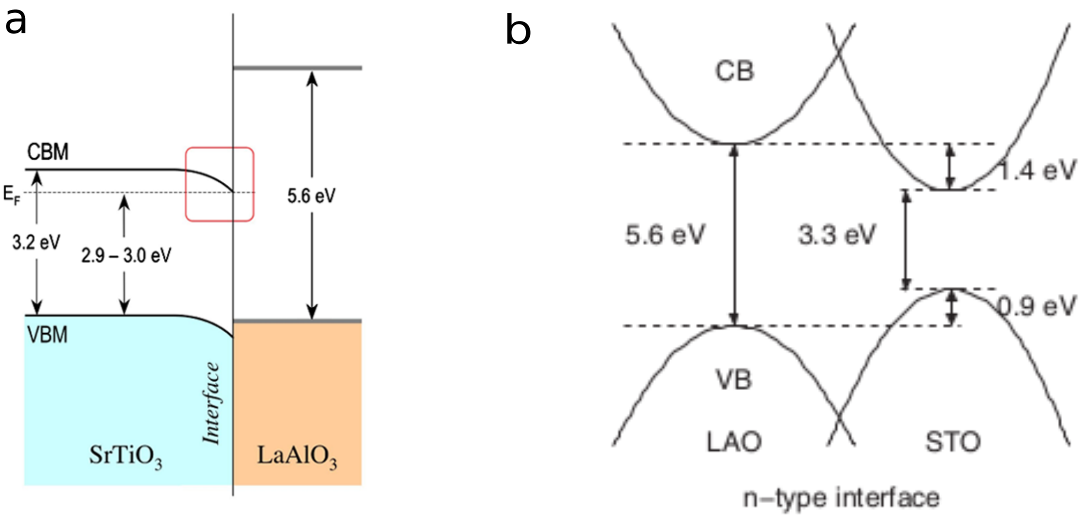

Fig. 1.4 (a) Simplified band-diagram across LAO/STO interface with band-gaps and a qualitative band bending [104]. (b) LAO and STO band-gaps and band-offsets at their interface as calculated by Popovic et al. [83].

not ferroelectric since quantum fluctuations are strong and restore the inversion symmetry. However, the remnant of this missed critical regime determines the behavior of the dielectric constant, which tends to diverge lowering the temperature, but then saturate at around 4K for values higher than 10^4. This qualify the strontium titanate as a quantum paraferroelectric.

Neville et al. [76] studied the behavior of the dielectric constant (figure 1.5) upon changing both the temperature, T, and the electric filed, E, finding a field dependence of the form

$$\varepsilon_r(E) = \varepsilon_\infty + \frac{1}{A + B|E|} \tag{1.1}$$

where, for $T \leq 4.5\text{K}$: $A = 4.097 \times 10^{-5}$, $B = 4.907 \times 10^{-10}\text{mV}^{-1}$ and $\varepsilon_\infty = 300$.

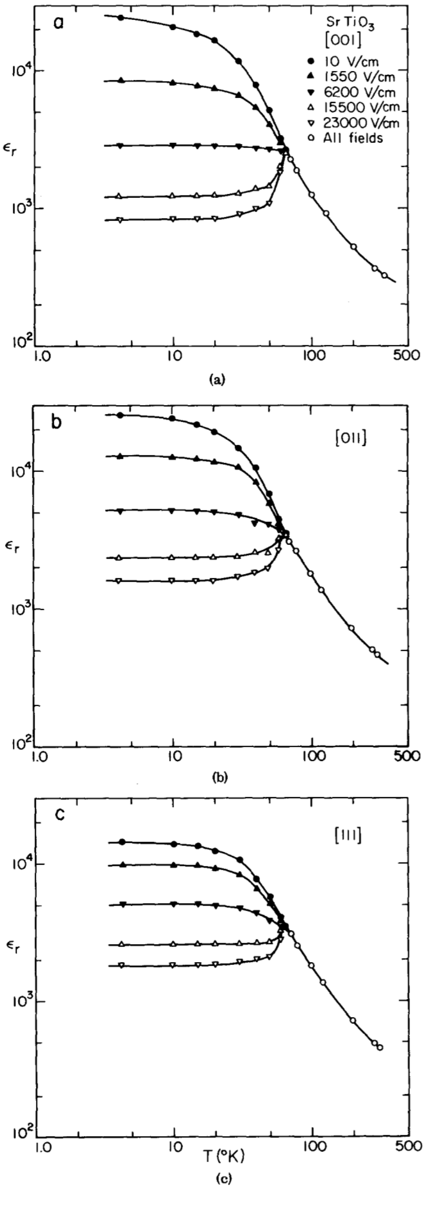

Fig. 1.5 Relative permittivity of strontium titanate as a function of temperature with applied dc bias field as a parameter: (a) [001] orientation, (b) [011] orientation, and (c) [111] orientation. Data are taken from Neville [76].

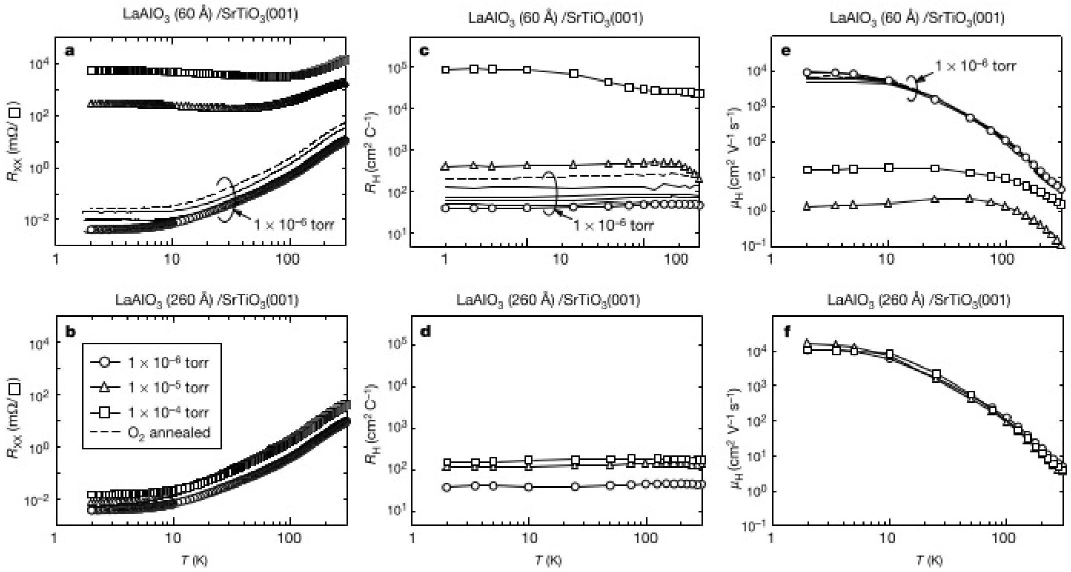

Fig. 1.6 Transport properties of the LaO-TiO$_2$ interface for different oxygen partial pressures during growth and different thickness of the LaAlO$_3$ layer. Temperature dependence of longitudinal sheet resistance $R_{XX}(T)$, Hall-resistance $R_H(T)$ and mobility $\mu(T)$ for two different thickness of the LaAlO$_3$ layer [77].

1.3 Origin of the gas: extrinsic and intrinsic mechanism

The origin of the interfacial electrons is still controversial. Experiments point out basically two possible sources of charge carriers: the introduction of oxygen vacancies and a surface reconstruction due to the different polarity of the former materials. Both mechanisms can be present on a certain sample, even simultaneously, depending on the growth conditions. However, since which of the two dominates will not affect our calculations nor the validity of the scenario presented in this thesis, we shall not describe them in too much detail, limiting our discussion to the easiest case of a [001] sample. The interested reader can find more informations about polarity catastrophe in [75] and the occurrence of oxygen vacancies in [31, 34, 36]. Other interesting informations about the origin of the gas can be found in [105].

We have already shown that Perovskite oxides have a general formula ABO$_3$. Along the cubic axis [001] they can be seen as an alternate stack of AO and BO$_2$ planes. Depending of what kind of planes goes to form the interface (AO- or BO$_2$-type) between the two constituent compounds, different heterostructures are obtained. When an overlayer of LAO is used, two kind of LAO/STO interfaces are possible (figure 1.7), the TiO$_2$-LaO or the SrO-AlO$_2$ terminated. We call them *n-* and *p-type* interfaces respectively, and transport experiments show that *n-type* interface is conducting while the *p-type* is insulating. For the SrTiO$_3$-LaTiO$_3$ (LTO/STO) there is only one configuration, the *n-type* SrO-TiO$_2$ interface. Moreover the

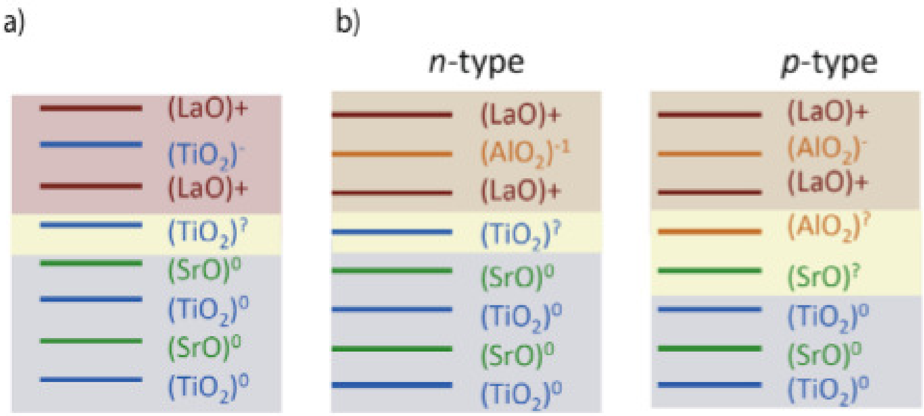

Fig. 1.7 Schematic picture of the valence discontinuity at the (**a**) $LaTiO_3$-$SrTiO_3$ interface, as well as at the (**b**) *n*- and *p*-type interfaces in $LaAlO_3$-$SrTiO_3$ [82].

conduction properties of the gas are greatly enhanced if the sample is grown at low oxygen pressure, a signal of the importance of the oxygen vacancies: this is a well-known mechanism to dope n-type the bulk $SrTiO_{3-x}$ since the valence of oxygen is -2 and its vacancies behave like donor impurities, and this is what we called *extrinsic mechanism*. However, there is another process that is responsible of the electrons in the gas, that is the *intrinsic mechanism*. It is the most important one as soon as the LXO layer is thick enough and the dependence of the conductivity on the oxygen pressure becomes less relevant. Transport properties of the $TiO_2 - LaO$ interface are reported in figure 1.6 for different oxygen pressures of growth and for different width of the LAO overlayer. We can also note that for thinner layer and hight pressure there is no significant conductivity. These experimental evidences can be explained if we assume that for low oxygen pressure the majority of the electrons of the 2DEG come from the extrinsic donors, represented by the oxygen vacancies, while for high oxygen pressure some other mechanism of interface reconstruction takes place, possibly driven by the polarity discontinuity and the inversion symmetry breaking. The latter mechanism was called *polar catastrophe* first by Nakagawa et al. [75].

1.3.1 Oxygen vacancies

Oxygen vacancies in $SrTiO_3$ can act as electron donors [59]. Each oxygen vacancy nominally provides two electrons since one oxygen atom binds two electrons. The energetic barrier for the formation of oxygen vacancies is quite low as compared for example to defects in semiconductors, and their formation could be further enhanced by electric fields near the interface. The relevance of this mechanism has been demonstrated by several experiments. In [94] the authors show that the large charge density initially observed at these heterointerfaces

($\sim 10^{17}$ el./cm^2) is due almost certainly to oxygen vacancies in the $SrTiO_3$ substrate. This hypothesis is also supported by experiments on LAO/STO interfaces where the LAO layer is grown at low oxygen pressure ($P_{O_2} \sim 10^{-6}$ mbar). The authors of reference [53] report that the high-mobility transport properties of LAO/STO sample grown at low oxygen pressure are due to a conducting region homogeneously extending over hundreds of µm inside the STO substrate. Further, the similarity between the transport properties of LAO/STO samples exhibiting high mobility ($P_{O_2} \sim 10^{-4}$ mbar) and those of reduced STO bulk single crystals, suggests that the high mobility of LAO/STO samples arises, at least to some extent, from the doping of STO with oxygen vacancies.

1.3.2 Polarity catastrophe

The LXO/STO heterostructures can be viewed as a stack of planes with different polarity, as shown in figure 1.7. In these compounds charge neutrality is conserved in the unit cell, but not necessarily in each layer, depending on the valence of the ions. At the interface a discontinuity can occur, since the polarity of the planes at the two sides usually is not the same. For example, in the case we are considering, the formal valences of the ions are $Sr^{2+}Ti^{4+}O_3^{2-}$,$La^{3+}Al^{3+}O_3^{2-}$ and therefore at their interfaces there is an abrupt change from the charge-neutral sheets $(SrO)^0$ and $(TiO_2)^0$ of $SrTiO_3$ to the alternating $\pm e-$charged sheets $(LaO)^+$ and $(AlO_2)^-$ or $(LaO)^+$ and $(TiO_2)^-$ of the $LaAlO_3$ and $LaTiO_3$ respectively. The discontinuity can induce free carriers at the interface. For example, at the TiO_2-LaO layer there would be an extra half electron per unit cell as the interfacial $(LaO)^+$ plane, which in the bulk has two $(AlO_2)^-$ neighbor planes, at the interface is between one $(AlO_2)^-$ and one $(TiO_2)^0$. Similarly, the SrO-AlO_2 interface should present an extra half a hole per unit cell. However, this simple scenario does not account for the dependence of the conductivity on the oxygen pressure, nor the fact the n-type junction is conducting and the p-type is insulating. To explain this, we have to investigate the role of the electrostatic boundary conditions, that is given, in this case, by the abrupt polarity discontinuity between the polar $LaXO_3$ and the non-polar $SrTiO_3$. Nakagawa and his team [75] pointed out the importance of electrostatic boundary conditions in controlling the atomic and electronic structure. They show how the abrupt interface between neutral and charged planes produces an electric field oscillating between a finite value and zero in the polar layer $LaXO_3$. The average field therefore turn to be different from zero and leads to a potential that increases monotonically with the thickness of the $LaXO_3$ layer. According to Nakagawa, to maintain finite the electric potential, avoiding this “polar catastrophe” that gives an unbearable cost in electrostatic energy, the interface undergo a certain surface reconstruction. The idea of a reconstruction that interest the interface of a heterostructure is not totally new: since many years physicists know that in semiconductor heterostructures (e.g GaAs-Ge), systems that shares similarities with oxide interfaces, a compensation of the polar discontinuity is often achieved through an atomic reconstruction, where the interface chemical composition is strongly altered via ordering of defects or roughening. The main difference between semiconductor and oxide heterostructures resides in the much richer possibilities of the latter to compensate the valence mismatch. For example they can prevent the polar catastrophe via an electronic reconstruction, without alter the chemical composition of the interface, transferring extra charge from the $LaXO_3$ side to the interfacial plane of $SrTiO_3$. The extra charge is half an electron per unit cell if the interface is TiO_2-LaO or half a hole if the interface is SrO-AlO_2.

In figure 1.8 the n-type LAO/STO interface, before the electronic reconstruction and after the reconstruction, is depicted. This scenario accounts for the dependence of the conductivity on the thickness of the LXO sample. In fact, two different competing effects act to determine whether the electronic reconstruction takes place: the energetic cost due to the polar catastrophe and the energy required to change the valence of titanium from +4 to +3. While the first is proportional to the volume Sd of the $LaXO_3$ layer, S and d are the surface and the width of the LXO respectively, the latter is proportional only to the surface S of the sample. If the LXO layer is thin enough, the electronic reconstruction is no longer energetically convenient and the system does not need to move charges from the LXO side to the STO side. In this case the origin of the gas can reside only in the oxygen vacancies; if they are not introduced (that is the LXO sample is grown in hight oxygen pressure) the interface remains insulating. Another remarkable feature of the argument of Nakagawa is the explanation of the difference between the n-type conducting and the p-type insulating interfaces. In fact, in the first case the extra half-electron can be accommodated at the titanium sites of the interfacial plane $\mathrm{Ti}O_2$ with the reduction of Ti from Ti^{4+} to Ti^{3+}. On the other hand, in the latter case the extra half-hole cannot in practice be transferred as there are no other valence states available and the interface remains insulating. In this case an atomic reconstruction, similar to that observed in some semiconductor heterostructures such as GaAs-Ge, is needed to avoid the potential divergence; the result is an atomic disordering and a stoichiometry change at the interface.

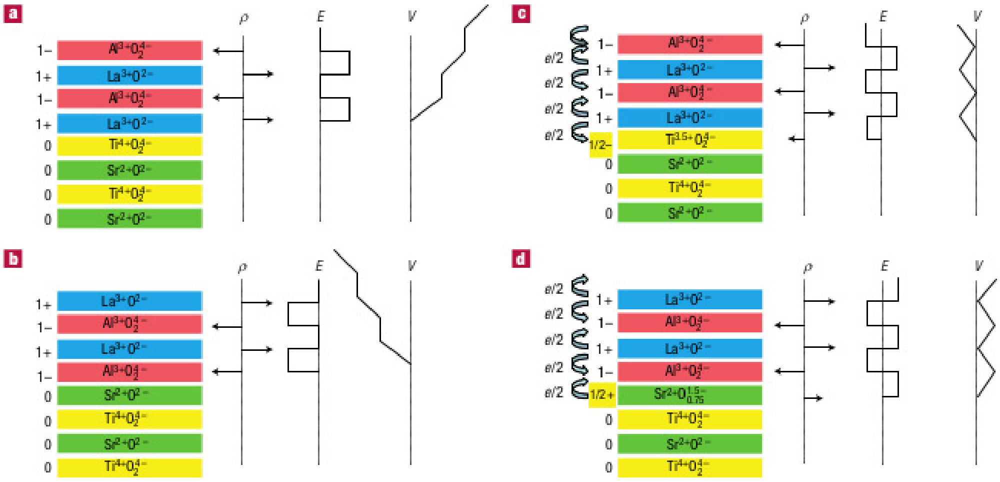

Fig. 1.8 **The polar catastrophe illustrated for atomically abrupt (001) interfaces between $LaAlO_3$ and $SrTiO_3$** . (**a**), The unreconstructed interface has neutral (001) planes in $SrTiO_3$, but the (001) planes in $LaAlO_3$ have alternating net charges (ρ). If the interface plane is AlO_2 /LaO/TiO_2 , this produces a non-negative electric field (E), leading in turn to an electric potential (V) that diverges with thickness. (**b**) If the interface is instead placed at the AlO2 /SrO/TiO2 plane, the potential diverges negatively. (**c**), The divergence catastrophe at the AlO_2 /LaO/TiO_2 interface can be avoided if half an electron is added to the last Ti layer. This produces an interface dipole that causes the electric field to oscillate about 0 and the potential remains finite. The upper free surface is not shown, but in this simple model the uppermost AlO_2 layer would be missing half an electron, which would bring the electric field and potential back to zero at the upper surface. The actual surface reconstruction is more complicated. (**d**), The divergence for the AlO_2 /SrO/TiO_2 interface can also be avoided by removing half an electron from the SrO plane in the form of oxygen vacancies [75].

1.4 Electron inhomogeneities

Ariando et al. [2] measured the magnetization as a function of temperature and cooling condition (fig. 1.9). The magnetization is positive, denoting a paramagnetic response, when the sample is cooled in a non-vanishing magnetic field (field-cooling), but it is negative if the magnetic field is zero during the cooling (zero-field-cooling) like diamagnetic systems. Moreover a ferromagnetic response, superimposed to both the paramagnetic and diamagnetic ones, is evidenced by hysteresis loops. These magnetization measurements were combined with magnetoresistance measurements for different directions of the magnetic field, showing the presence of ferromagnetic regions which act as scattering centers for a quasi-two-dimensional electron gas. The ferromagnetic behavior persists above room temperature and, below $60K$, it coexists with a superconductor-like diamagnetic/paramagnetic response. Figure 1.11 reports a direct imaging of the interface magnetization and susceptibility, as measured by Bert at al. [5]. It shows that the system is separated into different regions where ferromagnetism appears as many static spatially separated in-plane dipoles, which have no temperature dependence, embedded in a uniform paramagnetic metallic background. Experimental evidences have been found, demonstrating that the dipoles are not point-like but are instead ferromagnetic patches whose extent is below the experimental resolution. This scenario persists from below the superconducting transition temperature to up to $200K$, while low temperatures are characterized by a non-uniform weak diamagnetic susceptibility due to superconducting electrons that screen the local applied field. This indicates the existence of a two-dimensional superconductor at the interface and a ferromagnetic landscape in the background. The space-resolved image of the electronic phase separation at the interface also shows that the superconductivity is weak and inhomogeneous and it is replaced, above the critical temperature, by a paramagnetic behavior; it may indicate the presence of a first order phase transition. However there is no evidence of a direct correlation between the spatial inhomogeneities of the superconducting state and the distribution of magnetic regions.

The phase separation scenario, in which states at different densities coexist, may also explain the experimental difficulties in determining the real amount of charge transferred from LAO to LAO/STO interface. Measures of transport and capacitance [7, 9] find a value of order $n_0 \sim 0.02$ electrons per unit cell, instead of the theoretical 0.5 [el./u.c.] predicted by the polar catastrophe. However, they both may not be able to account for localized electrons which are compensated from a local charge reconstruction [1].

---

[1] Besides that, the theoretical value of 0.5 [el./u.c.] is expected for thick LAO and STO samples, much thicker than those commonly used in experiments, which is only few unit cells. Since the charge transfer has an energy cost, it may be convenient to the system to compensate the polar catastrophe (that is reduced by the finite size of the samples) using only a smaller amount of charge.

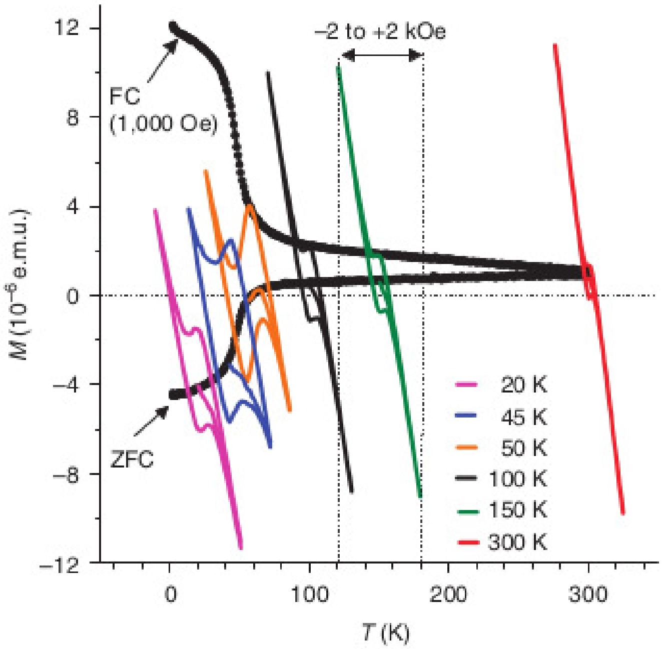

Fig. 1.9 Magnetization of the interface SrTiO3 -LaAlO3 as a function of temperature. In field-cooling (FC) condition the response is paramagnetic,whereas for zero-field-cooling (ZFC) the response is diamagnetic. Superimposed to these behaviors, there is a ferromagnetic response as evidenced by hysteresis-loops (not shown for FC) [2].

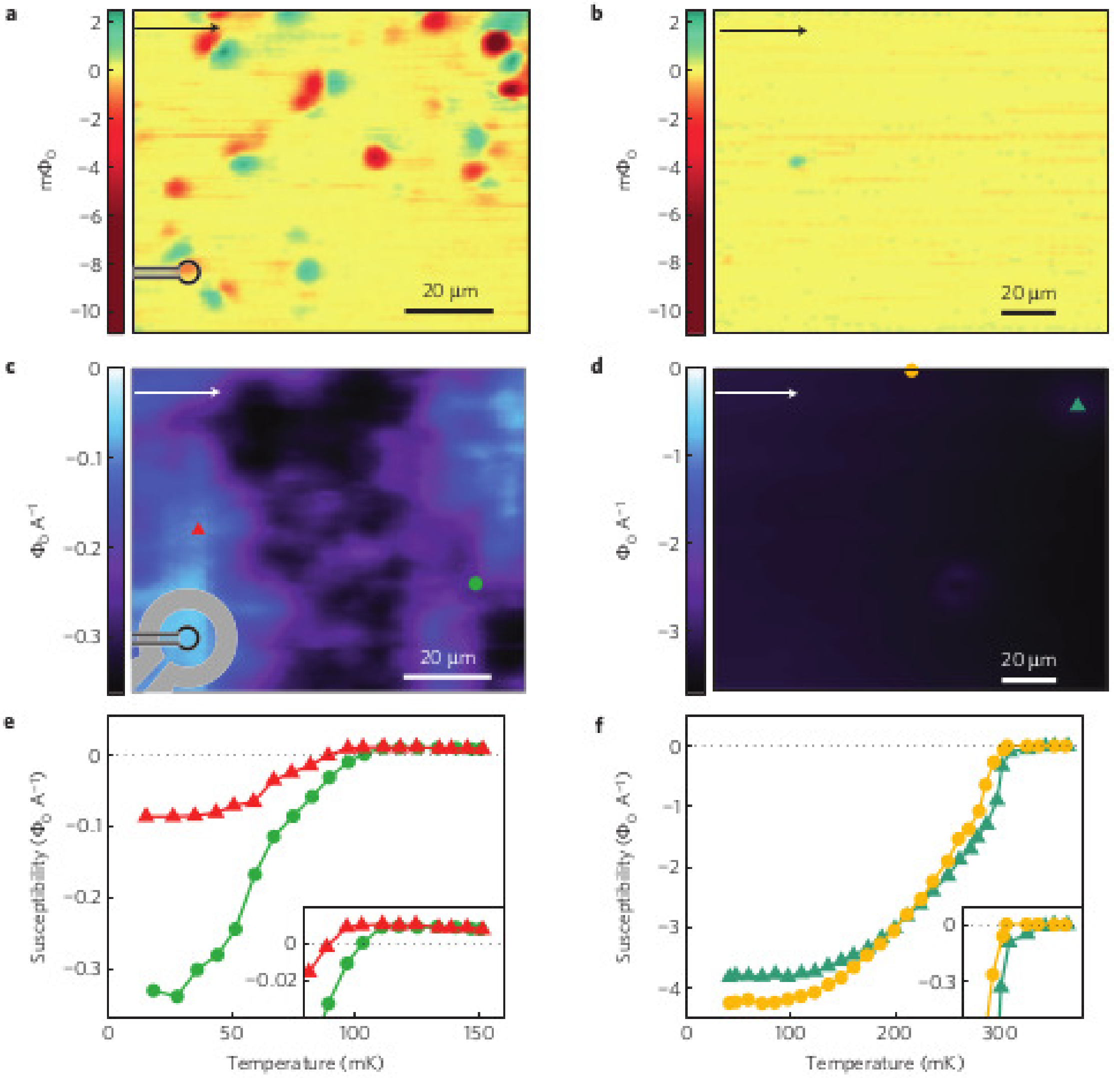

Fig. 1.10 Comparison of SQUID images on LaAlO$_3$-SrTiO$_3$ interface and δ-doped SrTiO$_3$ samples. (**a**), LAO-STO magnetometry image mapping the ferromagnetic order. (**b**), δ-doped STO magnetometry image showing no ferromagnetic order. (**c**), LAO/STO susceptibility image mapping the superfluid density at 40mK. (**d**), δ-doped STO susceptometry image mapping the superfluid density at 82mK. (**e**), The temperature dependence of the susceptibility taken at the two positions indicated in (**c**). (**f**), The temperature dependence of the susceptibility taken at the two positions indicated in (**e**).

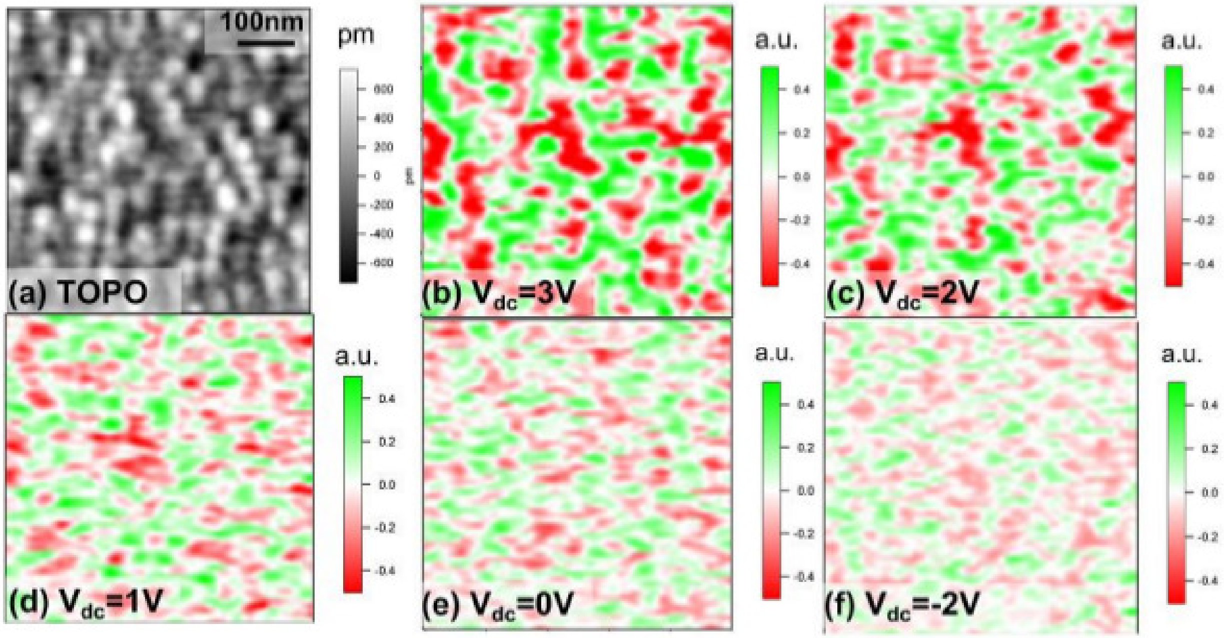

Fig. 1.11 Spatially-resolved dual frequency PFM images show inhomogeneity at interface. The height image (a) and corresponding PFM images (b-f) are shown at bias values V_{dc} =(b) 3V, (c) 2V, (d) 1V, (e) 0V (f) -2V with the mean value 4.24 a.u., 3.10 a.u., 1.91 a.u., 0.82 a.u., 0.35 a.u. subtracted. Scan size 500 nm × 500 nm [7].

1.5 Transport experiments and electrostatic tuning of the 2DEG

A remarkable feature of the 2DEG in LXO/STO interfaces is the possibility to control its transport properties through an external electric potential, applied by means of a back-gating electrode on the STO side or a top gating in the LXO side. The gating acts by changing the density of charge in the EG, which is increased for positive voltages and decreased for negative ones; but it also modifies the boundary conditions that the potential well, which results from the band bending of the STO bulk spectrum at the interface (see figure 1.4 (a)) and it is responsible of the quantum confinement of the 2DEG, has to match in order to satisfy the equation of electrostatic[2]. Experimental evidences [9] show that both the total amount of carriers and the shape of the well in which they are trapped are important to define the transport properties of this 2DEG.

Since the first observation of a conductive layer by Ohtomo et al., the transport properties of the 2DEG have been extensively studied, showing how a metal-to-insulator[3] transition, or even a superconducting-to-metal one, can be induced in the system just by changing the external gate voltage. In this section we will review some of these evidences to motivate the percolative model introduced in chapter 2.

Metallic conductivity and Hall measurements

In figure 1.12(b) (black continuous line) the sheet resistance R_s, measured by Biscaras et al. [9], is plotted as a function of the back gating V_G. As expected, the gas is more conducting since electrons are added, and the curve decreases in V_G. But then, around $V_G = 0$, a kink in the resistance appears, a behavior that is not compatible with a simple Drude model where the resistance only depends smoothly on the density of carriers. In order to explain the anomalous dependence of the resistance from the doping, *Biscaras et al.* made also Hall-effect measurements at low temperature ($\sim 20\,\mathrm{mK}$) and high magnetic field (45T), and found that the Hall resistance is linear only for negative V_G, but not for positive V_G, as shown in figure 1.12 (a). In the latter case two distinct slopes are evident, at low and high fields, respectively. Eventual non-linearities due to measurement errors such as a misalignment of voltage contacts in the setup can be excluded from the linear dependence around zero field B (B $\in [-2,2]$T). Biscaras et al. proposed that the appearance of a non-linear behavior is

---

[2] The role of the gating on the quantum well will be explained in chapter 3, where the local spectrum of the 2DEG is calculated.

[3] Actually, the system is driven from a metallic phase to a weakly localizing one. It becomes insulating only at very low doping.

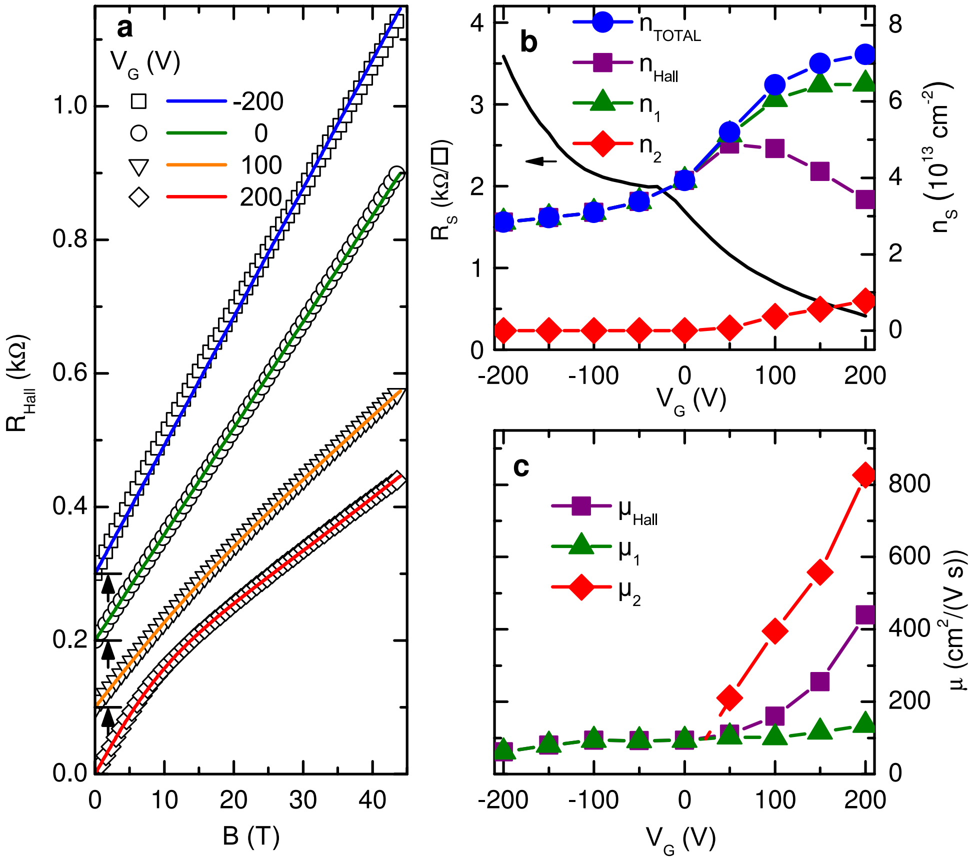

Fig. 1.12 **(b)**: Resistance, density of total charges (n_s), LMC (n_1), HMC (n_2), and apparent (n_{Hall}) of the 2DEG, calculated by analyzing the Hall effect at high field in a model with two types of carriers. **(c)**: Mobility of LMC (μ_1), HMC (μ_2) and apparent (μ_{Hall}) [9].

associated with the appearance two types of charge carriers with different mobility, that are both present in the 2DEG but in different proportions, n_1 and n_2 respectively. They called these carriers low mobility carriers (LMC) and high mobility carriers (HMC). HMC and LMC could explain the non monotone curve of the apparent number of carriers n_{Hall} in figure 1.12 (a), that is not compatible with only one electric carrier for the gas (instead, as expected for electrostatic doping, the total number of carriers $n_{total} = n_1 + n_2$ rises monotonically with V$_g$).

Indeed, fitting the Hall resistance with a two-band model[4] (colored curves in figure 1.12(a)) yields good agreement with the experimental data. As reported in figures 1.12(b) and 1.12(c), the LMC carriers (with a low and constant mobility $\mu 1$) are present for all gate biases. In contrast, a few HMC (with a mobility $\mu 2$ increasing linearly with bias) show up for positive V$_g$ only, as also observed by Kim et al. [62]. The question of what are the states only accessible at positive gating (and thus higher in energy than the states already accessible at VG = 0) is still debated. Biscaras et al. sustain that both LMC and HMC correspond to d$_{xy}$ electrons. According to their interpretation the HMC have a rather 3D character and are therefore less sensitive to disorder. In contrast, the LMC are located very close to the interface, with a pronounced 2D character and therefore more subject to localization. While this interpretation is surely sound, many theoretical and experimental works report the emergence of new physics as soon as the heavier d$_{xz}$, d$_{yz}$ start to be filled [42, 57, 47, 4]. Consequently, the HMC might be associated with these anisotropic bands, too.

1.5.1 Hysteresis and trapped charges

The presence of HMC could explain the hysteretic behavior (fig. 1.13) of the resistance as a function of the gate voltage, when the samples are cooled starting from $V_g = 0$ and then V_g is changed. In fact, while the total number of carriers is not increased during the first polarization, a small amount of HMC is injected into the gas (fig. 1.14), whose mobility is highly dependent on the gate voltage (fig. 1.15) around $V_g = 0$, but saturates as V_g is increased. Once the maximum value of V_g is reached, the voltage is decreased and the hysteretic behavior appears both in the resistance and in the total (partial) number of carrier. *Biscaras* explains the evaporation of the charge as the result of the bending of the confining potential due to the applied positive voltage (figure 1.16): when the sample is cooled at zero voltage, the well is almost filled by the 2DEG. As soon as the voltage is increased, more electrons are added to the gas. However, they cannot remain confined in the well, but escape towards the STO bulk exceeding the potential barrier. Biscaras assumes that a static distribution of trapped charges result from these electrons, since they fill some deep (or localized) levels in the STO sample, due to impurities or defects.

While a complete description of the escaping mechanism during the doping procedure is reviewed in detail in reference [11], the role of trapped charges will be investigated better in

---

[4] The Hall resistance in a two-carriers model is

$$R_{Hall} = \frac{B}{e}\,\frac{\frac{n_1\mu_1^2}{1+\mu_1^2B^2}+\frac{n_2\mu_2^2}{1+\mu_2^2B^2}}{\left[\frac{n_1\mu_1}{1+\mu_1^2B^2}+\frac{n_2\mu_2}{1+\mu_2^2B^2}\right]^2+\left[\frac{n_1\mu_1^2B}{1+\mu_1^2B^2}+\frac{n_2\mu_2^2B}{1+\mu_2^2B^2}\right]^2} \tag{1.2}$$

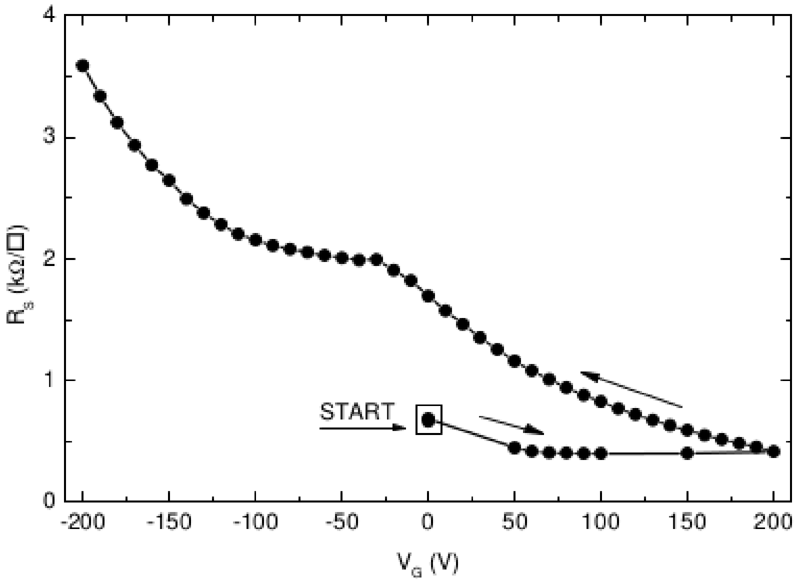

Fig. 1.13 Resistance of the 2DEG as a function of the gate voltage after a zero-voltage cooling of the samples [9].

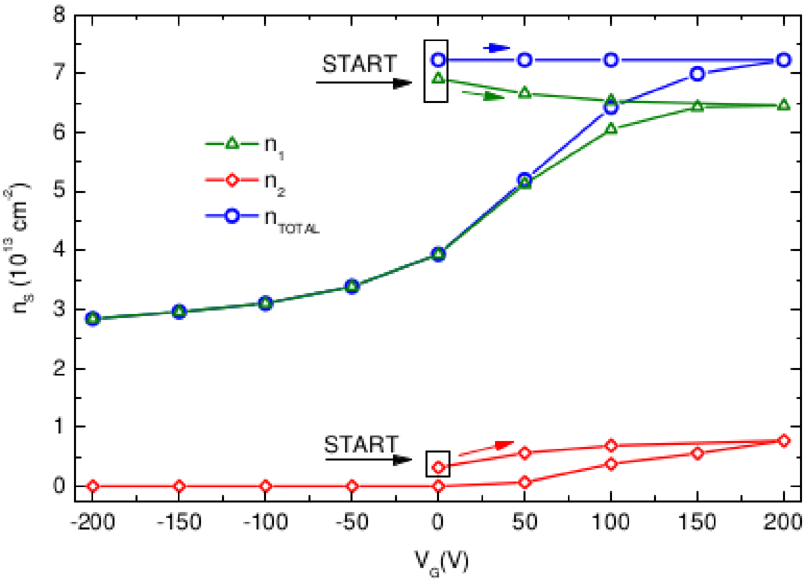

Fig. 1.14 Density of HMC, LMC and total number of carriers measured by Hall-effect experiments [9].

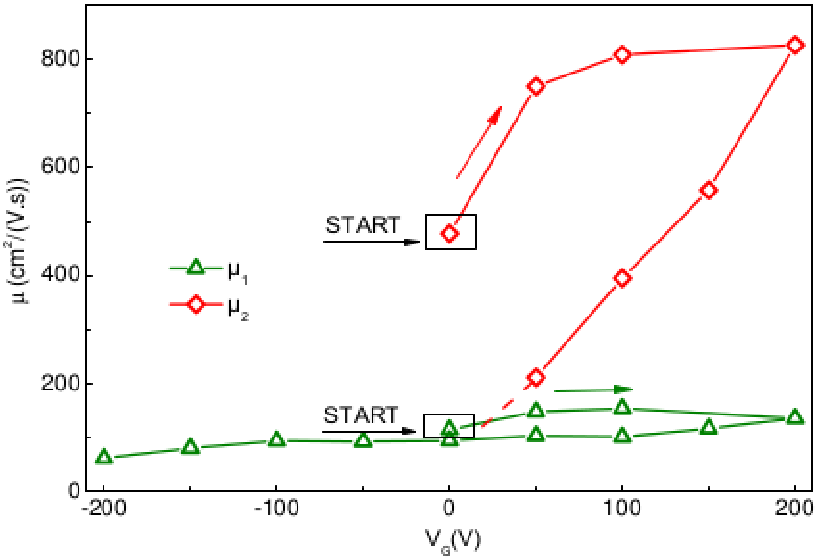

Fig. 1.15 Mobility of HMC, LMC and total number of carriers measured by Hall-effect experiments [9].

chapter 3, as they are essential to ensure the numerical convergence of the self-consistent calculation of the potential well.

1.5.2 Superconductivity

In figure 1.17 we report the measurements, made by Biscaras et al. [9], of the sheet resistance as a function of both gate voltage and temperatures[5]. At low temperature, superconductivity takes place with a maximum critical temperature T_c of about 200 mK, and signatures of superconducting fraction are seen well above the temperature at which the global zero resistance state is reached. This happens only for a large enough doping level: by decreasing V_g, the superconducting fraction is continuously reduced to a value such that the resistance stays finite down to the lowest measured temperatures. For negative voltages, when in the low density regime, the superconducting fraction eventually disappears and the 2DEG stays metallic at all temperatures and seems to undergo weak localization at low T. Finally, at yet smaller carrier densities the system behaves as an insulator. The suppression of the superconducting state seems to be correlated to the singular behavior of the normal resistance state around $V_g = 0$, indicating that the doping process modifies deeply the electronic properties of the 2DEG.

---

[5] The sample is the same used to perform the Hall measurements of figure 1.12.

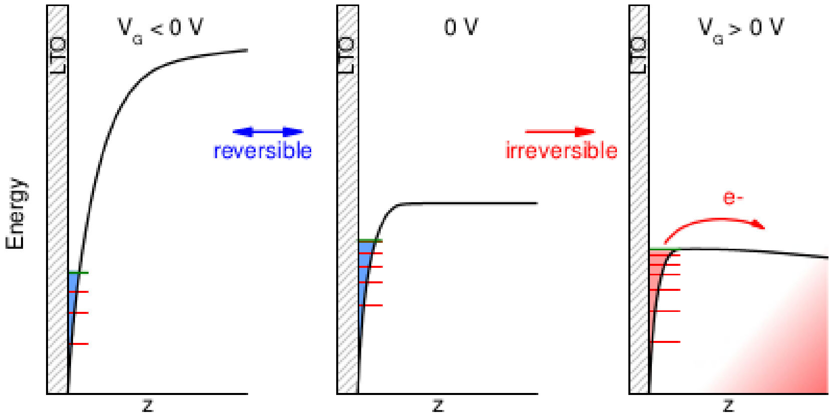

Fig. 1.16 Schematic picture of the mechanism followed by the electrons to escape the confining potential. (Center): quantum well at the LAO/STO interface when the samples are cooled at zero-gating voltage. The Fermi level is almost on the top of the well. (**Right**): irreversible escaping of the electrons towards the $SrTiO_3$ side when a positive voltage is applied to the gate. (**Left**): a negative polarization of the gate electrode does not cause the fugue of the electrons and the polarization is reversible [9].

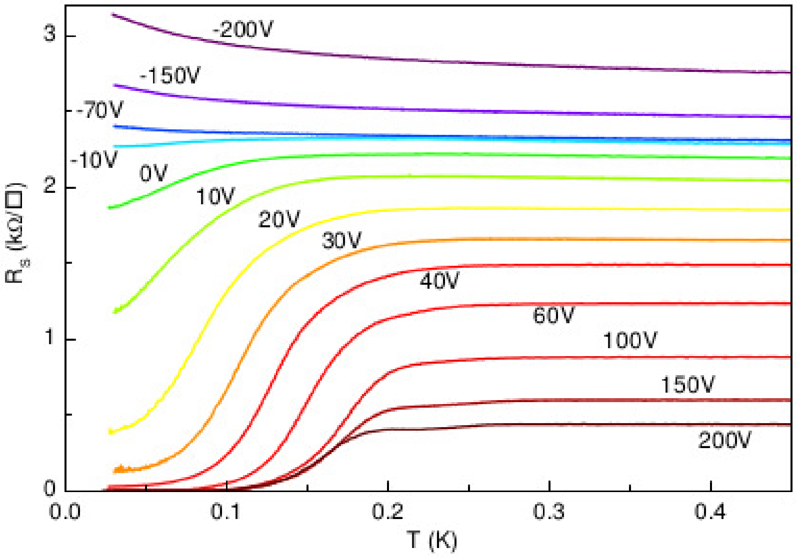

Fig. 1.17 The resistance of the LTO sample as function of the temperature, for different gate voltages [9].

The analysis of the magnetic critical field [10] evidences the strong two-dimensional character of the superconducting 2DEG, which has a typical thickness, th, smaller than 10 nm, in agreement with self-consistent calculations of the electronic states in the quantum well formed at the interface (see [9, 92] and chapter 3), and a superconducting coherence length of $\xi \sim 40-70\,\mathrm{nm}$ ($th < \xi$). With a Fermi energy in the $100-150\,\mathrm{meV}$ range [9, 72], the Fermi wavelength is $\lambda_F \sim 10\,\mathrm{nm}$, that is slightly greater than the extension of the well ($\lambda_F \geq th$). This 2DEG is therefore an extreme 2D superconductor, with an electronic sub-band structure due to confinement. As the doping is changed electrostatically, the superconducting critical temperature T_c is modulated, and shows a dome-like dependence with gate voltage V_g, ending with a quantum critical point (figure 1.19).

Owing to its low dimensionality, one expects that disorder plays an important role in the physics of this system. In particular, the evidences of inhomogeneities in the 2DEG at LXO/STO interfaces suggest that it may share some common behavior with other 2D superconductors, such as homogeneously disordered films of conventional superconductors of TiN or NbN. However, while the latter present rather sharp transitions with high slopes of $R(T)$ around T_c, LXO/STO heterostructures commonly display broad transitions even for relatively small values of the normal-state resistance. In figure 1.18 the typical shape of $R(T)$ is sketched schematically, showing how the downturn of $R(T)$ toward zero is characterized by a linear regime with a relatively small slope. The width of the transition can be estimated approximately as $\Delta T_c/T_c \simeq (T_h - T_l)/T_l$, where the two scales T_l and T_h are defined as in figure 1.18. In their paper, Caprara et al. shown that the typical width of the superconducting transition in metal-oxide interfaces is substantially larger that the width of standard disordered films, which attain values comparable to those reported for the interfaces only at extremely large disorder concentration, where also the critical temperature is driven to zero [26]. To explain this anomalously tailish resistance curves, Caprara et al. noted that that such broad transitions in the 2DEG can hardly be ascribed to ordinary superconducting fluctuations. Indeed, considering the Aslamazov-Larkin contribution of superconducting fluctuations, which is a universal quantity in two dimensions and accounts for the the paraconductive corrections above T_c, one finds that ordinary superconducting fluctuations would give a $\Delta T/T_c$ are at least an order of magnitude smaller than the experimental one. This suggest [26] that in heterostructures these large transition widths and persisting tails arise from mesoscopic inhomogeneities and the superconducting transition is someway related to the physics of a percolative system. We anticipate that the scenario of an inhomogeneous superconducting state at oxide interfaces, that will be explored in more detail in chapter 2, is also supported by the recent analysis of the quantum critical behavior that is observed when

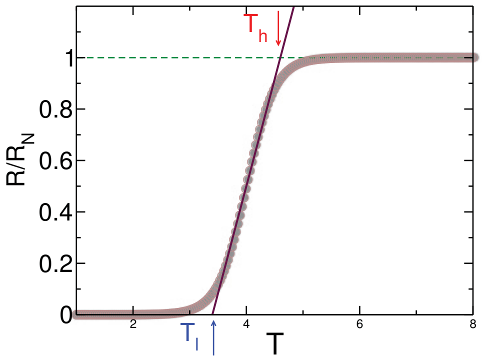

Fig. 1.18 Sketch of the typical resistance curve for a superconducting interface (circles). The width of the transition can be estimated as $\Delta T_c/T_c \simeq (T_h - T_l)/T_l$. A pronounced tail is present also below T$_l$. Figure from [26].

the superconducting phase is suppressed by means of a magnetic field perpendicular to the interface[8]. This aspect is the topic of the next section.

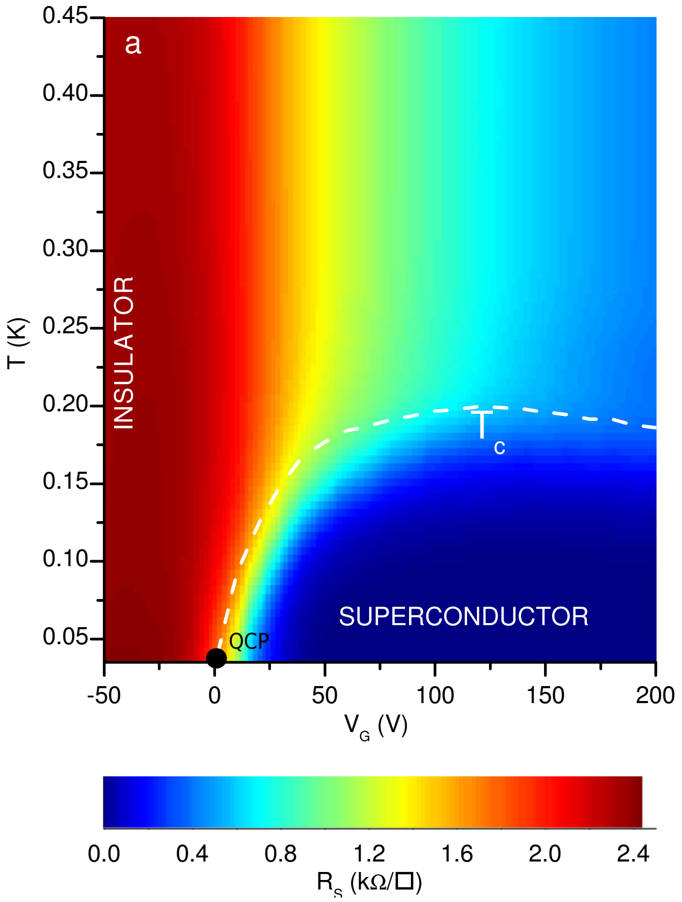

Fig. 1.19 Superconducting transition as a function of gate voltage for a LTO/STO sample [9]. The quantum critical point (QCP) is marked by a black dot.

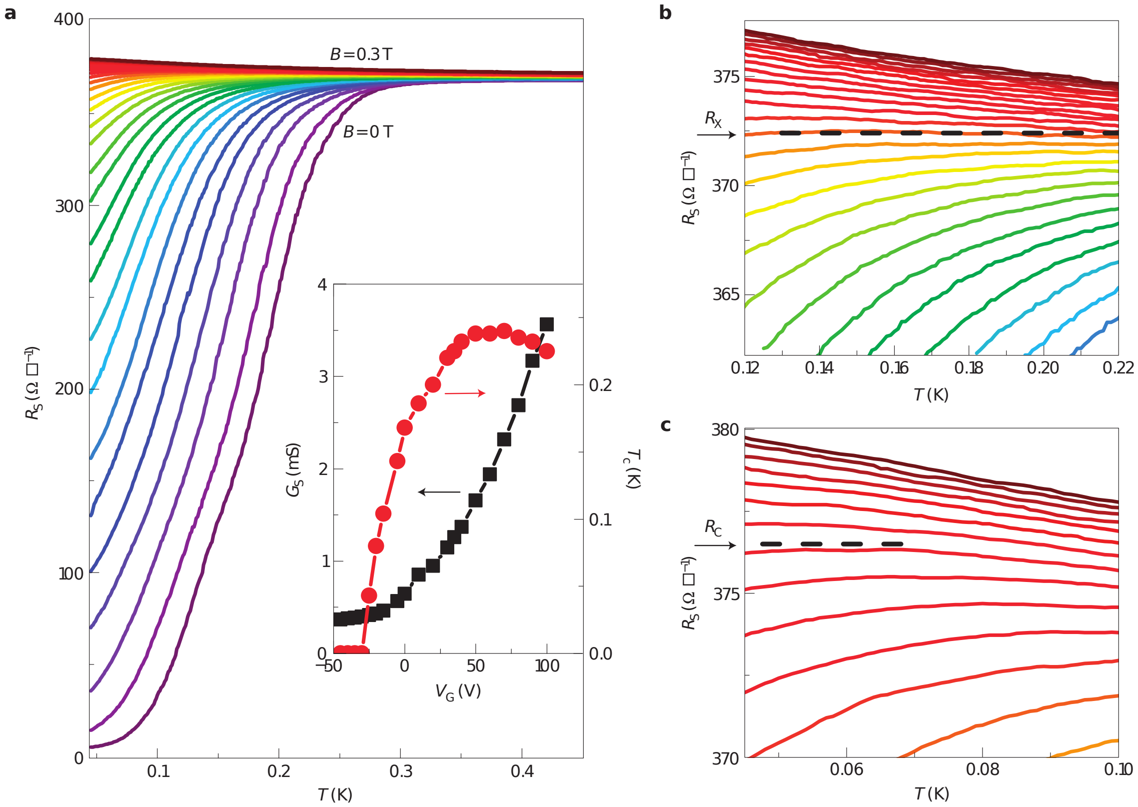

Fig. 1.20 (a)Sheet resistance R_s as a function of the temperature, for different perpendicular magnetic field. The gating is $V = 80\,\mathrm{V}$. Inset: critical temperature T_c and conductivity $G_s = 1/R_s$ as a function of the gate voltage.(b,c) Zoom of the same data. Figures from Biscaras et al. [8].

1.6 Multiple quantum criticality

Quantum critical regime develops in the vicinity of a zero temperature phase transition, where the role of temperature in driving the transition is taken by a control parameter in the Hamiltonian (e.g the external magnetic field). In figure 1.20 (a) the sheet resistance R of a LTO/STO sample is plotted as a function of temperature, for different perpendicular magnetic field [8]. A low temperature (figure 1.20 (b)) and a high temperature (figure 1.20 (c)) regimes are then identified. In each of them, depending on whether their derivative is positive or negative, the resistance curves are clearly separated in two classes by a line of constant resistance $\overline{R}$ (marked by a dashed line), which occurs at some magnetic field $\overline{B}$. The resistance $\overline{R}$ is equal to R_x when the temperature T is in the interval $T \in [0.12, 0.22]$ K and the field is $\overline{B} = B_x$, and it is equal to R_c when $T \in [0.04, 0.10]$ K and the field is $\overline{B} = B_c$.

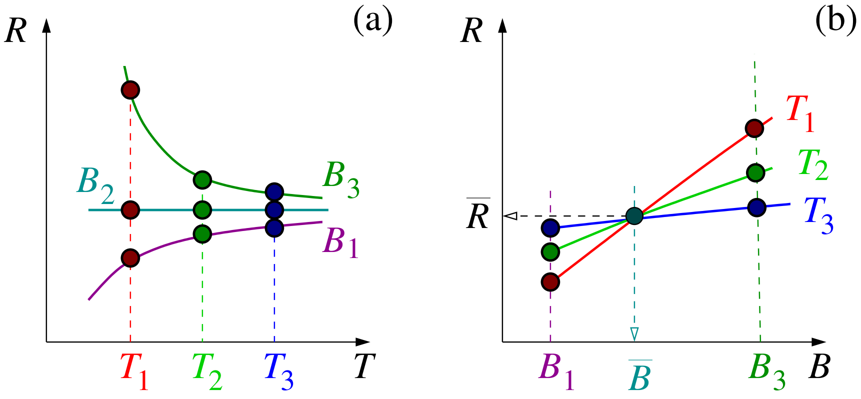

Fig. 1.21 Sketch of the procedure adopted to extract the quantum critical behavior when the superconducting phase is suppressed by means of a magnetic field perpendicular to the interface. (a) When the resistance R is plotted as a function of temperature T, three behaviors are observed over a certain temperature interval, exemplified by the curves corresponding to the three magnetic fields $B_1 < B_2 < B_3$: superconducting, critical, insulating. (b) To better identify the critical value of the magnetic filed, $B_\times$ or B_c, isotherms are plotted as a function of B, exemplified by the three curves corresponding to the temperatures $T_1 < T_2 < T_3$: the crossing point of the isotherms corresponds to $\overline{B}$ ($B_\times$ or B_c), and the corresponding characteristic value $\overline{R}$ is obtained on the resistance axis.

In order to identify the correct values of R_c and R_x, and the corresponding magnetic fields B_c and B_x, the resistance curves are plotted as a function of the magnetic field B at different temperatures, looking for their crossing point (figures 1.21, 1.22(a,c)).

When the resistance R is rescaled[6] by the characteristic value $\overline{R}$ and plotted as a function of the variable $(B-\overline{B})/T^{1/z\nu}$ (see figure 1.22), z being the dynamical exponent (converting a critical length scale in a time scale), and ν the critical exponent of the correlation length as a function of temperature, two quantum critical scaling regimes are found, in different temperature ranges (figure 1.22(b,c)). Criticality is signaled by the collapsing of the resistance curves on top of only two “master curves”.

These two scaling regimes, separated by a crossover at intermediate temperatures, are in correspondence with two different values of the characteristic magnetic field $\overline{B} = B_\times, B_c$. The smaller field, $B_\times$, is related to the scaling at higher T, with $z\nu \approx \frac{2}{3}$, whereas the (slightly) larger field, B_c, corresponds to the scaling at lower T, with $z\nu \approx \frac{3}{2}$. Noticeably, the characteristic fields $B_\times$ and B_c coalesce at low carrier density, i.e. low gate voltage V_g. When V_g is increased, $B_\times$ saturates to a constant, B_d, whereas B_c closely tracks the superconducting critical temperature T_c (with a conversion factor of 1 T corresponding to 1 K. See figure 1.23 (a)).

---

[6] This procedure is called by the Finite Size Scaling (FSS) analysis and will be used also in chapter 4. A brief explanation of how FSS works can be found in the appendix B.

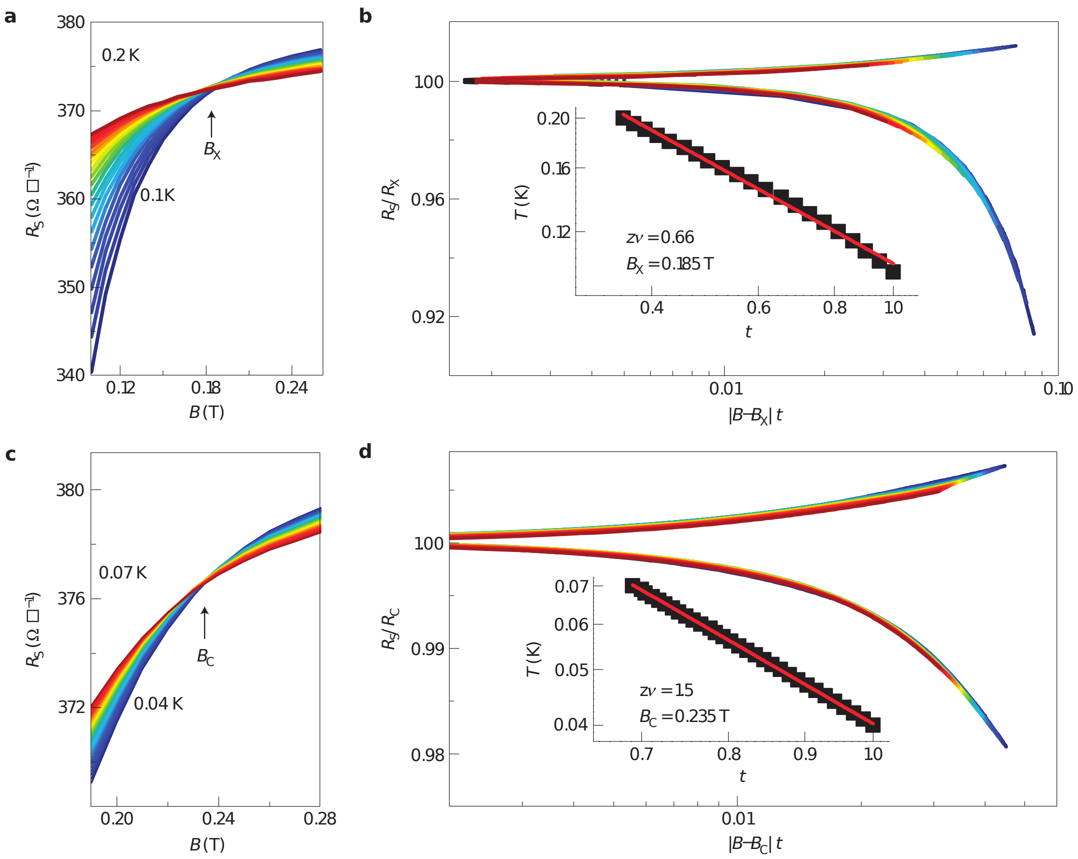

Fig. 1.22 FSS analysis for $V_G = +80\,V$. (a) Sheet resistance R_S as a function of magnetic field B for different temperatures from 0.1 to 0.2 K. The crossing point is (B_X = 0.185 T, R_X = 372.4 $\Omega\Box^{-1}$). (b) FSS plot of R_S/R_X as a function of $|B - B_X|t$ (see text for the definition of t). Inset: temperature behavior of the scaling parameter t. The power-law fit gives $z\nu = 0.66$. (c) R_S as a function of B for different temperatures from 0.04 to 0.07 K. The crossing point is (B_C = 0.235 T, R_C = 376.6 $\Omega\Box^{-1}$). (d) FSS plot of R_S/R_C as a function of $|B - B_C|t$. Inset: temperature behavior of the scaling parameter t. The power-law fit gives $z\nu = 1.5$. Figures from reference [8].

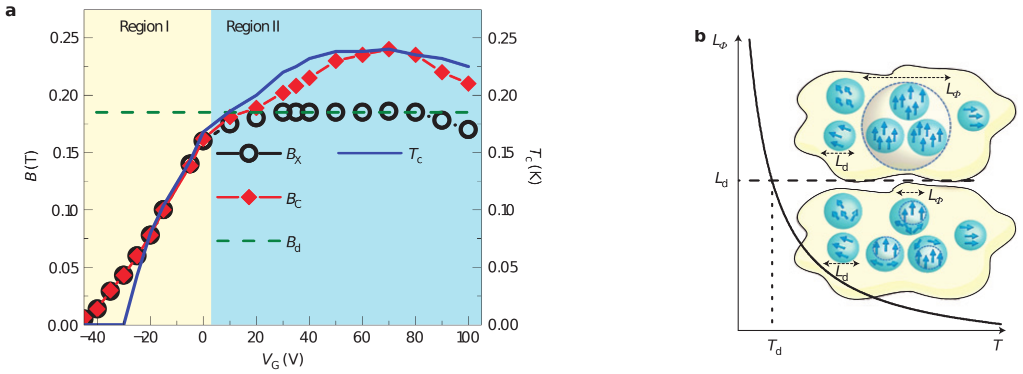

Fig. 1.23 (a) B_x,B_c (left scale) and T_c (right scale) as a function of V_g . The dashed line corresponds to B_d. Regions I and II refers to the low, and respectively high, coupling regimes (see text). (b) The dephasing length L$_\phi$ diverges with decreasing temperature, and reaches the size of the superconducting puddles L$_d$ at T$_d$. The insets show a piece of material in the two regimes. At high temperature (bottom), $L_\phi < L_d$ and the system is in the clean limit, whereas at low temperature (top), $L_\phi > L_d$, and the system is in the dirty limit. In this drawing, superconducting puddles (blue) are coupled through a 2DEG (yellow). The arrows symbolize the local phase of the superconductor. Figure taken from [8].

A possible explanation for this multiple critical behavior relies on the assumption that superconductivity develops in static puddles embedded in a metallic background. Within an isolated puddle, superconductivity would be suppressed by the smaller critical field $B_\times$. However, the puddles are coupled through their common metallic background [96]. When inter-puddle coupling eventually intervenes, superconductivity is strengthened and survives up to the (slightly) larger critical field B_c.

If we borrow the value of the dynamical exponent $z = 1$, which is commonly adopted in similar situations [95], the intra-puddle criticality is described by the XY model [56, 101, 69, 63] in the clean limit, where $\nu \approx \frac{2}{3}$. However, when the temperature decreases, the coherence length, L_ϕ, increases, eventually exceeding the puddle size, L_d, and inter-puddle superconductivity establishes in the inhomogeneous landscape of puddles embedded in the metallic background (see figure 1.23 (b)). In this case, the exponent ν must obey the Harris criterion[52] for disordered systems, and indeed we find $\nu \approx \frac{3}{2} > 1$.

In it worth noting that the superconducting puddle size can be estimated from the saturation value B_d, once one recognize that B_d is the critical field $B_\times$ on a puddle of size L_d ($B_d \sim \phi_0/L_d^2$, where ϕ_0 is the flux quantum). From this relation, a value of $L_d \sim 100\,\text{nm}$ is found, compatible with the size of the puddles estimated by electrostatic arguments in reference [19].

Chapter 2

Inhomogeneous multi-carrier superconductivity

In the previous chapter we have shown that magnetotransport experiments reveal the presence of high- and low-mobility carriers in LTO/STO, and superconductivity seems to develop as soon as high-mobility carriers appear, when carrier density is tuned above a threshold value by means of gate voltage, V_g (see figure 2.1). The width of the superconducting transition is anomalously large and cannot be accounted for by reasonable superconducting fluctuation. This phenomenology suggests instead that an inhomogeneous 2DEG is formed at these oxide interfaces, opening the way to a scenario of percolative superconducting transition [26].

Here we first provide new, compelling evidence of the inhomogeneous character of the 2DEG, extending previous multicarrier analyses of magnetotransport measurements to deal with inhomogeneous systems. Using a phenomenological description of the electron gas, based on the detection of multiple type of carriers and inhomogeneities, we shall then show that the measured resistance, superfluid density, and tunneling spectra result from the percolative connection of superconducting puddles with randomly distributed critical temperatures, embedded in a weakly localized background.

Despite most of the analysis carried out in this chapter is referred to back gated samples, we expect that our conclusions remain valid also in a top gating configuration.

The outline of this chapter is as follows: in section 2.1, we propose a model for multi carrier magnetotransport in inhomogeneous systems, and show that previous analyses of the magnetoresistance and Hall resistance measurements, in terms of two different species of carriers [9], are fully consistent with the inhomogeneous character of the 2DEG at the LAO/STO and LTO/STO interfaces. In sections 2.2, 2.3, and 2.4, we revisit some of our previous results. Assuming inhomogeneity as an empirical evidence, we show that resistance measurements [9] and the topographic mapping of the superfluid density [6] can be accounted for within

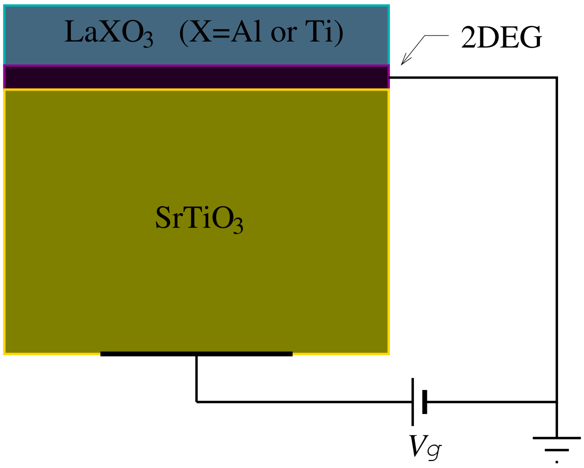

Fig. 2.1 Scheme of an oxide interface (not in scale), in the back gating configuration. The LAO (or LTO) topmost slab has a thickness of few nm, whereas the STO slab is ≈ 0.5 mm thick. The back gate voltage V_g is employed to tune the carrier density of the 2DEG. The top gating configuration is also possible.

a percolative scheme. In section 2.5, we discuss some preliminary aspects of a theory for metal-insulator-superconductor tunneling in inhomogeneous superconductors that is apt to reproduce the measured tunneling spectra [88]. In section 2.6, relying on the results of [24], we show that the properties of the superconducting puddles (e.g., their fractions and critical temperatures) can be extracted from experiments and used to model intra puddle, multi carrier superconductivity, gaining insight about the pairing mechanism. Although some features of the diamagnetic response seem to be related to strong superconducting coupling [6], we show instead that inhomogeneities and multi carrier superconductivity fully account for the behavior of these systems within a standard, weak-coupling Bardeen–Cooper–Schrieffer (BCS) scheme.

2.1 Multi-carrier magneto-transport in inhomogeneous systems

The detection of high- and low-mobility carriers by means of magneto transport measurements in LTO/STO [9] is not necessarily direct evidence of inhomogeneity, since the two species of carriers could coexist in a homogeneous manner. However, to account for the phenomenology of the superconducting state of the 2DEG at the LXO/STO interface, we propose that the 2DEG is inhomogeneous, with higher-density regions (the superconducting puddles) and lower-density regions (the metallic background) [8, 24]. Assigning a band structure to the system, one assumes that when the density is large enough to fill the bands occupied by the high-mobility carriers, the high-mobility carriers should locally coexist with low-mobility carriers occupying the lower-lying levels (see also section 2.6). A picture then emerges in which the low-mobility carriers alone are present in the metallic background, whereas both low- and high-mobility carriers exist in the superconducting puddles. To improve our description of LXO/STO interfaces, we must then rely on a theory for multi carrier magneto transport that is able to deal with an inhomogeneous system. One such theory has been developed in the form of an effective medium theory (EMT) for the Hall conductance of a binary medium resulting from the mixture of two phases and based on rotation transformations (see [3] for a detailed description of this method). In our description of the LXO/STO interfaces, a less dense phase hosts a species of low-mobility carriers, and the other, denser phase hosts both high- and low-mobility carriers. Following [3] and appendix A.2 we derived the expression for the Hall resistance of the inhomogeneous system as

$$R_H^{EMT}(B,\varepsilon) = \frac{\sigma_{xy}^{EMT}(B,\varepsilon)}{\sigma_{xy}^{EMT}(B,\varepsilon)^2 + \sigma_{xx}^{EMT}(B,\varepsilon)^2} \tag{2.1}$$

which we use to accurately fit the experimental resistivity data of LTO/STO [9] under strong magnetic field and at different gate voltages (see figure 2.2). Here $\sigma_{xx}^{EMT}(B,\varepsilon)$ and $\sigma_{xy}^{EMT}(B,\varepsilon)$ are the diagonal and the off-diagonal elements of the conductivity tensor, as defined in appendix A.2, B is a magnetic field perpendicular to the interface, ε is the deviation from the percolating threshold[1]. This procedure allows us to extract the values of both the mobilities, μ_i, and the densities, n_i, of the two species of carriers, as well as the fraction of the system occupied by the superconducting puddles, w. These values are reported in figure 2.3, while the inset of figure 2.2 displays the evolution of the normal-state sheet resistance, extracted using the relation $R = [\sigma_{xx}(B=0,\varepsilon)]^{-1}$ with changing V_g.

Our present findings cast a new perspective on the analysis carried out in [9], where the appearance of more mobile carriers around $V_g = 0\,\mathrm{V}$ was found. On the one hand, we fully confirm that result, but on the other hand, we find here that the magnetotransport data are well described assuming that these carriers do not appear uniformly in the whole system. Rather, high- and low-mobility carriers coexist in a high-mobility metallic phase, identified here with phase (2), which is inhomogeneously distributed at the interface and spatially separated from the less metallic phase (1), where only one species of less-mobile carriers is present. In this framework, the enhanced conductivity around $V_g = 0V$ and the changes in the slope of the Hall resistance at a high magnetic field occur because a finite fraction, w, of phase (2), which

---

[1] We use $w \equiv \frac{1}{2} - \varepsilon$ for the fraction of the system occupied by the superconducting puddles. See appendix A.2

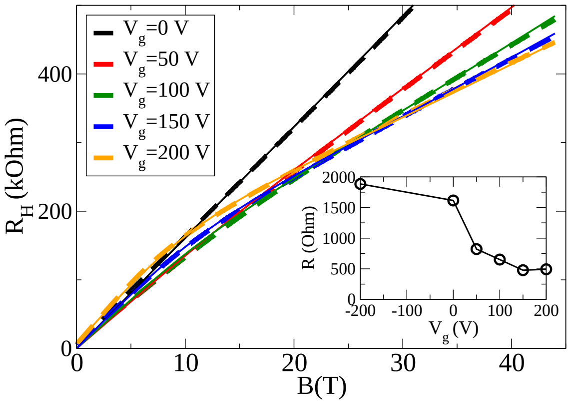

Fig. 2.2 Hall resistance as a function of the magnetic field for different gate voltages, V_g, measured at $T = 4.2K$ in an LTO/STO 15-unit-cell-thick sample (sample A of [9]). Solid lines correspond to experimental data, taken from [9], while the dashed lines obtained here fit the data in equation (2.1). For clarity, the curves have been shifted upwards by $50\,\Omega$ in increasing voltage order. Inset: Sheet resistance R, obtained via equation (A.6), as a function of the gate voltage.

is characterized by an overall higher carrier density and hosts high-mobility carriers, appears around this gate voltage (see figure 2.3(a)). In agreement with the conclusions of [9], we also find that the more mobile carriers have a lower-density than the low-mobility carriers (figure 2.3(b)) but, in contrast with the results obtained within a homogeneous description, the mobilities of the two species stay rather constant over the whole range of gate voltages in the present inhomogeneous scheme (see figure 2.3(c)).

2.2 Percolative superconductivity

After assessing the occurrence of inhomogeneous multi carrier magneto transport at LXO/STO interfaces, we discuss the superconducting transition that is driven by tuning the gate voltage, V_g (i.e. the carrier density), above a threshold value. It has been shown that the superconducting transition that occurs in inhomogeneous system is well described within the EMT [26]. EMT is a mean-field-like theory used to describe a random resistor network (RRN) that lacks spatial correlation. The EMT equations are obtained by embedding one given random resistance, R_i, in an effective medium of constant resistance, R. The latter is chosen so the same current that flows thorough R_i also flows in the RRN (see appendix A). The EMT resistance can be shown [26] to be larger than the parallel of random resistance, and smaller

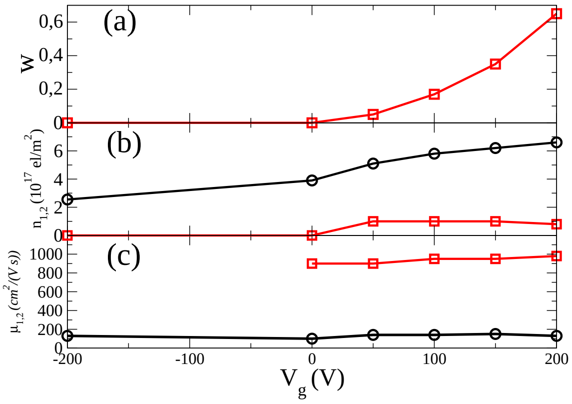

Fig. 2.3 (a) The fraction w, of the high-mobility metallic phase (phase (2), see text). (b) Densities of the less (n_1, empty circles) and more-mobile (n_2, empty squares) carriers extracted from the fits of the Hall resistance, equation (2), as a function of the gate voltage measured at $T = 4.2K$. (c) Mobilities μ_1 (empty circles) and μ_2 (empty squares) of the majority (low-mobility) and minority (high-mobility) carriers, respectively, extracted from equation (2). Type 1 (low-mobility) carriers alone are present in phase (1), while both type 1 and 2 (high-mobility) carriers are present in phase (2).

than the series of random resistances with the two limiting values being reached in infinite and one dimensions, respectively.

The resistance of the LTO/STO interface exhibits a marked suppression due to incipient superconductivity, which is accurately fitted [24], assuming that the superconducting puddles occupy a fraction, $w < 1$, of the sample, and that each puddle is characterized by a random local critical temperature, T_c. For the sake of definiteness, we adopt a Gaussian distribution of critical temperatures, $W(T_c)$, parametrized by its mean value, $\bar{T}_c$, and its width, γ. The remaining $1-w$ fraction of the sample is occupied by metallic background. The resistance at temperature T is found within EMT to be [26]

$$R(T) = R_\infty \left[(1-w) + w \,\mathrm{erf}\left(\frac{T - \overline{T}_c}{\gamma\sqrt{2}} \right) \right],$$

and results form the metallic background (first term inside the square brackets) and from not yet superconducting puddles (i.e., those puddles with $T_c < T$, the second term inside the square brackets, with erf being the error function); the remaining puddles (i.e. those with $T_c > T$), have become superconducting and do not contribute to the resistance. The high-temperature resistance R_∞, w, $\overline{T}_c$, and γ are used as fitting parameters. The global zero

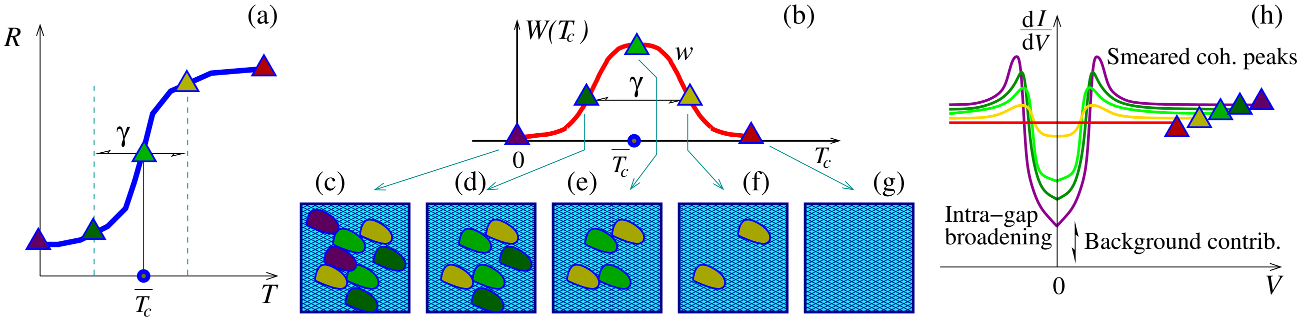

Fig. 2.4 (a) Sketch of the behavior of the resistance as a function of temperature in a case when the superconducting fraction does not percolate. (b) Distribution of critical temperatures $W(T_c)$ in the superconducting puddles, that occupy a fraction w of the sample (the remaining $1-w$ fraction will never become superconducting). (c−g) When the temperature is reduced [from (g) to (c)] superconducting puddles appear in the system as soon as the local critical temperature exceeds T. However, if the puddles do not percolate down to $T=0$, the global zero resistance state is never reached. (h) Sketch of the tunneling spectra measured in LAO/STO, as a function of bias voltage V: At temperatures well above the temperature at which the zero resistance state is reached (if ever), a suppression is observed in the tunneling spectra around zero bias, accompanied by more or less pronounced coherence peaks above the gap. The coherence peaks are smeared and the intra-gap spectra are broadened, with non-vanishing zero bias spectral weight, that we attribute to the metallic background. The curves are labelled by colored triangles that refer to the corresponding temperatures in panel (a).

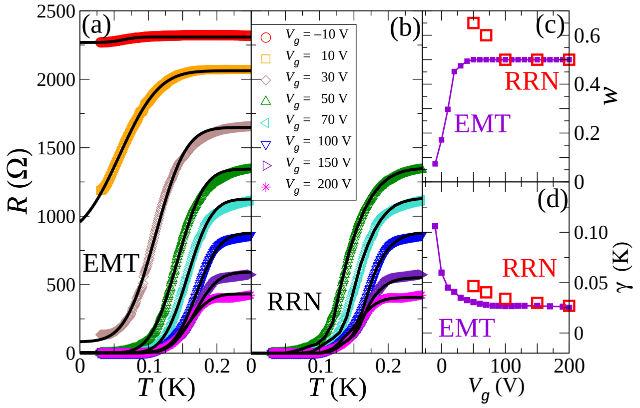

Fig. 2.5 (a) Measured sheet resistance in a LAO/STO sample, for $V_g = -10, 10, 30, 50, 70, 100, 150, 200$ V. The solid lines are the EMT fits. (b) Same as in panel (a), with fewer experimental curves, fitted by RRN curves (solid lines). The RRN fits are based on an exact numerical solution of the Kirchhoff equations for the resistive network. (c) Weight of the superconducting fraction and (d) width of the T_c distribution, from EMT (line and squares) and RRN (large open squares) fits.

resistance state is reached at the percolative transition temperature, $T_p \le \overline{T}_c$ such that

$$\operatorname{erf}\left(\frac{T_p - \overline{T}_c}{\gamma\sqrt{2}}\right) = \frac{w-1}{w}. \tag{2.2}$$

A solution for T_p only exists if the superconducting fraction of the 2DEG can percolate in the two dimensional system (i.e., for $w \ge \frac{1}{2}$). When $T_p < 0$, or when it is not at all defined (for $w < \frac{1}{2}$), the resistance remains finite down to $T = 0$, although the presence of a sizable (yet not percolating) superconducting fraction is mirrored by a sizable suppression of $R(T)$, as sketched in Fig. 2.4(a).

The resistance measured in an LTO/STO sample as a function of T for various values of the gate voltages, V_g, [9] are shown in figure 2.5(a), along with the fitting EMT curves (symbols and solid lines, respectively). Figure 2.5 is inspired by a similar figure in [24], with new elements included to make explicit connection with the overview contained in this paper.

The set of parameters $R_\infty, w, \overline{T}_c, \gamma$, i.e., the distribution of the puddles, changes with changing the carrier density by means of gating.

We are thus able to extract from the fits the mean intra-puddle critical temperature $\overline{T}_c$ (i.e., the temperature at which $R(T)$ changes curvature within EMT), which will be analyzed in section 2.6, and the overall superconducting fraction w, which is tracked by the solid line with filled squares in figure 2.5(c). Note that EMT disregards spatial correlations, so that the presence of pronounced tails in the resistance, in the presence of a percolating superconducting cluster, force the overall superconducting fraction to be[26] $w \approx \frac{1}{2}$, as shown in Fig. 2.5(c). The width γ of the Gaussian distribution of T_c is plotted as a solid line with filled squares in figure 2.5(d). It increases as the fraction w of the puddles goes to zero. This is rather natural because a reduction of the carrier density emphasizes the effects of disorder, so that fluctuations of the local superconducting critical temperature increase, leading to a broadening of the T_c distribution.

A comment is now in order. When dealing with superconducting puddles embedded in a superconducting background, we expect the proximity effect [78, 65] to play an important role in LXO/STO interfaces. Within EMT, this effect certainly entails the temperature dependence of the superconducting fraction, w. However, when fitting the resistance curves, $R(T)$, the introduction of a temperature-dependent $w(T)$ is not viable, because it would make a good fit by definition. Nonetheless, the role of the proximity effect can be analyzed when discussing tunneling spectra. We shall come back to this point in section 2.5.

2.3 Superfluid density in inhomogeneous superconductors

The inhomogeneous character of the 2DEG at the LXO/STO interfaces raises the question of the description of the superfluid properties in a mixture of two phases.

The superfluid density n_s was measured [6] by means of a Superconducting Quantum Interference Device (SQUID) in LAO/STO interfaces. The measurements average over micrometric scales and are therefore not sensitive to submicrometric inhomogeneities. Nonetheless, the idea that the 2DEG at these interfaces is inhomogeneous, is still supported by the evidence of variations of n_s on the micrometric scale within a given sample. Encouraged by the marked similarity of the resistance curves in LAO/STO and in LTO/STO, we apply EMT also to describe the measured local n_s as an average over an inhomogeneous state of submicrometric puddles. We point out that recent experiments in LTO/STO [8] led to estimate the typical size of the puddles to be $\approx 100\,\mathrm{nm}$, thereby supporting this idea.

We proceeded to extend EMT to a small frequency, ω[24], and assigning a Drude-like complex conductivity, $\sigma_M(\omega) = \Lambda(\Gamma + i\omega)^{-1}$, to the metallic background and assigned a purely reactive conductivity, $\sigma_S(\omega) = \Lambda(i\omega)^{-1}$, to the superconducting puddles. We then defined the resistivity $\rho_S(\omega) \equiv \sigma_S^{-1}(\omega)$ and $\rho_M(\omega) \equiv \sigma_M^{-1}(\omega) = \rho_0 + \rho_S(\omega)$, with $\rho_0 \equiv \Gamma/\Lambda$. At high T, the system is metallic and $\rho(\omega) = \rho_M(\omega)$. However, when the temperature is lowered, the static resistivity vanishes within each individual puddle as soon as T equals the local T_c. Although the full expression of the complex resistivity can be found within EMT, aiming at describing the static diamagnetic response, we give only the expression

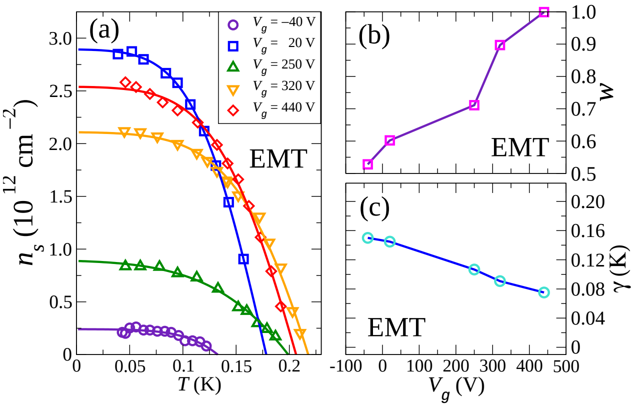

Fig. 2.6 (a) Superfluid density (symbols) as a function of T and EMT fits according to Eq. (2.3) (solid lines). Weight of the superconducting fraction (b) and width of the T_c distribution (c) extracted from the EMT fits, as a function of V_g. The lines are guides to the eye.

up to terms $\sim \omega$, i.e., $\rho(\omega) \approx \rho_0\,(w_M - w_S)\,\vartheta(w_M - w_S) + |w_M - w_S|^{-1}\rho_S(\omega)$, where ϑ is the Heaviside function, w_S is the fraction of puddles that have become superconducting at a given temperature, and $w_M = 1 - w_S$ is the non superconducting fraction resulting both from puddles that have not yet become superconducting and from the metallic background. Evidently, when $w_M > w_S$, the conductivity is Drude-like. However, below the percolation temperature T_p (whenever defined), $w_M < w_S$, and the conductivity is purely reactive: $\sigma(\omega) = \Gamma\,(w_S - w_M)\,(i\omega)^{-1}$. Therefore, using equation (2.2), we find that the superfluid density of the percolating two-dimensional network for $T \le T_p$ is

$$\begin{aligned} n_s &\propto w_S - w_M \\ &= w\left[\operatorname{erf}\left(\frac{T_p - \overline{T}_c}{\gamma\sqrt{2}}\right) - \operatorname{erf}\left(\frac{T - \overline{T}_c}{\gamma\sqrt{2}}\right)\right]. \end{aligned} \tag{2.3}$$

In Fig. 2.6(a), this average superfluid density and our EMT fits (equation (2.3)) are reported for different values of V_g. The behavior of $n_s(T)$, although qualitatively resembling the BCS prediction, may quantitatively differ from it. The slope at $T = T_p$, for instance, is controlled by the width γ of the distribution $W(T_c)$. Thus, the deviations from standard BCS prediction measured in Ref. [6] and attributed to a tendency to strong coupling are here alternatively explained claiming that the 2DEG is in a weak coupling BCS regime (see Sec. 2.6), but the superfluid density is intrinsically inhomogeneous at the submicrometric scale, and is averaged at the micron scale by the SQUID pick-up loop used in Ref. [6]. We point out that our mean field approach is justified by the observation that the channels down to $\approx 500\,\mathrm{nm}$ wide share properties similar to those of the larger samples [98]. Our fits yield the fraction, w, of volume occupied by the puddles, extracted from measurements of the superfluid density and reported in Fig. 2.6(b). It ranges from $\frac{1}{2}$ to 1, and is always larger than the fraction obtained from transport measurements. This is not surprising, because transport mainly probes the long-range connectivity of the percolating path, regardless of dead ends and disconnected superconducting regions [1], whereas diamagnetic screening measurements are sensitive to all sufficiently large superconducting loops, even when not connected to the backbone. In this case, the diamagnetic fraction can be large and the long-distance connectivity can be small if many puddles or loops are disconnected (see section. 2.4). Figure 2.6(c) reports the behavior of the width, γ, of the distribution $W(T_c)$, inferred from the superfluid density. We point out that, despite the fact that we are dealing with different materials and physical quantities, the behavior of γ resembles that obtained from transport in LTO/STO, as seen in figure 2.5(d), and is of comparable magnitude. Of course, a proof of the above arguments requires a model accounting for space correlations that includes both closed loops (relevant for diamagnetism) and connected paths (relevant for transport). While such a model has been found for transport (see Sec. 2.4), a similar model for the diamagnetic response is not yet available, so our discussion on this specific aspect has a purely speculative character. An experimental test to our scenario could be provided by the observation of different diamagnetic responses in field-cooled and zero-field-cooled samples. In the first case one expects substantially smaller diamagnetic fraction, since a sizable flux would be trapped in the normal part, encircled by the superconducting loops (see the shaded region in figure 2.7 and the discussion in section 2.4).

The study of the dynamical response of an inhomogeneous superconductor at finite frequency, within EMT, is presently under investigation. A somewhat similar approach, applied to superconducting stripes in high-temperature superconductors, can be found in [74].

2.4 Space correlations within the superconducting cluster

A possible explanation for the discrepancy between the superconducting fraction, w, observed in both transport and diamagnetism measurements may rest upon the filamentary structure of the superconducting cluster at oxide interfaces [27]. So far, we have made use of the mean-field-like EMT, which completely neglects spatial correlations. To investigate the mechanisms determining the superconducting fraction observed in transport, $w \approx \frac{1}{2}$, we solve a random resistor network (RRN) where the superconducting puddles form a spatially correlated cluster embedded in a metallic matrix. Preliminary results [16] indicated that a superconducting cluster dense at short distances and filamentary at larger distances is necessary in order to reproduce the observed tails of the resistance curves near percolation. Based on this observation and following a procedure similar to the one described in [18], we generated a fractal-like cluster that has small long-scale connectivity and percolates only when almost all bonds have become superconducting. We point out that the fractality of the cluster is an artifice to produce spatially correlated networks that are at the same time dense at short distances and filamentary over long distances. For a Gaussian $W(T_c)$, the low temperature tail of the distribution must be necessarily reached in order to get a percolating path, and a correspondingly pronounced tail in the resistance is obtained. In absence of a filamentary structure at long distance, compact clusters fail to reproduce the tails in the resistance. Our systematic investigation showed that the presence of loosely connected filaments is necessary to get the correct behavior of $R(T)$ near percolation. On the other hand, a purely filamentary structure, no matter how dense at short distance, is too loose and is not apt to describe the behavior of $R(T)$ at higher temperatures. In order to tune the density of the superconducting cluster without significantly changing the long-distance connectivity, we decorate the filaments with randomly distributed superpuddles, which we assume are circular for simplicity's sake. Their number and size is chosen to produce weights w ranging from 0.3 to 0.7 (see the sketch in figure 2.7). Superpuddles may be produced either large tails in the distribution of the puddle sizes or by extrinsic pinning centers, promoting the nucleation of much larger puddles. We systematically investigated the effect of the size and density of the superpuddles. A smaller fraction of larger superpuddles or a larger fraction of smaller superpuddles are essentially equivalent, as long as the superpuddles do not overlap to form percolating clusters.

In figure 2.5(b) we show our fits of the resistance obtained within our RRNs. Noticeably, even though the superconducting fraction, w, is no longer forced to $\frac{1}{2}$, as it was instead within EMT, the resistance displays pronounced tails only if $0.50 \lesssim w \lesssim 0.65$. The lower bound is imposed by the high slope at intermediate temperatures whereas the upper bound is due to the pronounced tail near percolation. In figure2.5(c) and (d) we show the fraction w occupied by the superconducting cluster and the width γ of the Gaussian distribution $W(T_c)$ obtained within the RRN (open squares): γ qualitatively resembles the width obtained within EMT, and increases upon lowering V_g. Thus EMT and RRN models lead to similar results about the distribution of T_c and its variation with V_g, provided the RRN is dense at short distances and filamentary over long distances.

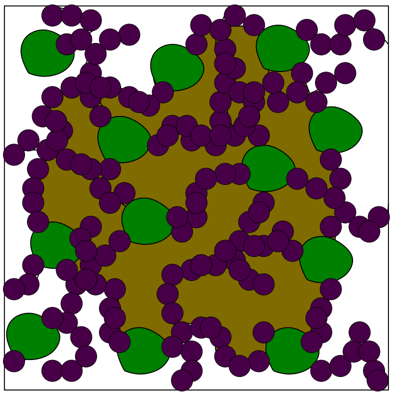

Fig. 2.7 Sketch of the RRN with superpuddles (green regions) connected by filaments of puddles (purple circles). The large shaded region, that does not contribute to superconducting transport, contributes instead to the diamagnetic response in the case of a field-cooling measurement.

2.5 Tunneling spectra of inhomogeneous superconductors

Another possibility for examining the inhomogeneous character of the superconducting state at LXO/STO interface is provided by tunneling experiments. Recent metal-insulator-superconductor tunnel spectroscopy measurements on LAO/STO [88] reveal the occurrence of a state with finite resistance, but with superconducting-like density of states (DOS). The measurements are performed depositing a metallic Au electrode on top of the insulating LAO layer and applying a bias voltage, V, to drive a tunnel current I between the electrode and the 2DEG (see figure 2.8).

The electrode measures several hundreds μm across, thus being orders of magnitude larger than the nanoscale inhomogeneities [8]. At the lowest measured temperature, $T = 30\,\mathrm{mK}$, the spectra reveal a gap in the DOS at the Fermi energy over the entire range of explored gate voltages $V_g \in [-300, 300]$ V, accompanied by more or less broadened coherence peaks above the gap (see figure 2.9 (a)), pointing to superconducting coherence and pairing as the origin of DOS suppression. In the carrier depleted regime ($V_g \ll 0$), the suppression is found even in the absence of global superconductivity, again highlighting the inhomogeneous character of the state formed by superconducting puddles embedded in a metallic matrix. At very low carrier concentration, $V_g \approx -300$ V, the coherence peaks have been completely smeared, although a sizable gap is still present as a signature of (incoherent) pairing. We shall use the term “pseudo-gap state” to describe a state that simultaneously displays a DOS suppression in the tunneling spectra, more or less pronounced coherence peaks, and non-zero electrical resistance. At higher carrier concentration, $V_g = 200$ V, the 2DEG shows a superconducting gap and coherence peaks that decrease with increasing temperature and

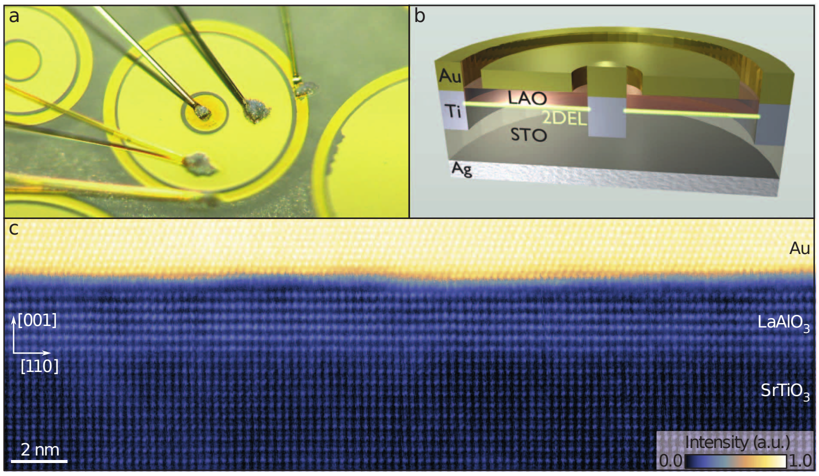

Fig. 2.8 (a) Photograph and (b) schematic cross section of a typical Au/LaAlO$_3$/SrTiO$_3$ tunnel device. The broad gold ring (inner diameter, 160 mm) lies on top of the LaAlO_3 layer, which serves as a tunnel barrier between the 2DEG and the Au. The outer ring and the center contact of the device are Au-covered Ti contacts to the 2DEG. (c) Cross-sectional high-angle annular dark-field STEM image of a Au/LaAlO$_3$/SrTiO$_3$ tunnel junction. The image is taken along the $\left[1\bar{1}0\right]$ zone axis of the perovskite unit cells. Intensity is in arbitrary unit (a.u). Figure and caption from reference [88].

vanish around 300 mK (which agrees with the critical temperature of bulk STO reported in [64]). At $V_g \leq 0$, the gap closes and the coherence peaks vanish at temperatures much higher than the global T_c.

Since the tunneling spectra are taken over several hundreds µm, as we observed above, we expect (see also [17]) that the observed pseudo-gap results from an average over superconducting regions (the superconducting puddles with a DOS described by standard BCS theory) and metallic regions (composed of both the metallic background and not-yet-superconducting puddles) with constant DOS N_0 (see figure 2.4(h)).

The differential conductance is usually written as

$$\frac{\mathrm{d}I}{\mathrm{d}V}(V) = G_0 + G_1 \int_{-\infty}^{\infty} f'(E+eV)N(E)\,\mathrm{d}E, \tag{2.4}$$

where $N(E)$ is the DOS, $f'(E)$ is the derivative of the Fermi distribution function, the positive constant G_0 customarily accounts for effects such as leakage currents, and G_1 is a dimensional constant. We recall that in our model, superconducting pairing occurs within each puddle below a local critical temperature T_c, randomly distributed according to a probability distribution $W(T_c)$. The DOS of the 2DEG probed in the tunneling spectra has

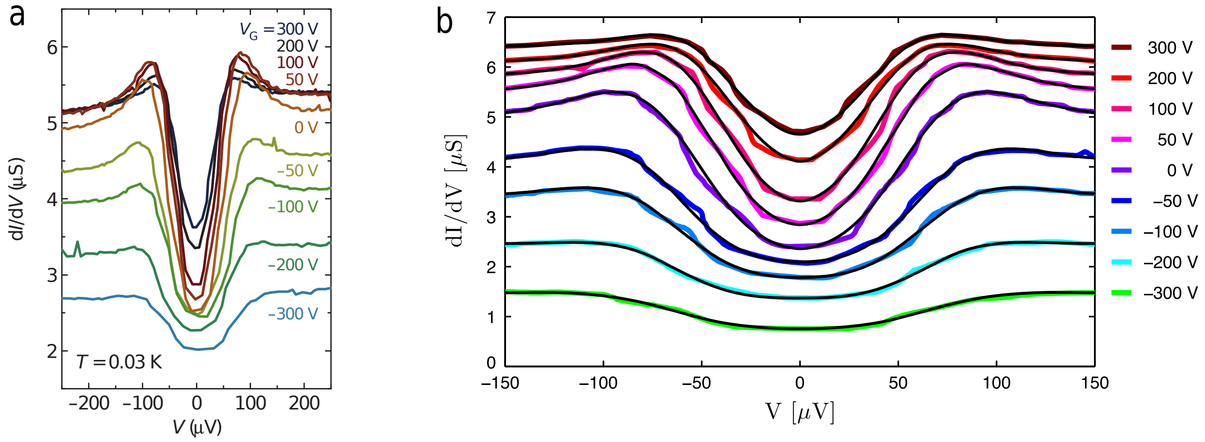

Fig. 2.9 (a) Tunnel spectra for different back-gate voltage, V_G (from [88]). (b) Fits (black curves) of the experimental tuneling data of [88] (colored curves) with a Gaussian distribution of T_c. The curves at positive (negative) gating have been shifted vertically by +0.3 μS (-0.3 μS) for a better view [17].

three distinct contributions,

$$
\begin{aligned}
N(E) &= (1-w)N_0 + wN_0 \int_{-\infty}^{T} \mathrm{d}T_c W(T_c) \\
&+ w \int_{T}^{\infty} \mathrm{d}T_c W(T_c) N_{\Delta(T_c,T)}(E).
\end{aligned} \tag{2.5}
$$

The first two terms correspond to the metallic background and to puddles where pairing has not taken place yet, respectively, and fully account for the zero bias background observed in the tunneling spectra, allowing us to take $G_0 = 0$ in equation (2.4). The third term corresponds to puddles that developed a finite pairing gap Δ. The DOS within these puddles is taken as

$$
N_\Delta(E) = \left[(1-x)\frac{|E|}{\sqrt{E^2-\Delta^2}} + x \right] N_0 \, \vartheta\big(|E|-\Delta\big).
$$

The first term is the standard BCS expression, and describes coherent pairing occurring within a $(1-x)$ fraction of the gapped part. The second term describes puddles that, although having a gap, are too small to exhibit phase coherence. We define w_{pair} as the total fraction of the system that can display pairing down to $T = 0$, and the coherently and incoherently paired fractions $w_{coh} = (1-x)\,w_{pair}$ and $w_{inc} = x\,w_{pair}$. The latter term is necessary because the experimental spectra are gapped but display no coherence peaks when $V_g \ll 0$ [88]. The

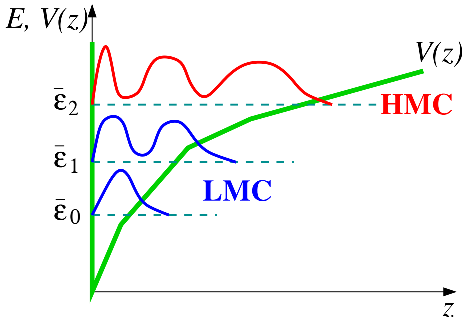

Fig. 2.10 Sketch of the quantized levels $\bar{\varepsilon}_\ell$ in the potential well $V(z)$ confining the 2DEG at the interface (z is the coordinate perpendicular to the interface), and of the corresponding carrier density distributions. The lower-lying levels, e.g., at energies $E = \bar{\varepsilon}_0, \bar{\varepsilon}_1$, accommodate the low mobility carriers (LMC), whereas the topmost level, e.g., at $E = \bar{\varepsilon}_2$, hosts the high mobility carriers (HMC).

gap is assumed to take the BCS expression

$$\Delta(T_c, T) = 1.76\, T_c \tanh\left(\frac{\pi}{1.76}\sqrt{\frac{T_c - T}{T}}\right). \tag{2.6}$$

The value of N_0 is determined by the high-bias part of the spectra, while w, x, and the parameters of the distribution of critical temperatures, $\overline{T}_c$, γ, are used as fitting parameters.

At low temperature, accurate fits the spectra and of their evolution as a function of the gate voltage V_g were obtained [17] (figure 2.9 (b)). Remarkably, the width of the distribution of critical temperatures, γ, turned out to be very weakly dependent of V_g, indicating that the the distribution of T_c in the sample is essentially related to structural properties, like the local amount of disorder.

When fitting the temperature dependence of the spectra at fixed V_g, the attempt to use the same temperature-independent set of parameters captures the main features of the spectra, but yielded fits that are definitely less convincing than the fits at low temperature. However, by releasing the severe constraint of temperature-independent parameters, very good fit are obtained by letting w and x vary, while the parameters of the distribution of critical temperatures, $\overline{T}_c$, γ are kept fixed. The variation of w and x with the temperature is more clearly understood when expressed through the quantities w_{coh} and w_{inc} defined above. It turns out that the fraction of the sample occupied by the superconducting cluster increases with decreasing temperature, and saturates at low T, likely indicating that a sizable part of the metallic background is gradually driven superconducting by proximity effect [17].

2.6 Multi-carrier BCS model

According to the discussion developed so far, the inhomogeneous character of the 2DEG at the LXO/STO oxide interfaces induces a distribution $W(T_c)$ of local critical temperatures, whose mean value, $\overline{T}_c$, depends on the overall carrier density (i.e., on V_g). This dependence is obtained fitting the resistance data in Fig. 2.5(a) within EMT, shedding light on the intra-puddle pairing mechanism. As discussed in section 2.1, detailed magneto-transport measurements [9] highlighted the coexistence of a sizable amount of low-mobility carriers and a smaller amount of high-mobility carriers in LTO/STO. Here, as well as in LAO/STO [84], superconductivity seems definitely to be develop as soon as the high-mobility carriers appear.

Accordingly, we propose [24] that superconducting pairing within the 2DEG formed at the oxide interface may be described by a multi-band [90, 57, 35, 106, 55] BCS-like Hamiltonian

$$\begin{aligned}\mathscr{H}_{BCS} &= \sum_{\mathbf{k},\ell} \xi_{\mathbf{k},\ell} \left(a^\dagger_{\mathbf{k},\ell,\uparrow} a_{\mathbf{k},\ell,\uparrow} + a^\dagger_{\mathbf{k},\ell,\downarrow} a_{\mathbf{k},\ell,\downarrow} \right) \\ &+ \sum_{\substack{\mathbf{k},\ell \\ \mathbf{k}',\ell'}}{}' \frac{g_{\ell\ell'}}{N} a^\dagger_{\mathbf{k},\ell,\uparrow} a^\dagger_{-\mathbf{k},\ell,\downarrow} a_{-\mathbf{k}',\ell',\downarrow} a_{\mathbf{k}',\ell',\uparrow} \end{aligned} \tag{2.7}$$

where $a^\dagger_{\mathbf{k},\ell,\sigma}(a_{\mathbf{k},\ell,\sigma})$ creates (annihilates) an electron with two-dimensional wave vector $\mathbf{k} = (k_x, k_y)$, parallel to the plane of the interface, and spin projection $\sigma =\uparrow,\downarrow$, belonging to the ℓ-th sub-band, with dispersion law

$$\xi_{\mathbf{k},\ell} = \bar{\varepsilon}_\ell + \frac{\hbar^2 k_x^2}{2m_{\ell,x}} + \frac{\hbar^2 k_y^2}{2m_{\ell,y}} - \mu,$$

where $m_{\ell,x(y)}$ are the (possibly anisotropic) effective masses of the charge carriers and μ is the chemical potential, $g_{\ell\ell'}$ are the intraband (for $\ell = \ell'$) or interband (for $\ell \neq \ell'$) pairing amplitudes and N is the number of $\mathbf{k}$ points within the first Brillouin zone. The sub-bands can originate, e.g., from the multiband structure of STO [27, 19] and/or from the quantum confinement within the self-consistent potential well at the interface (see chapter 3). In our schematic description, we represent the whole set of low-lying bands with one sub-band ($\ell = 1$) accommodating the non superconducting low mobility carriers, while the high mobility carriers in the sub-band $\ell = 2$ are paired and give rise to a finite T_c (see figure 2.10, which shows a sub-band structure originated from the quantum confinement).

Thus, according to our interpretation, the superconducting puddles are regions where the $\ell = 2$ sub-band is locally filled, whereas the (weakly localizing) metallic background

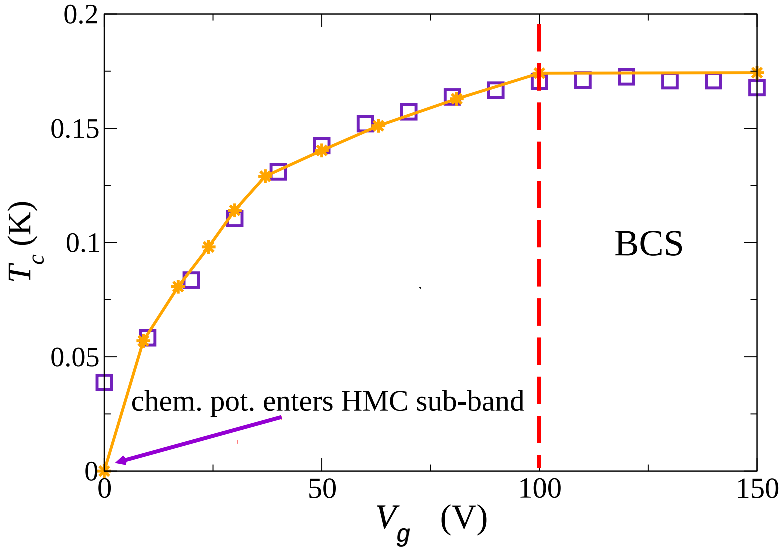

Fig. 2.11 Average critical temperature extracted from the EMT fit of the sheet resistance data (empty squares), and critical temperature of our BCS-like model (solid line with diamonds), as a function of V_g. T_c starts to rise when the chemical potential enters the HMC sub-band ($\mu = \bar{\varepsilon}_2$) and saturates to the standard BCS value when $\mu = \bar{\varepsilon}_2 + \hbar\omega_0$

corresponds to regions where the $\ell = 2$ sub-band is empty. The phenomenology of the superconducting phase at oxide interfaces is reproduced assuming that the pairing amplitudes are such that $g_{11} \ll (g_{12}, g_{21}) \ll g_{22}$. This condition is also consistent with the analysis of a two-band model in [40]. For simplicity, to minimize the number of free parameters, in the following we assume that $g_{11} = g_{12} = g_{21} = 0$. According to the standard BCS approach, the pairing amplitudes are only effective in a window $|\xi_{\mathbf{k},\ell}|, |\xi_{\mathbf{k}',\ell'}| \leq \hbar\omega_0$, where ω_0 is a characteristic cut off frequency. The prime superscript attached to the last sum in Eq. (2.7) implies this restriction. We assume that the bottoms of the two sub-bands are well separated, $\bar{\varepsilon}_2 - \bar{\varepsilon}_1 \gg \hbar\omega_0$, and take henceforth $\bar{\varepsilon}_2 = 0$.

In principle, when deducing a BCS-like Hamiltonian, one should take care of vertex corrections, which are expected to be relevant when Migdal's condition is violated. However, the task of deducing a BCS-like Hamiltonian in a multi band model, where electrons with large and small Fermi energies coexist, is overwhelmingly difficult. Instead, we take equation (2.7) as a phenomenological low-energy effective Hamiltonian where all the high-energy effects have been accounted for by a suitable dressing of the bare physical parameters. Thus, the identification of ω_0 with the characteristic frequency of the pairing mediator is expected to hold only indicatively.

For $\mu \leq 0$, the sub-band hosting the high-mobility carriers is empty and $T_c = 0$. For $0 < \mu < \hbar\omega_0$, the critical temperature is

$$T_c \approx 1.14\,(\hbar\omega_0\mu)^{\frac{1}{2}}\,\mathrm{e}^{-1/\lambda},$$

where $\lambda \equiv g_{22}N_0^{\mathrm{HMC}}$ is the dimensionless superconducting coupling and N_0^{HMC} is the DOS of the sub-band filled by the high mobility carriers. For $\mu \geq \hbar\omega_0$, T_c saturates to the standard BCS value

$$T_c^{BCS} \approx 1.14\hbar\omega_0\,\mathrm{e}^{-1/\lambda}.$$

The previous results can be cast into a single expression

$$T_c(\mu) = T_c^{BCS}\vartheta(\mu)\min\left(\sqrt{\frac{\mu}{\hbar\omega_0}}, 1\right). \tag{2.8}$$

Remarkably, the amplitude $\Delta\mu$ of the interval in correspondence of which T_c is an increasing function of μ provides a direct measure of the characteristic energy scale of the cut off energy scale, $\hbar\omega_0 = \Delta\mu$.

The fit of the curve $\overline{T}_c(V_g)$, extracted from the experimental data in Fig. 2.5(a) within EMT, with the curve $T_c(\mu)$ in equation (2.8), exploiting the approximately linear relation between V_g and μ [9], yields the result illustrated in figure 2.11 (orange line with diamonds and empty squares, respectively).

For instance, if the various band masses are taken all equal to 0.7 electron masses, corresponding to a scenario where the sub-band structure originates from quantum confinement of the lowest t_{2g} band of bulk STO near the interface, we obtain the dimensionless coupling constant $\lambda \approx 0.125$ (therefore consistent with our assumption that the system falls in the weak coupling regime) and $\hbar\omega_0 \approx 23$ meV, which is a typical phonon energy in STO [64].

2.7 Concluding remarks

In conclusion, we first analyzed magneto-transport experiments in LTO/STO oxide interfaces within a multi-carrier EMT model, confirming the occurrence of two kind of carriers, with high and low mobility, within an inhomogeneous landscape. We proposed that the system is made of regions of higher carrier density, were both carrier coexist, and regions of lower carrier density, where only the low mobility carriers exist. We also confirms that the high-mobility carriers have a lower density that low-mobility ones. The mobilities of the two species turn out to be almost independent of the gate voltage. Thus, the enhancement of conductivity observed around $V_g = 0$ V and the change in the slope of the Hall resistance at high magnetic fields occur because a finite fraction, w, of regions with higher carrier density, hosting high-mobility carriers, appears around this gate voltage.

We then described superconductivity in LAO/STO and LTO/STO within a scenario in which superconducting puddles (the regions with coexisting high and low mobility carriers) are embedded in a metallic background (the regions with low mobility carriers only), and form a percolating network. In this framework, the sheet resistance of LTO/STO interfaces is very well described by EMT or by a RRN for an inhomogeneous 2DEG with a substantial filamentary character. Fitting the experiments, we were able to extract the random distribution of T_c at various V_g (i.e. at various carrier densities). A similar approach was adopted to fit the micrometrically averaged superfluid stiffness [6] and the pseudo-gap in tunneling spectra [88] of LAO/STO.

Assuming an effective two-band model with superconductivity triggered by the presence of few high-mobility carriers, locally filling the highest-energy band, we account for the density dependence of the intra-puddle T_c within a simple BCS weak coupling scheme. As an important by-product, we find that the range of variation in V_g of the average intra-puddle T_c is directly related (via the chemical potential μ) to the cut off energy scale, $\hbar\omega_0$. Taking this value as a crude estimate of the typical energy scale of the pairing mediator, we find that this is compatible with phonon-mediated superconductivity.

Chapter 3

Origin of electron inhomogeneity

In the previous chapter it has been shown how magneto-transport experiments and metal-to-superconductor transition can be explained within a multi-carrier EMT model, based on the idea that the system is made of higher carrier density regions, were both carrier coexist, and lower carrier density regions, where only the low mobility carriers exist. Thus, superconductivity is set up only in the regions where high and low mobility carriers coexist, while the remaining of the system stays metallic. We proved that this scenario is consistent with the evidences of inhomogeneities in the superfluid density [6] and accounts for the phenomenology of the superconducting state of the 2DEG at LXO/STO interface. However, this phenomenological model relies on the assumption, which is of course experimentally justified (see e.g. [7]), that also the normal state of the 2DEG is inhomogeneous, a fact that up to now has been left unexplained. The aim of this chapter is to discuss the possible origin of the inhomogeneity of the electron density in the normal state of the 2DEG at LXO/STO interfaces and show how it is related to the appearance of low- and high-mobility carriers.

In order to find a possible explanation to this question, we started from the observation that although extrinsic mechanisms [15], like impurities and growth defects, are always accountable for rendering an interface inhomogeneous, experimental data show that inhomogeneity is never reduced below a sizable extent, even in the best samples. Furthermore, the indication of negative electron compressibility in a low-filling regime [68] suggests that *intrinsic* mechanisms (e.g. in the form of effective electron-electron attractions) are present, which may render the 2DEG inhomogeneous by phase separation, even in a perfectly clean and expectedly homogeneous sample. These facts led us to look for intrinsic mechanisms of inhomogeneity, as those proposed in [27, 19], where a strong density-dependent Rashba spin-orbit coupling (which is present at these interfaces [29]) yields a non-rigid band structure, with the possibility that the chemical potential of the carriers is a non-monotonic function

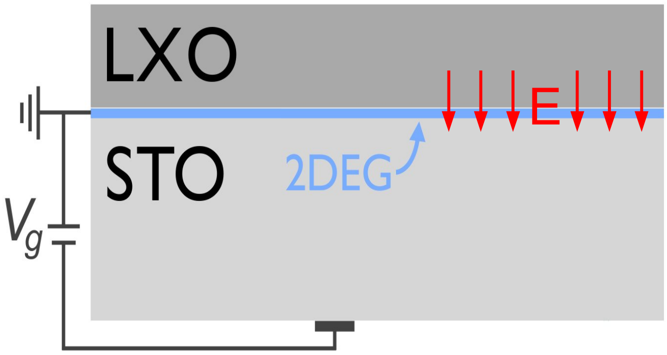

Fig. 3.1 Scheme of an oxide interface in the back gating configuration. Due to the inversion symmetry breaking, a strong electric field E, responsible for the confinement of the electron gas, sets up perpendicularly to the interface. The magnitude of the field depends largely on the local electron density and only marginally on the back gating potential.

of the carrier density for reasonable values of the model parameters, thus giving rise to thermodynamic instability.

Here we propose another possible electron-driven mechanism leading to phase separation, based on the electrostatic confinement of the 2DEG at the interface, which is more effective than the one provided by the density-dependent Rashba spin-orbit coupling (RSOC) and can be present also in other kind of interfaces, where RSOC is weak or even missing. This mechanism, like the one based on RSOC, relies on the presence of a strong electric field, E, which is responsible for the confinement of the electrons at the interface [21] (see figure 3.1). Such field depends on the local electron density via the Poisson equation and determines the potential well where the 2DEG resides, resulting in an energy spectrum which is a function of the local electron density too.

3.1 A model of the interface

From customary self-consistent calculations of the confining potential well in semiconductors, it is well known [39] that a finite lateral extension usually renders the 2DEG more compressible than its strictly 2D counterpart. This effect is proportional to the electron density and in ordinary semiconductor it is reduced by the small number of carriers that is possible to confine in the quantum well at the interface. In LXO/STO, instead, this effect is much stronger, due to the huge dielectric constant of STO, allowing for much larger electron densities, with a strong amplification of the self-consistent adjustments of the confining potential. As a consequence, a non-rigid band structure arises, which varies with the local electron density: an increased electron density is accompanied by a corresponding

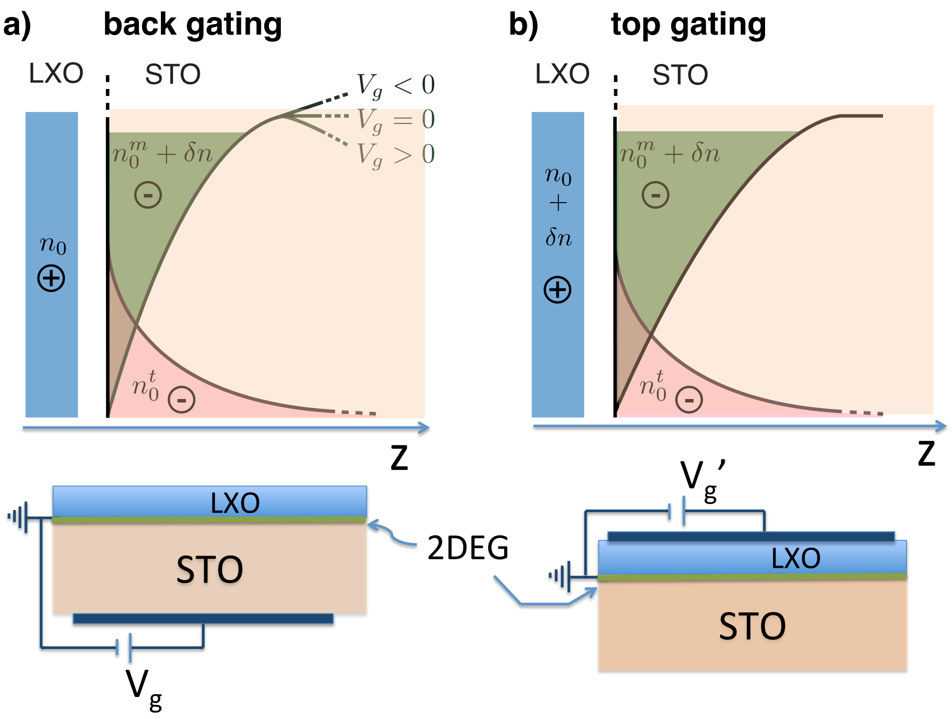

Fig. 3.2 Sketch of the interface for back (a) and top (b) gating. The upper part sketches the confining potentials, while the bottom part reports the structure of samples and electrodes. The confining potential depends on both mobile (n_0^m) and trapped (n_0^t) charges, which together compensate the positive countercharges n_0 in the LXO side. Applying a positive (negative) voltage V_g (or $V_g' \ll V_g$, in the case of top gating), δn electrons per unit cell are added to (subtracted from) the interface and the potential changes accordingly.

increase of the positive countercharges (due to oxygen vacancies and/or polarity catastrophe , from which the interfacial electrons are generated) restoring the overall charge neutrality. For small-to-moderate increases of electron and countercharge densities the potential well deepens and the electron energy levels are shifted downwards.

In the following, the thermodynamic stability of the system is investigated by varying the density of the interfacial gas *while keeping the overall neutrality*. Therefore a corresponding amount of positive countercharges has to be varied (see figure 3.2). Due to this tight connection between positive and negative charges the (in)stability will be determined by calculating the chemical potential of the whole system (i.e., of both the mobile electrons and of the other charges). While we will solve the quantum problem of the mobile electrons in the self-consistent confining well, the countercharges, the fraction of electrons trapped in impurity states of the bulk (see below) and the boundary conditions fixing the gating potential will determine the classical electrostatic energy of the system. All these contributions (for a detailed description see Appendix E) yield the total energy $\mathscr{E}$ and, in turn, the chemical potential $\mu = \mathscr{E}(N+1) - \mathscr{E}(N) \approx \partial_N \mathscr{E}$ (here N represents the number of electrons, which is always kept equal to the number of countercharges).

The energy of the 2DEG is obtained through the calculation of the energy spectra as a function of the electron density, $n \equiv \delta n + n_0$ (henceforth, carrier densities, e.g., n, are meant per interfacial unit cell (u.c.)). Here, the two contribution have a different origin: δn is the extrinsic component introduced by gating, while the intrinsic component n_0 originates from the electronic reconstruction due to the polarity catastrophe and/or from oxygen vacancies within the LXO layer (see section (1.3)). Which of the two dominates is immaterial in our calculations and we represent the related positive countercharges as the light-blue shaded areas in the LXO side of figure 3.2.

What matters, instead, is the way the extrinsic charges are introduced, particularly in the case of back-gating (figure 3.2 (a)): applying a positive voltage V_g, the electrostatic potential, after increasing in the region close to the interface, decreases linearly with distance, once the interfacial charge density has been exhausted (the electrons reside on the STO side, assumed to occupy the $z > 0$ half space, and $n(z) \to 0$ for large z). Then the electrons closest to the top of the well are weakly confined and some of them may escape and get trapped into the defects of bulk STO, as it is demonstrated by irreversibility effects under large back-gating potentials [11]. Thus, in the absence of trapped charges, the quantum well is intrinsically unstable upon positive back-gating. In the top-gating configuration (figure 3.2 (b)), the leakage also occurs, because the Fermi energy of the electrons, attracted to the interface by the positive V_g, exceeds the confining potential on the STO side. In both configurations, we are therefore led to introduce trapped charges that we describe by a distribution $n_0^t(z) = (n_0^t/\lambda)\mathrm{e}^{-z/\lambda}$ on the STO side, decaying over a distance λ of several tens of nanometers (see pink shaded area in figure 3.2). This has the main effect of deepening the confining potential well, the Fermi energy being located substantially below its top (see, e.g., references [9, 72]).

The mobile electrons occupy energy levels that are quantized in the z direction and form a 2D band structure in the xy (interfacial) plane. The electrostatic potential $\phi(z)$ confining the electrons is determined self-consistently with the mobile electron density distribution $n^m(z) \equiv n_0^m(z) + \delta n(z)$ at external gating V_g, for a frozen distribution of trapped charges $n_0^t(z)$ (the z-dependent densities $n(z)$ are related to their counterparts n by relations like, e.g., $n = \int_0^\infty dz n(z)$). The z component of the factorized wave function $\Psi(x,y,z) = \zeta_{i\alpha}(z)\psi_{k_xk_y}(x,y)$ is the solution of the Schrödinger equation[1] yielding the sub-band energy $\varepsilon_{i\alpha}$,

$$\left[\frac{\hbar^2}{2m_\alpha^z}\frac{d^2}{dz^2} + e\phi(z) + \varepsilon_{i\alpha}\right]\zeta_{i\alpha}(z) = 0, \tag{3.1}$$

where the electron charge is $-e$, $i = 1,2,3,...$ is the sub-band index, and $\alpha = xy, xz, yz$ labels the Ti t_{2g} orbitals, d_{xy}, d_{xz}, d_{yz}, where the electrons mostly reside (see chapter 1). According to standard values [91], we take $m_l = 0.7m_e$ and $m_h = 14m_e$ (m_e is the electron mass).

Assuming full translational invariance along the xy planes and integrating over a u.c. of area a^2 with a suitable normalization of $\psi_{k_xk_y}(x,y)$, the density of mobile electrons, at temperature $T = 0$, reads

$$n^m(z) = \sum_{i\alpha}|\zeta_{i\alpha}(z)|^2 \int_{-\infty}^{\varepsilon_F} d\varepsilon\, g_{i\alpha}(\varepsilon),$$

where $g_{i\alpha}(\varepsilon) = a^2(\pi\hbar^2)^{-1}\sqrt{m_\alpha^x m_\alpha^y}\,\theta(\varepsilon - \varepsilon_{i\alpha})$ is the density of states (DOS) of the various t_{2g} sub-bands, $\theta(\varepsilon)$ is the Heaviside function, and ε_F is the Fermi energy.

The electron distribution corresponds to an electrostatic potential $\tilde{\phi}(z)$ obeying the Poisson equation:

$$\frac{\varepsilon_0 a^2}{e}\frac{d}{dz}\left[\varepsilon_r(E)\frac{d}{dz}\tilde{\phi}(z)\right] = n^m(z) + n_0^t(z). \tag{3.2}$$

Here, the dielectric constant is a function of the electric field $E = -d\tilde{\phi}/dz$ via the relation $\varepsilon_r(E) = (A + B|E|)^{-1} + \varepsilon_\infty$, where A, B, and ε_∞ are experimentally measured constants (see also chapter 1). Owing to the nearly ferroelectric character of STO, ε_r can reach very large values ($\gtrsim 25 \times 10^3$) but, due to the very strong interfacial electric field [9, 27, 19], we find that, near $z = 0$, $\varepsilon_r \approx \varepsilon_\infty \approx 100 - 300$. The point of the above derivation is that the calculation

---

[1] The equation E.1 is the Schrödinger equation in the Envelope Function Approximation (EFA). The EFA method is briefly summarized in appendix C.

is self-consistent only if the two potentials, ϕ from equation (E.1) and $\tilde{\phi}$ from equation (E.2), coincide.

Besides the difficulties stemming from the self-consistency, there are additional subtleties coming from the boundary conditions, which vary for the back- or top-gating configuration. In the former case we fix a density of positive charges $n_0 = \int_0^\infty dz\,[n_0^m(z) + n_0^t(z)]$ (per u.c.) at $z = 0^-$. We made this simplifying choice, which turns out to be slightly less favorable to the occurrence of PS, to avoids the distinction between the case of oxygen vacancies (for which the countercharges would be uniformly distributed in the LXO) and the polarity catastrophe (in which the countercharges suitably distribute themselves in the polar planes of LXO in order to minimize the energy [97]). Having fixed the positive charges, we consider the electric field at $z = 0^+$ (i.e., the slope of the confining potential) at the interface. The electric field deep inside the STO (where $n_0(z) \to 0$) is fully determined by the gate potential because the intrinsic electronic density and the corresponding positive charges in the LXO compensate and have thus no effect in this region (see figure 3.2 (a)). On the other hand, the electrons coming from back-gating create a field V_g/L, with $e\delta n = \varepsilon_0 a^2 \int_0^{V_g/L} \varepsilon_r(E)dE$, where L is the thickness of the STO substrate. In the top-gating configuration, instead, the density of positive charges at $z = 0^-$ amounts to $n_0 + \delta n$, and the electric field vanishes deep inside the STO substrate (see figure 3.2 (b)).

Once the quantum problem of mobile electrons is solved, the rest of the energy is due to the electrostatic contribution (per u.c.) of electric fields due to the overall distribution of the mobile (m) and the fixed (f, from gates and trapped) charges

$$\mathscr{E}_{es} = \frac{\varepsilon_0 a^2}{2} \int_{-\infty}^{\infty} \varepsilon_r(E) \left[E^{f\,2}(z) - E^{m\,2}(z) \right] dz, \tag{3.3}$$

with $E = E^f + E^m$. Notice that, since the Hartree-like electrostatic energy is double-counted in the quantum Hamiltonian, the contribution of the mobile charges must be subtracted in equation (3.3). In appendix C we provide details of how the Schrödinger equation is solved numerically, while in appendix E we show a derivation of the contributions to the electrostatic field.

3.2 Phase separation

To show that the electron confinement is the driving mechanism of PS we first consider the pure quantum problem (neglecting the classical electrostatic contributions to the free energy) and study the evolution of the different sub-bands levels as a function of the mobile electron density n^m. When looking for the phase separation, it is important to keep in mind that the mobile electron density is the sum of the as grown carrier density n_0^m and the extra charges δn added by electrostatic gating. While the density n_0^m and its fluctuations are determined by the internal stability of the system, the density δn results from the gate potential V_g, which is an external parameter[2]. Therefore, in order to establish whether the 2DEG is stable or not for a given value of n^m, say $\bar{n}^m$, one has to keep $\delta n \propto V_g$ constant and change n_0^m only, to see whether the chemical potential is an increasing or a decreasing function of n^m in the vicinity of $\bar{n}^m$.

The evolution of the sub-bands levels in figure 3.3 (a) is a direct consequence of the non-rigidity of the bands. The resulting Fermi energy ε_F is going up as expected, while the chemical potential μ^m of the mobile electrons has a non-monotonic behavior. Indeed, when ε_F crosses the first heavy band ($d_{xz,yz}$ which have the largest DOS along the xy plane), μ^m starts to decrease. The most important result here is that, for a given range of mobile electron densities, the chemical potential decreases while electrons are added, resulting into a region of negative compressibility in the phase diagram. This region is reduced when the classical electrostatic contributions (equation 3.3) are added, but still extends over a broad range of densities and voltages. It is delimited by a spinodal line, where the compressibility diverges (i.e., μ has a maximum or a minimum as a function of the density).

To identify the region where the homogeneous system is thermodynamically stable one has to perform a standard Maxwell construction. The Maxwell construction region encloses the spinodal region and it identifies the region where the thermodynamic instability is prevented by phase separation, with the consequent inhomogeneous redistribution of electrons and countercharges. Our calculations, which takes into account both electrostatic and quantum electronic contributions, lead to the chemical potential displayed in the panels of figure 3.3 (b-d) (orange dashed lines) when n^m is increased (the gate voltage is kept constant in this calculation, while n_0^m is varied).

The Maxwell construction results in a very broad PS region delimited by the dashed orange lines in the phase diagrams of figure 3.4(a) and (b) for back- and top-gating, respectively. As it can be seen, the "miscibility gap" extends on a very broad range of densities and voltages. This raises the issue of mechanisms which are present in the real systems to limit this otherwise strong PS tendency. A microscopic modeling of such interactions is exceedingly difficult, but they can be considered within a phenomenological scheme. For instance, while we already took into account the long-range electrostatic cost of the charge distribution, we did not include in our model any short range repulsion between the countercharges (oxygen vacancies or positive charges left by the polarity catastrophe reconstruction). While some mild fluctuations of electrons and compensating countercharges are acceptable,

---

[2] It means that it determines the thermodynamic state of the system, but it is not related to its stability

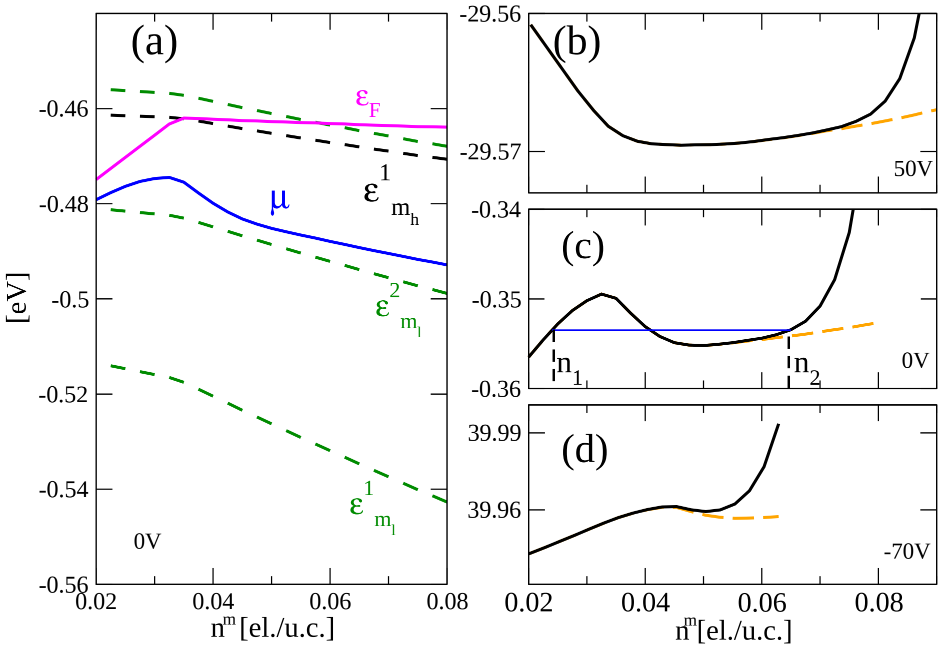

Fig. 3.3 (a) Fermi energy (magenta solid line), electron-only (the purely quantum contribution. See main text and Appendix E) chemical potential (blue solid line), sub-band levels (green dashed for the d_{xy} and black dashed for the $d_{xz,yz}$ levels) as a function of the build-in density n_0 at zero gating potential. (b) Chemical potential as a function of the mobile electron density $n^m = n^m_0 + \delta n$ at fixed values of the back gating potential $V_g(\delta n)$ (the δn electrons due to gating are thus also fixed). The orange dashed (black solid) lines correspond to the solution in the absence (presence) of a short-range background contribution (coming from the repulsion of positive countercharges) to the chemical potential of the form $\mu_{sr}(n^m) = A\left[(n^m - \delta n)/0.065\right]^p$, where the exponent $p = 19$ measures the short-range rigidity and $A = 7\times 10^{-4}$. For $V_g = 50V$, $\delta n = 0.0137$. Both solid and dashed lines include the purely electrostatic terms (see text). (c) Same as (b) with $\delta n = 0$. The thin solid blue line provides an example of Maxwell construction. The densities n_1 and n_2 delimit the miscibility gap and identify the phase separation region at $V_g = 0$V. The same procedure has been performed for all the values of V_g for which the system is unstable, to get the phase diagram of figure 3.4. (d) Same as (b) with $\delta n = -0.0171$.

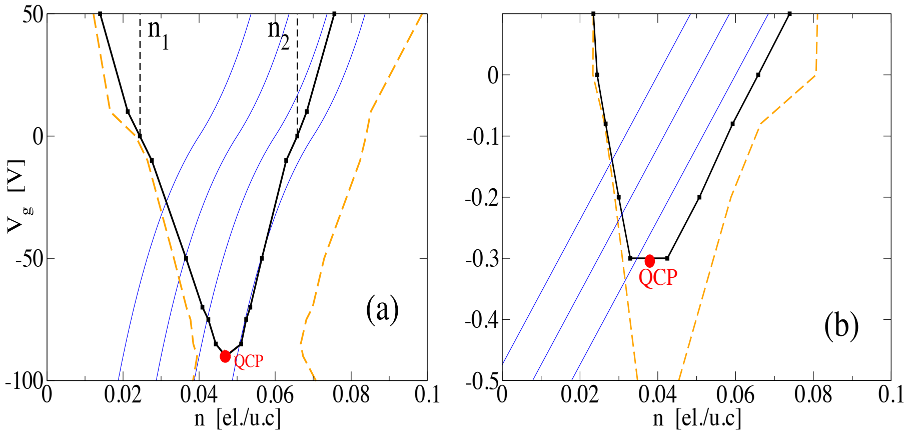

Fig. 3.4 (a) Gate potential versus mobile electron density phase diagram for the back gated LXO/STO interface in the absence (orange dashed lines) and in the presence (black solid lines) of short-range rigidity of the countercharges. n_1 and n_2 are determined by the Maxwell construction exemplified in Fig. 3.3(c). The blue thin solid lines correspond to $n_0 = 0.04, 0.05, 0.06, 0.07$ el/u.c. at $V_g = 0$. (b) Same as (a) for the top-gating case, with $n_0 = 0.04, 0.05, 0.06$ el/u.c. Notice that, despite the different voltage scale, due to the different ε_r and thickness of LXO and STO, the electron densities and confining electric fields are comparable.

when too many electrons segregate carrying along too large densities of countercharges, the system becomes very rigid and the charge segregation stops. To phenomenologically describe this physics, we added a short-range repulsion to the total energy, that induces a rapid growth in $\mu(n)$ when electron densities above those experimentally found (with a maximum of 0.5 el/u.c., including the trapped charges) is reached. Due to this additional short-range mechanism, the PS region determined by the Maxwell construction on the black solid lines of figure 3.3 (b-d) is reduced (black solid lines and squares in figure 3.4(a,b)) and, quite remarkably, it ends with a critical point at some critical negative gate value, V_g^c.

The initial (as-grown) density n_0 is determined by several factors (like, e.g., the number of LXO planes). Starting from a given n_0, the total density, $n = n_0 + \delta n$, is then changed by the gating following the thin blue trajectories in the phase diagram. Upon decreasing the gating the overall average density n decreases and the fraction of the system with lower density n_1 increases, in agreement with transport measurements [24, 25, 22], until the system exits the PS region at some negative voltage.

From figure 3.4 (a) and (b) one can see that there exists a broad range of the intrinsic density n_0 yielding a negative compressibility, prevented by PS. This PS yields an inhomogeneous 2DEG with associated inhomogeneity of the oxygen vacancies and/or electronic reconstructions. We carried out a detailed analysis (see also appendix E) to identify the specific mechanisms determining this instability, finding that it arises from two main features peculiar to these oxide interfaces.

First of all, a larger n_0 corresponds to larger countercharge density on the LXO side, which attracts the interface electrons and deepens the confining potential well, causing a downward shift of the quantized levels. Secondly, the electrons at the interface are confined on the STO side, where a large dielectric constant ($\varepsilon_r > \varepsilon_\infty \gtrsim 100$) efficiently screens the electric fields. This allows for the accommodation of a large number of electrons ($\approx 10^{13}\,\mathrm{cm}^{-2}$) on several confined levels. The large DOS coming from the contributions of the individual sub-bands enhances the electron compressibility and facilitate the instability. This effect is stronger when $d_{xz,yz}$ sub-bands start to be filled because they have a rather large DOS. The relevance of the $d_{xz,yz}$ levels has already been asserted in Hartree-Fock calculations [80] and seems to be experimentally supported [57]. The filling of these levels typically starts when the system enters the PS dome upon increasing V_g, and rapidly leads to increasingly more abundant regions with locally higher electron density. We speculate that this corresponds to the observed increase of high-mobility carriers [9, 24]. If one is willing to accept the idea that only regions with higher electron densities can become superconducting, the increasingly large number of these regions can account for the occurrence of an inhomogeneous superconducting state above some (percolative) threshold [26, 16, 24, 25, 22].

Interestingly, in a rather large range of n_0 values, the system exits the PS dome in the vicinity of the critical point located at $n_0^c \approx 0.0475$ el/u.c. and $V_g^c \approx -90\,\mathrm{V}$ for back-gating (see blue line trajectories in figure 3.4). These values are well within the range experimentally found for the gate potentials of the superconducting onsets [30, 9], indicating that the real systems exit the PS dome not far from the QCP. This also suggests that decreasing V_g the electrons in the LXO/STO interface should eventually display some signatures of critical behavior, where superconductivity will likely be affected by the strong quantum density fluctuations. The behavior of superconducting critical fluctuations in proximity of the density QCP will be discussed in detail in chapter 4.

3.3 Concluding remarks

In conclusion, we identified a mechanism of electron-driven PS. While the details of the phase-separated region also depend on the short-range rigidity of the system, the existence and robustness of the PS is on a firm ground and can be responsible for the strong inhomogeneity observed at LXO/STO interfaces. This mechanism can also cooperate with extrinsic defects (e.g., domain walls [60, 15]) or with other intrinsic mechanisms based on short range interactions, like the Rashba spin-orbit coupling [27, 19] or the local electronic effects of oxygen vacancies [81], which are specific of the LXO/STO systems. On the other hand, owing to the rather generic character of the mechanism considered here, our work might also be relevant for other surface or interface states, like, e.g., in topologic insulators, where inhomogeneities turn out to be quite common.

Chapter 4

Density driven superconducting critical fluctuations

In section 1.6 we discussed briefly the quantum critical regime controlled by an external magnetic field B (see also reference [8]), enlightening the presence of two different doping regimes, identified by Region I and Region II in figure 1.23 and characterized by the same critical exponents z and ν.
In that case the critical behavior was explained assuming the presence of static superconducting puddles, with a well established amplitude of the superconducting order parameter and a fluctuating phase. According to the results of chapter 3, these puddles originate from a first order phase transition. However, puddles can be regarded as static objects only when the system is well inside the phase separated region and far from the critical gate voltage (identified in figure 3.4 by a red point where the domes close). Around that value, one expects that density fluctuations become relevant and the behavior of the system is ruled by a second order phase transition.

In this chapter we consider this regime of voltages and analyze the quantum critical point (QCP) of the superconducting 2DEG at LXO/STO interfaces when using V_g, instead of B, as the control parameter of the Hamiltonian (see figure 1.19 in chapter 1). We address the possibility that a new type of fluctuations occurs in superconductors with an anomalous dynamics. In particular we suggest that the superconducting-to-metal transition, driven by the gating V_g, displays anomalous scaling properties, which can be explained by superconducting critical fluctuations controlled by an electronic phase separation critical point. Performing a Finite Size Scaling (FSS) analysis, we found that the product $z\nu$ (ν is the correlation length exponent and z the dynamical one) is $z\nu \sim 3/2$. When the superconducting transition takes place at a gating close to the value for which the system enters the phase separation dome, we claim that the fluctuations acquire an anomalous dynamics with $z = 3$, since they couple to density ones, and that $\nu = 1/2$ correspond to the mean-field value. This scenario strongly departs from the one that is conventionally seen in disordered 2D superconductors, where phase fluctuations dominate and $z = 1$ because of long-range Coulomb interactions.

4.1 Two merging quantum critical points

In chapter 3 it was shown that, in a rather large range of values of the mobile electrons density, n^m, the 2DEG at at LXO/STO interfaces displays a negative inverse electronic compressibility $\partial\mu/\partial n < 0$ (μ is the chemical potential), which leads to a spontaneous phase separation between high and low electronic density regions. A phase diagram emerges (figure 3.4) with an electronic phase separation region ended by a QCP. This quantum critical point can be reached upon changing the gating, V_g, to a certain critical value V_g^{ps}. A similar scenario also characterize the superconducting phase when the system is cooled at very low temperature: again, using the gating as a control parameter, it is possible to drive a superconducting-to-metal transition which ends in a QCP at zero temperature (figure 1.19 of chapter 1), when V_g equals a critical value V_g^{sc}. Even though, in principle, the two QCPs are reached at a different gating, we showed in the previous chapters that there are good reasons for the density QCP to be near to the QCP for superconductivity, which means that $V_g^{sc} \simeq V_g^{ps}$. According to our model, the phase separation occurs because of the d-bands and sub-bands in the quantum well are non-rigid and the spacing between sub-bands, together with the energy of the bottom of the conduction band, change with the filling of the well. The lowest bands are of d_{xy} character and lie close to the interface. Upon doping, the populated upper band can be of d_{xy} character [9] or d_{xz}/d_{yz} one[1] [80, 92] or even a mixture between them through Spin Orbit Coupling. Whatever the scenario is, the common feature is that this band strongly delocalizes within the STO substrate when populated, which favors superconductivity [9, 24]. In figure 4.1 (d) it is reported the extension of the 2DEG as a function of gate voltage, calculated using the self-consistent method presented in chapter 3. When entering the phase separated domain, the system separates in region of electron density n_{s1} where, according to the interpretation given in chapter 2, only low-mobility carriers exist, and regions of density n_{s2}, where both low-mobility and high-mobility carriers exist. While the spatial extension of the band related to n_{s1} does not evolve significantly, the one related to n_{s2} increases rapidly beyond 4 nm, where the superconducting phase shows up [9]. A Ginzburg-Landau approach extended to a diffusion model confirms this scenario and the occurrence of an electronic instability in this case [23].

---

[1] Our numerical study, that we presented in chapter 3, suggests that phase separation occurs as soon as d_{xz}/d_{yz} bands are filled.

Consequently, phase separation and superconductivity appear in the same region of the phase diagram. In addition, superconductivity can favor phase separation by itself, when the critical temperature T_c depends (as it is the case) on the electron density n_s: if the pairing energy Δ is a function of n_s, the system may gain energy by forming superconducting regions of high density in non superconducting low density ones. Conversely, the electronic compressibility is strongly enhanced near a density-driven superconducting critical line $T_c(n)$. Thus, the QCP related to the phase separation dome (where compressibility diverges), is attracted by the superconducting QCP (where $T_c(n)$ vanishes), and the two tend to merge [23].

4.2 Superconductivity in density fluctuating droplets

The microscopic BCS theory of superconductivity and its phenomenological version, the Ginzburg-Landau theory in mean field approximation, describe the emergence of a quantum coherent phase out of a Fermi liquid metal, with a large electronic density, a well established Fermi surface and a nearly constant density of states at the Fermi level. As the temperature T approaches the critical temperature T_c (which relates to the density of states at the Fermi level), thermal fluctuations of both amplitude and phase increase. In proximity of the phase transition the only relevant scale is the spatial coherence length ξ, which scales with the distance to the critical temperature as $\xi \propto (T-T_c)^{-\nu}$. The dynamics of the fluctuations are also determined by the coherence length as $\tau \propto \xi^z$, and they slow down with a critical exponent $z = 2$. Here τ is the characteristic lifetime of the fluctuations. In a quantum phase transition, the superconducting critical point is approached by varying continuously a parameter K of the Hamiltonian, keeping the system at zero temperature. As K equal the critical value K_c [95], superconductivity is destroyed and the system becomes metallic. In dirty two dimensional superconductors, the reduced screening of the Coulomb electron-electron repulsion may lead to pair breaking [41] or to direct localization of the superconducting pairs [43], with Coulomb interaction rendering the superfluid density weaker and thus the conjugated phase fluctuations softer. In this scenario the physics is dominated by phase fluctuations and the system is described, close to the phase transition, by a classical XY model. Fisher argued that, in this strongly localized systems, the Coulomb interactions are restored and the superconductor-to-insulator transition has a dynamical exponent $z = 1$ [43]. Other scenarios have been proposed in recent years [13, 38], where disorder destroys coherence approaching the transition and inhomogeneities develop even in structurally homogeneous thin films. The dynamical exponents associated with these transitions are $z = 1$ or $z = 2$.

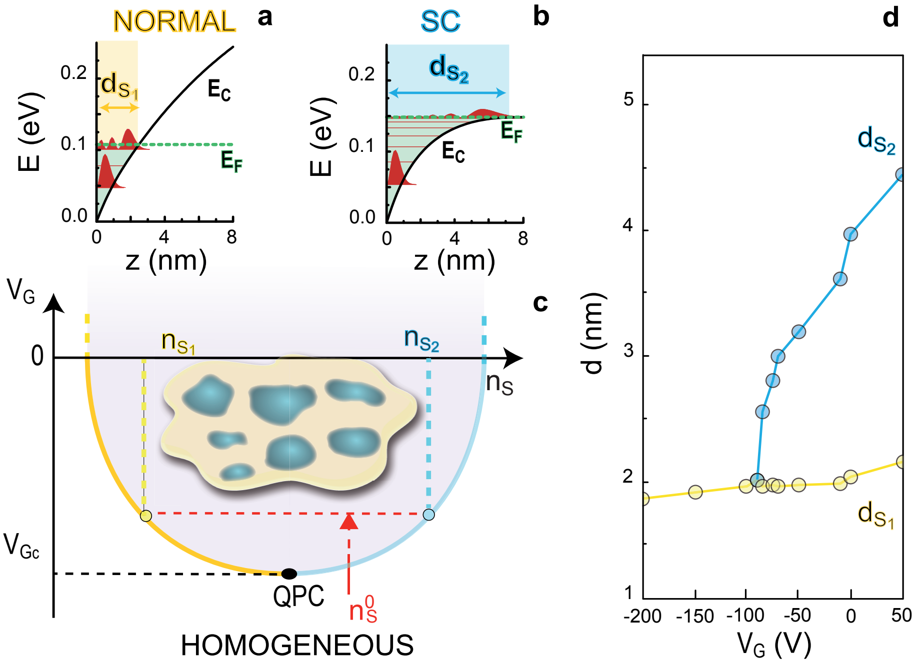

Fig. 4.1 (c) : Sketch of the electronic phase separation at oxide interfaces. A phase separation line ending by a density QCP marks out the homogeneous from the phase separated zone (in purple) in the V_G vs n_s phase diagram. For a sample with a density n_s (red arrow) at $V_G < V_{Gc}$, the system has an homogeneous density. When further increasing V_G, it enters the phase separated zone, and decomposes into low density n_{s1} (yellow broken line) and high density n_{s2} (blue broken line) droplets, as sketched within the dome. In the low density droplets, carriers are localized near the interface and remain normal (a), while in the high density ones, carriers extend far from the interface (b) and display superconductivity [9]. (d) : Calculated gas extension d as a function of V_G. Beyond V_{Gc} (which for the parameters chosen in the theoretical calculations occurs above $V_{Gc} \approx -100V$), d remains constant for the low density regions at $n = n_{s1}$ (yellow dots) , and increases in high density droplets at $n = n_{s2}$ (blue dots)[92].

In figure 4.2 (a) the sheet resistance R_s of a LaAlO$_3$/SrTiO$_3$ sample is plotted as a function of the temperature T for different gate voltages V$_g$. As seen in figure 4.2 (c), the superconducting state is progressively destroyed in favor of a weakly localizing metal [10, 8]. The superconducting and the normal states are separated by a plateau in the resistivity curves at the lowest temperatures, which develops for a critical value of the sheet resistance of $R_c \sim 2.57\ k\Omega/\Box$. A possible sign of quantum phase transition is revealed when R_s is plotted as a function of V$_g$ for different temperatures, revealing a clear crossing point at $R_c \simeq 2.57\ k\Omega/\Box$, $V_{\mathrm{Gc}} = -78.5\ V$ (figure 4.3 (a)). A finite size scaling analysis (FSS) of the data in this region in made on figure 4.3 (b). All the sheet resistance data from 35 to 110 mK collapse onto a single function

$$\frac{R_s}{R_c} = F\left(\frac{|V_{\mathrm{G}} - V_{\mathrm{Gc}}|}{T^{1/z\nu}}\right) \tag{4.1}$$

if $z\nu \sim 1.6 \pm 0.1$. This critical exponent can then be retrieved (figure 4.3 (c)) by a scaling procedure.

A similar behavior characterize the 2DEG at the LaTiO$_3$/SrTiO$_3$ interface. Figure 4.4 (a) displays R_s as a function of temperature T for different gate voltages: again, a critical sheet resistance $R_c \sim 2.35\ k\Omega/\Box$, indicated by the crossing point in figure 4.4 (b), separates the superconducting phase from the metallic one. The FSS analysis of the low temperature data points toward a QPT with a critical exponent $z\nu \sim 1.6 \pm 0.1$ (figure 4.4 (c)).

The exponent $z\nu \sim 3/2$ is somewhat surprising, and rarely found in the literature. The most common reported values are close to $z\nu = 2/3$, $z\nu = 4/3$ or $z\nu = 7/3$ [51]. Assuming a dynamical exponent $z = 1$, the spatial exponent $\nu = 2/3$ would therefore correspond to a clean (2+1)D XY model, coherent with a scenario where phase fluctuations dominate the behavior of the system in the vicinity of the transition, with an enhanced dimension for the quantum character of the transition. Under the same assumption $z = 1$, $\nu = 4/3$ and $\nu = 7/3$ are typical of a classical, respectively quantum percolating behavior in highly disordered systems. The main assumption[2] in these arguments is that the dynamical exponent z equals 1, because of enhanced long range Coulomb interactions when the system becomes insulating [43].

Following the same assumption $z = 1$, we were not able to perform a satisfying FSS with the above quoted ν exponents in none of our samples. Moreover, since the non-superconducting phase is a weakly localizing metal and not an insulator [10, 8], screening effects should be substantial and the exponent $z = 1$ could not be justified invoking long

---

[2] Experiments of Yazdani et al. [103] in amorphous MoGe films and Markovic et al. [71] in a-Bi layers confirmed the validity of this assumption.

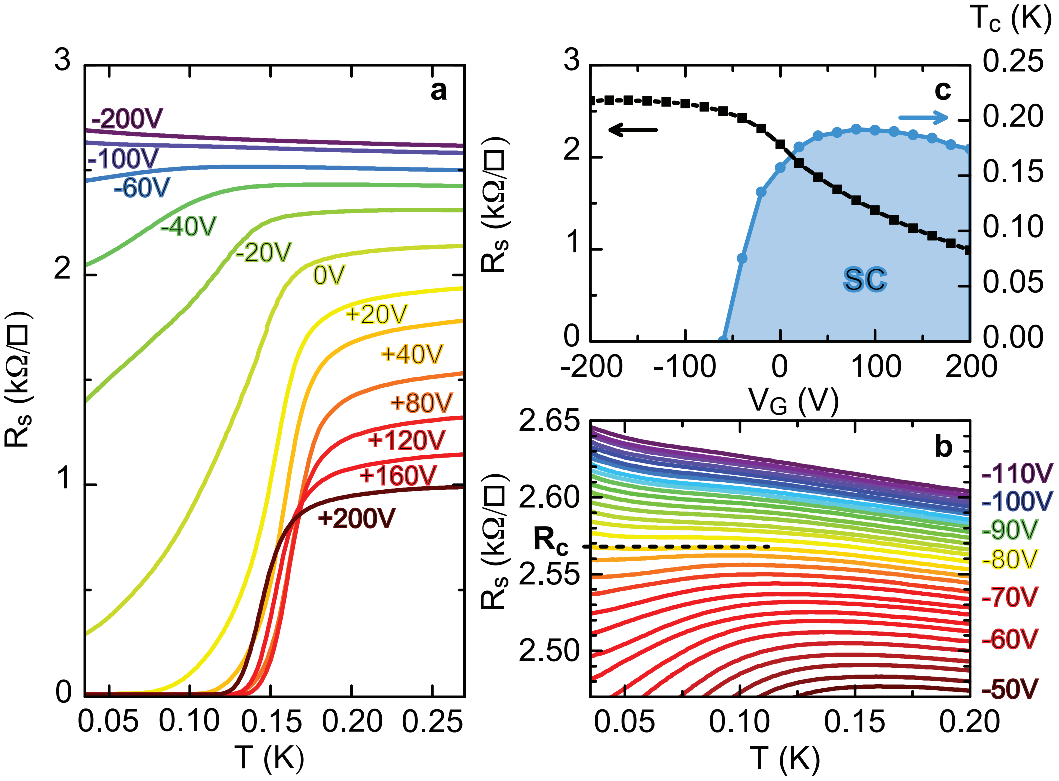

Fig. 4.2 $LaAlO_3/SrTiO_3$ interface : (a) Resistance per square R_s as a function of temperature for different gate voltages V_G from $+200V$ to $-200V$. (b) Zoom in the low temperature region, where a plateau develops for $R_c \sim 2.57k\Omega/\square$. (c) Resistance per square R_s (left axis) and superconducting critical temperature T_c (right axis) as a function of the gate voltage V_G. The superconducting region (SC) is colored in blue.

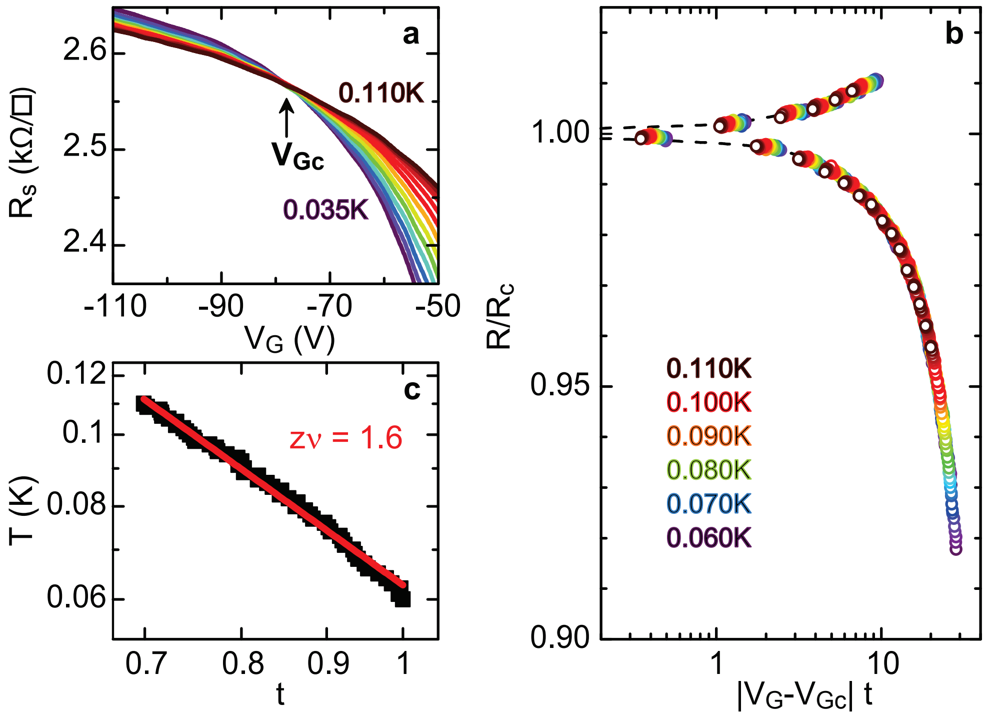

Fig. 4.3 $LaAlO_3/SrTiO_3$ interface : (a) R_s as a function of the gate voltage V_G for different temperatures from 0.035 to 0.11 K. The crossing point is ($R_c \sim 2.57k\Omega/\Box$,$V_{Gc} = -78.5V$). (b) Finite size scaling plot R_s/R_c as a function of $|V_G - V_{Gc}|t$ (see text for the definition of t). (c) Temperature behavior of the scaling parameter t (see text). The power law fit gives $z\nu \sim 1.6 \pm 0.1$

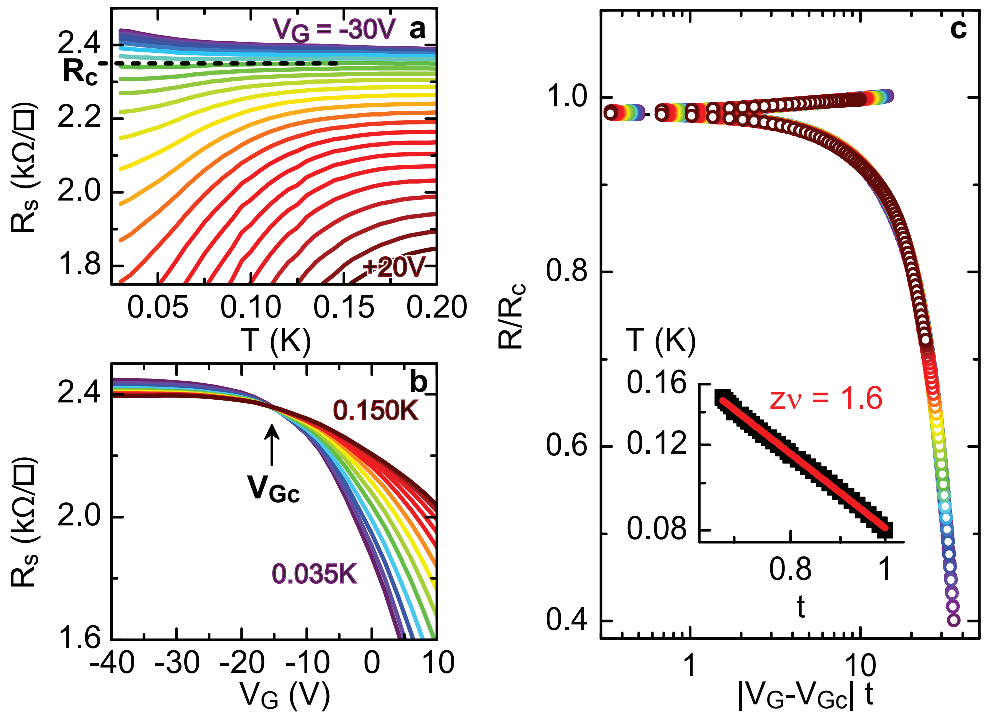

Fig. 4.4 LaTiO$_3$/SrTiO$_3$ interface : (a) Resistance per square R_s as a function of temperature between 0.03 and 0.2 K for different gate voltages from $+30V$ to $-20V$. A plateau is observed for $R_c \sim 2.35k\Omega/\square$ (b) R_s as a function of the gate voltage V_G for different temperatures from 0.035 to 0.15 K. (b) The crossing point is ($R_c = \sim 2.35k\Omega/\square, V_\mathrm{Gc} = -15V$). (c) Finite size scaling plot R_s/R_c as a function of $|V_G - V_\mathrm{Gc}|t$ (see text for the definition of t). Inset : temperature behavior of the scaling parameter t (see text). The power law fit gives $z\nu \sim 1.6 \pm 0.1$

range Coulomb forces. Indeed the highly metallic character of these materials leaves the possibility open that the $z = 1$ critical behavior usually invoked for the superconductor to insulator transition could be replaced by an over damped dynamics with $z > 1$. Thus, in the following, we investigate an alternative scenario, in which the dynamical critical behavior of the superconducting fluctuations is imposed by the coupling to nearly critical density fluctuations with $z = 3$. In this scheme, the experimental observation of $z\nu \sim 3/2$ arises from a $z = 3$ dynamical critical behavior of the superconducting fluctuations together with a mean-field like exponent $\nu = 1/2$. In figure 4.1 (c) is reported a sketch of the phase diagram of the electronic density as a function of the gate voltage. At low density (very negative V_g), the electronic system is homogeneous, and becomes phase separated when entering the instability dome. In this region, static clusters of high density n_{2s} are embedded in low-density regions of density n_{1s}, whose proportions are given by the Maxwell construction. This intrinsic electronic inhomogeneity accounts for observed inhomogeneous superconducting properties (see chapter 2): indeed, if n_{2s} is high enough, the islands can be superconducting, embedded in normal zone of density n_{1s}. The dome ends at a Quantum Critical Point (QCP), which is the analogous of the critical point of the classical liquid-gas phase diagram. In the vicinity of the QCP, critical density fluctuations are ruled by a $z = 3$ dynamics. This substantially increases the effective dimensionality $D+z$ and the system therefore displays a mean-field exponent $\nu = 1/2$. As we mentioned above, it is reasonable to make the hypothesis that superconductivity is destroyed at the critical gate voltage V_{Gc} of the QCP . In other words, this voltage corresponds to the beginning of the phase separation *and* the occurrence of superconductivity (in high density droplets). In that case, superconducting fluctuations develop on density fluctuating droplets, and therefore acquire their dynamics with $z = 3$: consequently $\nu = 1/2$, and $z\nu = 3/2$.

4.2.1 Density driven superconducting transition in other systems

A density driven transition of a 2D superconductor to a weakly localized metal or an insulator is quite uncommon in the literature. Focusing on critical exponents extracted from a complete FSS analysis, a few results are found in the literature. Parendo et al. [79] reported $z\nu \sim 2/3$ in amorphous Bi films, corresponding to a clean (2+1)D XY model in this highly metallic conventional s-p compound. In 7 u.c. thick $YBa_2Cu_3O_7$ layers[43], $z\nu \sim 2.2$ has been found corresponding to quantum percolation, which is not surprising in highly disordered thin films with up to 6 u.c. of dead layer. However, in 1 to 2 u.c. thick $La_{2-x}Sr_xCuO_4$ samples, Bollinger et al. found exactly $z\nu = 3/2$ [12], while Garcia-Barriocanal et al. reported $z\nu$ from 1.4 to 1.8 for 4 u.c $La_{2-x}Sr_xCuO_4$ thin films [49], not far from it. This system shares similarities with the LAO/STO or LTO/STO interfaces, such as an extreme 2D character (thickness of a few unit cells) and a low electronic density at the transition (in the $10^{13}\, e^-/cm^2$ range). It is worthwhile mentioning that the magnetic field driven transition looks also very similar in the two systems, with two critical regimes in temperature [8, 93]. There is no report of negative compressibility induced phase separation in $La_{2-x}Sr_xCuO_4$, but other intrinsic electronic inhomogeneities have been found such as fluctuating Charge Density Waves [50]. The coupling of the superconducting fluctuations to other critical electronic modes near Charge Density Waves [28], stripes or fermionic nematic phases [45] QCP may lead to anomalous dynamics as well. It would be interesting to explore more widely this possibility in cuprates, Fe-pnictides or other exotic superconductors.

4.3 Concluding remarks

In conclusion, we studied the superconductor to metallic phase transition in $LaAlO_3/SrTiO_3$ and $LaTiO_3/SrTiO_3$ interface as a function of the electronic density tuned by a gate voltage. The critical exponents product $z\nu \sim 3/2$ is compatible with density driven fluctuations, where the superconducting fluctuations are coupled to density ones in the vicinity of an electronic phase separation critical point. This new type of fluctuations may be observed in other 2D superconductors and perhaps also in superfluids such as ^4He on aerogels, where a similar $z\nu$ has been found [33].

Chapter 5

Conclusions

Although experimental evidences suggest that the two-dimensional electron gas at LXO/STO interfaces is inhomogeneous, the size of the inhomogeneities and their role in the transport properties of the 2DEG are still largely debated within the oxide community. Inhomogeneities at the nanometric and micrometric scale seem to coexist, despite their different origin: while the micrometric ones, revealed by the occurrence of striped textures in the current distribution and in the surface potential, are reasonable accounted for by structural (e.g. tetragonal) distortions in the $SrTiO_3$, nanometric inhomogeneities have a controversial and largely unexplained origin. In addition, inhomogeneities appear both in the metallic and in the superconducting state, but whether they come from the same microscopic mechanism or completely different ones, this was not clear at all.

In this thesis we propose a possible answer to these questions by collecting together the most relevant experimental evidences about LXO/STO, which up to now have been considered only separately, and interpreting them within an overall coherent theoretical framework, which relies on the concept of electronic phase separation. We also provide new compelling evidences of the inhomogeneous character of the 2DEG, giving further proofs of the robustness of our picture.

The starting point of our analysis is the consideration that the metal-to-superconductor transition in these systems is characterized by sheet resistance curves which display a very large width at low temperature, and saturate to a plateau with finite resistance in the low doping regime. This behavior, inexplicable by any reasonable superconducting fluctuations, is instead a clear indication of the percolating character of the transition. This led us to formulate the phenomenological scenario of an electron gas consisting of metallic islands embedded in a metallic sea, which become superconducting below a randomly distributed critical temperature.

In this framework, the sheet resistance curves of LTO/STO interfaces are well reproduced by EMT or by a RRN for an inhomogeneous 2DEG with a substantial filamentary character. Fitting the experiments, we were able to extract the random distribution of T_c at various V_g (i.e. at various carrier densities). A similar approach was adopted to fit the micrometrically averaged superfluid stiffness and the pseudo-gap in tunneling spectra of LAO/STO, convincing us of the reliability of our scenario.

However, this picture is still too simplistic to give a detailled description of magneto-transport experiments, which address the presence of two kind of carriers with low and high mobility, and it is unable to explain why the the superconductivity seems to be related to the presence of high-mobility carriers, appearing when the electron density is tuned above a threshold value by gate voltage. Therefore, in order to deal with multiple species of carriers, we add another reasonable ingredient to our model, making the hypothesis that the presence of low- and high-mobility carriers occurs according to a not uniform spatial distribution: in the metallic islands both carrier coexist, while the metallic sea has only the low-mobility ones. We then modify the EMT to include the two kinds of carriers and use it to analyze the magneto-transport experiments in LTO/STO oxide interfaces. It turns out that the mobilities of the two species are almost independent of the gate voltage. Thus, the enhancement of conductivity observed around $V_g = 0\,\mathrm{V}$ and the change in the slope of the Hall resistance at high magnetic fields occur because a finite fraction of regions with higher carrier density, hosting high-mobility carriers, appears around this gate voltage. This analysis also confirms that the high-mobility carriers have a lower density that low-mobility ones, as reported by Biscaras et al. [9].

At this point, it is quite natural to recognize that superconductivity is related to the occurrence of high mobility carriers. Assuming phenomenologically an effective two-band model with superconductivity triggered by the presence of few high-mobility carriers[1], locally filling the highest-energy band, we are able to account for the density dependence of the intra-puddle T_c within a simple BCS weak coupling scheme. As an important by-product, we find that the range of variation in V_g of the average intra-puddle T_c is directly related (via the chemical potential μ) to the cut off energy scale, $\hbar\omega_0$. Taking this value as a crude estimate of the typical energy scale of the pairing mediator, we find that this is compatible with phonon-mediated superconductivity.

Once we have proved that our phenomenological scenario is able to fit transport experiments and it does not show evident internal contradditions, we can formulate a possible justification of the inhomogeneous character of the 2DEG and the appearing of two type

---

[1] In agreement with direct superfluid density measurements (e.g. in LAO/STO), where it is found that only a small fraction of the total electron density forms the superconducting state.

of carriers whose distribution is not uniform in space. The mechanism that we identified is based on an electron-driven phase separation.

Electrons in the 2DEG experience a strong electric field directed perpendicularly to the interface, which is responsible of the potential well that keeps the gas confined. Since the potential well depends on the electron density, a larger number of electrons producing a stronger electric field, it turns out that the band structure is non rigid and evolves as a function of the electron density. Numerical calculations demonstrate that in a wide range of reasonable parameters, compatible with the experiments, the non-rigidity determines a negative compressibility in the uniform system, which it avoids by phase separation. The densities of the phase separated regions are thus found by Maxwell construction and depend on the doping level.

The phase separation scenario also explains the inhomogeneous distribution of low- and high-mobility carriers, and their behavior as a function of the doping level: since the electronic instability is developed as soon as the Fermi energy reaches the STO high energy bands[2], whenever the system is phase separated, the Maxwell construction ensures that in the region of high electron density the upper d$_{xz,yz}$ bands are populated. But d$_{xz,yz}$ electrons are precisely the high mobility carriers [9] and the phenomenological assumption of an effective two-band model made above is now justified theoretically. The numerical solution of the Schrödinger-Poisson equations (chapter 3) also confirms that albeit the details of the phase-separated region are model dependent (e.g. they depend from the functional form of short-range potential between the countercharges), the existence and robustness of the phase separation is on a firm ground and can be responsible for the strong inhomogeneity observed at LXO/STO interfaces. Of course the this mechanism can also cooperate with extrinsic defects (e.g., domain walls) or with other intrinsic mechanisms based on short range interactions, like the Rashba spin-orbit coupling or the local electronic effects of oxygen vacancies, which are specific of the LXO/STO systems.

Finally, we study the superconductor-to-metallic phase transition in LXO/STO interfaces as a function of the electronic density tuned by a gate voltage. According to the mechanisms outlined above, phase separation and superconductivity appear in the same region of the phase diagram. This can be rephrased more rigorously (see reference [23]) by saying that the quantum critical point related to the phase separation dome (where compressibility diverges), is attracted by the superconducting quantum critical point (where the critical temperature $T_c(n)$ vanishes), and the two tend to merge . We prove that the proximity of the two quantum critical points leads to anomalous dynamics of the superconducting quantum fluctuations, characterized by the critical exponents product $z\nu \sim 3/2$. This value

---

[2] See chapter 3

is compatible with density driven fluctuations, where the superconducting fluctuations are coupled to density ones in the vicinity of an electronic phase separation critical point. This new type of fluctuations may be observed in other 2D superconductors and perhaps also in superfluids such as ^{4}He on aerogels, where a similar $z\nu$ has been found [33].

References

[1] Aharony, A. and Stauffer, D. (2003). *Introduction to percolation theory*. Taylor & Francis.

[2] Ariando, Wang, X., Baskaran, G., Liu, Z. Q., Huijben, J., Yi, J. B., Annadi, a., Barman, a. R., Rusydi, a., Dhar, S., Feng, Y. P., Ding, J., Hilgenkamp, H., and Venkatesan, T. (2011). Electronic phase separation at the $LaAlO_3/SrTiO_3$ interface. *Nature communications*, 2:188.

[3] Arkhincheev, V. E. (2000). Quantum Hall Effect in Inhomogeneous Media: Effective Characteristics and Local Current Distribution. *JETP*, 91(2):407–415.

[4] Banerjee, S., Erten, O., and Randeria, M. (2013). Ferromagnetic exchange, spin–orbit coupling and spiral magnetism at the LaAlO3/SrTiO3 interface. *Nature Physics*, 9(10):626–630.

[5] Bert, J. a., Kalisky, B., Bell, C., Kim, M., Hikita, Y., Hwang, H. Y., and Moler, K. a. (2011). Direct imaging of the coexistence of ferromagnetism and superconductivity at the $LaAlO_3/SrTiO_3$ interface. *Nature Physics*, 7(10):767–771.

[6] Bert, J. a., Nowack, K. C., Kalisky, B., Noad, H., Kirtley, J. R., Bell, C., Sato, H. K., Hosoda, M., Hikita, Y., Hwang, H. Y., and Moler, K. a. (2012). Gate-tuned superfluid density at the superconducting $LaAlO_3/SrTiO_3$ interface. *Physical Review B*, 86(6):060503.

[7] Bi, F., Huang, M., Wung Bark, C., Ryu, S., Lee, S., Eom, C.-B., Irvin, P., and Levy, J. (2013). Electro-Mechanical Response of Top-Gated LaAlO3/SrTiO3 Heterostructures. *ArXiv e-prints*.

[8] Biscaras, J., Bergeal, N., Hurand, S., Feuillet-Palma, C., Rastogi, a., Budhani, R. C., Grilli, M., Caprara, S., and Lesueur, J. (2013). Multiple quantum criticality in a two-dimensional superconductor. *Nature materials*, 12(6):542–8.

[9] Biscaras, J., Bergeal, N., Hurand, S., Grossetête, C., Rastogi, a., Budhani, R. C., LeBoeuf, D., Proust, C., and Lesueur, J. (2012). Two-Dimensional Superconducting Phase in LaTiO_{3}/SrTiO_{3} Heterostructures Induced by High-Mobility Carrier Doping. *Physical Review Letters*, 108(24):247004.

[10] Biscaras, J., Bergeal, N., Kushwaha, a., Wolf, T., Rastogi, a., Budhani, R. C., and Lesueur, J. (2010). Two-dimensional superconductivity at a Mott insulator/band insulator interface LaTiO3/SrTiO3. *Nature communications*, 1:89.

[11] Biscaras, J., Hurand, S., Feuillet-Palma, C., Rastogi, a., Budhani, R. C., Reyren, N., Lesne, E., Lesueur, J., and Bergeal, N. (2014). Limit of the electrostatic doping in two-dimensional electron gases of $LaXO_3$(X = Al, Ti)/$SrTiO_3$. *Scientific reports*, 4:6788.

[12] Bollinger, a. T., Dubuis, G., Yoon, J., Pavuna, D., Misewich, J., and Božović, I. (2011). Superconductor-insulator transition in $La_{2-x}Sr_xCuO_4$ at the pair quantum resistance. *Nature*, 472(7344):458–60.

[13] Bouadim, K., Loh, Y. L., Randeria, M., and Trivedi, N. (2011). Single- and two-particle energy gaps across the disorder-driven superconductor–insulator transition. *Nature Physics*, 7(11):884–889.

[Brezis] Brezis, H. *Analysis, Sobolev Spaces and Partial Differential Equations*. Springer-Verlag.

[15] Bristowe, N. C., Fix, T., Blamire, M. G., Littlewood, P. B., and Artacho, E. (2012). Proposal of a one-dimensional electron gas in the steps at the LaAlO3-SrTiO3 interface. *Physical review letters*, 108(16):166802.

[16] Bucheli, D., Caprara, S., Castellani, C., and Grilli, M. (2013). Metal–superconductor transition in low-dimensional superconducting clusters embedded in two-dimensional electron systems. *New Journal of Physics*, 15(2):023014.

[17] Bucheli, D., Caprara, S., and Grilli, M. (2015a). Pseudo-gap as a signature of inhomogeneous superconductivity in oxide interfaces. *Superconductor Science and Technology*, 28(4):045004.

[18] Bucheli, D., Caprara, S., and Grilli, M. (2015b). Pseudo-gap as a signature of inhomogeneous superconductivity in oxide interfaces. *Superconductor Science and Technology*, 28(4):045004.

[19] Bucheli, D., Grilli, M., Peronaci, F., Seibold, G., and Caprara, S. (2014). Phase diagrams of voltage-gated oxide interfaces with strong Rashba coupling. *Physical Review B*, 89(19):195448.

[20] Burt, M. G. (1992). The justification for applying the effective-mass approximation to microstructures. *Journal of Physics: Condensed Matter*, 4(32):6651.

[21] Cantoni, C., Gazquez, J., Miletto Granozio, F., Oxley, M. P., Varela, M., Lupini, A. R., Pennycook, S. J., Aruta, C., di Uccio, U. S., Perna, P., and Maccariello, D. (2012). Electron transfer and ionic displacements at the origin of the 2D electron gas at the LAO/STO interface: direct measurements with atomic-column spatial resolution. *Advanced materials (Deerfield Beach, Fla.)*, 24(29):3952–7.

[22] Caprara, S., Bergeal, N., Lesueur, J., and Grilli, M. (2015a). Interplay between density and superconducting quantum critical fluctuations. *Journal of physics. Condensed matter : an Institute of Physics journal*, 27(42):425701.

[23] Caprara, S., Bergeal, N., Lesueur, J., and Grilli, M. (2015b). Interplay between density and superconducting quantum critical fluctuations. *Journal of Physics: Condensed Matter*, 27(42):425701.

[24] Caprara, S., Biscaras, J., Bergeal, N., Bucheli, D., Hurand, S., Feuillet-Palma, C., Rastogi, a., Budhani, R. C., Lesueur, J., and Grilli, M. (2013). Multiband superconductivity and nanoscale inhomogeneity at oxide interfaces. *Physical Review B*, 88(2):020504.

[25] Caprara, S., Bucheli, D., Grilli, M., Biscaras, J., Bergeal, N., Hurand, S., Feuillet-Palma, C., Lesueur, J., Rastogi, a., and Budhani, R. C. (2014). Inhomogeneous Electron Gas At Oxide Interfaces With Strong Rashba Spin–Orbit Coupling. *Spin*, 04(01):1440004.

[26] Caprara, S., Grilli, M., Benfatto, L., and Castellani, C. (2011). Effective medium theory for superconducting layers: A systematic analysis including space correlation effects. *Physical Review B*, 84(1):014514.

[27] Caprara, S., Peronaci, F., and Grilli, M. (2012). Intrinsic Instability of Electronic Interfaces with Strong Rashba Coupling. *Physical Review Letters*, 109(19):196401.

[28] Castellani, C., Di Castro, C., and Grilli, M. (1995). Singular quasiparticle scattering in the proximity of charge instabilities. *Phys. Rev. Lett.*, 75:4650–4653.

[29] Caviglia, A. D., Gabay, M., Gariglio, S., Reyren, N., Cancellieri, C., and Triscone, J.-M. (2010). Tunable rashba spin-orbit interaction at oxide interfaces. *Phys. Rev. Lett.*, 104:126803.

[30] Caviglia, a. D., Gariglio, S., Reyren, N., Jaccard, D., Schneider, T., Gabay, M., Thiel, S., Hammerl, G., Mannhart, J., and Triscone, J.-M. (2008). Electric field control of the LaAlO3/SrTiO3 interface ground state. *Nature*, 456(7222):624–7.

[31] Chen, Y., Pryds, N., Koster, G., Sun, J., Stamate, E., Shen, B., Rijnders, G., and Linderoth, S. (2011). Metallic and Insulating Interfaces of Amorphous SrTiO 3 -Based Oxide Heterostructures. *Nano Letters*, pages 3774–3778.

[32] Copie, O., Garcia, V., Bödefeld, C., Carrétéro, C., Bibes, M., Herranz, G., Jacquet, E., Maurice, J.-L., Vinter, B., Fusil, S., Bouzehouane, K., Jaffrès, H., and Barthélémy, a. (2009). Towards Two-Dimensional Metallic Behavior at LaAlO3/SrTiO3 Interfaces. *Physical Review Letters*, 102(21):216804.

[33] Crowell, P. A., Van Keuls, F. W., and Reppy, J. D. (1997). Onset of superfluidity in ^{4}He films adsorbed on disordered substrates. *Phys. Rev. B*, 55:12620–12634.

[34] De Luca, G., Rubano, A., Gennaro, E. D., Khare, A., Granozio, F. M., di Uccio, U. S., Marrucci, L., and Paparo, D. (2014). Potential-well depth at amorphous-LaAlO3/crystalline-SrTiO3 interfaces measured by optical second harmonic generation. *Applied Physics Letters*, 104(26):261603.

[35] Delugas, P., Filippetti, A., Fiorentini, V., Bilc, D. I., Fontaine, D., and Ghosez, P. (2011). Spontaneous 2-dimensional carrier confinement at the *n*-type $\mathrm{srtio}_3/\mathrm{laalo}_3$ interface. *Phys. Rev. Lett.*, 106:166807.

[36] Di Gennaro, E., Coscia, U., Ambrosone, G., Khare, A., Granozio, F. M., and di Uccio, U. S. (2015). Photoresponse dynamics in amorphous-LaAlO3/SrTiO3 interfaces. *Scientific reports*, 5:8393.

[37] Dikin, D. a., Mehta, M., Bark, C. W., Folkman, C. M., Eom, C. B., and Chandrasekhar, V. (2011). Coexistence of superconductivity and ferromagnetism in two dimensions. *Physical review letters*, 107(5):056802.

[38] Dubi, Y., Meir, Y., and Avishai, Y. (2007). Nature of the superconductor–insulator transition in disordered superconductors. *Nature*, 449(7164):876–880.

[39] Eisenstein, J. P. and West, W. (1994). Compressibility of the two-dimensional electron gas: Measurements of the zero-field exchange energy and fractional quantum Hall gap. *Physical Review B*, 50(3):1760–1779.

[40] Fernandes, R. M., Haraldsen, J. T., Wölfle, P., and Balatsky, A. V. (2013). Two-band superconductivity in doped srtio$_3$ films and interfaces. *Phys. Rev. B*, 87:014510.

[41] Finkelśhtein, A. M. (1987). Superconducting transition temperature in amorphous films. *JETP Letters*, 45:46–49.

[42] Fischer, M. H., Raghu, S., and Kim, E.-A. (2013). Spin–orbit coupling in laalo 3 /srtio 3 interfaces: magnetism and orbital ordering. *New Journal of Physics*, 15(2):023022.

[43] Fisher, M. P. A. (1990). Quantum phase transitions in disordered two-dimensional superconductors. *Phys. Rev. Lett.*, 65:923–926.

[44] Foreman, B. A. (1993). Effective-mass hamiltonian and boundary conditions for the valence bands of semiconductor microstructures. *Phys. Rev. B*, 48:4964–4967.

[45] Fradkin, E., Kivelson, S. a., Lawler, M. J., Eisenstein, J. P., and Mackenzie, A. P. (2010). Nematic Fermi Fluids in Condensed Matter Physics. *Annual Review of Condensed Matter Physics*, 1(1):153–178.

[46] Frank, S. and Howard, W. E. (1967). Properties of Semiconductor Surface Inversion Layers in the Electric Quantum Limit. *Physical Review*, 163(3).

[47] Gabay, M. and Triscone, J.-M. (2013). Oxide heterostructures: Hund rules with a twist. *Nature Physics*, 9(10):610–611.

[48] Galeriu, C. (2005). *$k \cdot p$ theory of semiconductur nanostructures*. PhD thesis, Worchester Polytechnic Institute, Department of Physics.

[49] Garcia-Barriocanal, J., Kobrinskii, A., Leng, X., Kinney, J., Yang, B., Snyder, S., and Goldman, A. M. (2013). Electronically driven superconductor-insulator transition in electrostatically doped la$_2$cuo$_{4+\delta}$ thin films. *Phys. Rev. B*, 87:024509.

[50] Ghiringhelli, G., Tacon, M. L., Minola, M., Mazzoli, C., Brookes, B., Luca, G. M. D., Frano, A., Hawthorn, D. G., He, F., Loew, T., Sala, M., Peets, D. C., Salluzzo, M., Schierle, E., Sutarto, R., Weschke, E., Keimer, B., and Braicovich, L. (2012). Long-range incommensurate charge fluctuations in (Y,Nd)Ba$_2$Cu$_3$O$_{6+x}$. *Science (New York, N.Y.)*, 337(July):821.

[51] Goldman, A. M. (2010). Superconductor-insulator transitions. *International Journal of Modern Physics B*, 24(20n21):4081–4101.

[52] Harris, A. B. (1974). Upper bounds for the transition temperatures of generalized ising models. *Journal of Physics C: Solid State Physics*, 7(17):3082.

[53] Herranz, G., Basletić, M., Bibes, M., Carrétéro, C., Tafra, E., Jacquet, E., Bouzehouane, K., Deranlot, C., Hamzić, A., Broto, J.-M., Barthélémy, A., and Fert, A. (2007). High mobility in laalo$_3$/srtio$_3$ heterostructures: Origin, dimensionality, and perspectives. *Phys. Rev. Lett.*, 98:216803.

[54] Ilani, S. (2013). Private communication.

[55] Innocenti, D., Poccia, N., Ricci, A., Valletta, A., Caprara, S., Perali, A., and Bianconi, A. (2010). Resonant and crossover phenomena in a multiband superconductor: Tuning the chemical potential near a band edge. *Phys. Rev. B*, 82:184528.

[56] Jasnow, D. and Wortis, M. (1968). High-temperature critical indices for the classical anisotropic heisenberg model. *Phys. Rev.*, 176:739–750.

[57] Joshua, A., Pecker, S., Ruhman, J., Altman, E., and Ilani, S. (2012). A universal critical density underlying the physics of electrons at the LaAlO$_3$/SrTiO$_3$ interface. *Nature communications*, 3:1129.

[58] Kahn, A. H. and Leyendecker, A. J. (1964). Electronic energy bands in strontium titanate. *Phys. Rev.*, 135:A1321–A1325.

[59] Kalabukhov, A. S., Boikov, Y. A., Serenkov, I. T., Sakharov, V. I., Popok, V. N., Gunnarsson, R., Börjesson, J., Ljustina, N., Olsson, E., Winkler, D., and Claeson, T. (2009). Cationic disorder and phase segregation in laalo$_3$/srtio$_3$ heterointerfaces evidenced by medium-energy ion spectroscopy. *Phys. Rev. Lett.*, 103:146101.

[60] Kalisky, B., Spanton, E. M., Noad, H., Kirtley, J. R., Nowack, K. C., Bell, C., Sato, H. K., Hosoda, M., Xie, Y., Hikita, Y., Woltmann, C., Pfanzelt, G., Jany, R., Richter, C., Hwang, H. Y., Mannhart, J., and Moler, K. a. (2013). Locally enhanced conductivity due to the tetragonal domain structure in LaAlO3/SrTiO3 heterointerfaces. *Nature materials*, 12(12):1091–5.

[61] Karim M. Rabe, Charles H. Ahn, J.-M. T. (2007). *Physics of Ferroelectrics: A Modern Perspective (Topics in Applied Physics)*. Springer, Berlin.

[62] Kim, J. S., Seo, S. S. A., Chisholm, M. F., Kremer, R. K., Habermeier, H.-U., Keimer, B., and Lee, H. N. (2010). Nonlinear hall effect and multichannel conduction in latio$_3$/srtio$_3$ superlattices. *Phys. Rev. B*, 82:201407.

[63] Kisker, J. and Rieger, H. (1997). Bose-glass and mott-insulator phase in the disordered boson hubbard model. *Phys. Rev. B*, 55:R11981–R11984.

[64] Koonce, C. S., Cohen, M. L., Schooley, J. F., Hosler, W. R., and Pfeiffer, E. R. (1967). Superconducting transition temperatures of semiconducting srtio$_3$. *Phys. Rev.*, 163:380–390.

[65] Kresin, V. Z., Ovchinnikov, Y. N., and Wolf, S. A. (2006). *Phys. Rep.*, 431(231).

[66] L. Landau, E. L. (1984). *Electrodynamics of continuous media (second edition)*. Pergamon Press.

[67] Li, L., Richter, C., Mannhart, J., and Ashoori, R. C. (2011a). Coexistence of magnetic order and two-dimensional superconductivity at $LaAlO_3/SrTiO_3$ interfaces. *Nature Physics*, 7(10):762–766.

[68] Li, L., Richter, C., Paetel, S., Kopp, T., Mannhart, J., and Ashoori, R. C. (2011b). Very large capacitance enhancement in a two-dimensional electron system. *Science (New York, N.Y.)*, 332(6031):825–8.

[69] Li, Y.-H. and Teitel, S. (1989). Finite-size scaling study of the three-dimensional classical *XY* model. *Phys. Rev. B*, 40:9122–9125.

[70] Lowdin, P.-O. (1951). A Note on the Quantum-Mechanical Perturbation Theory. *The Journal of Chemical Physics*, 19(11):1396.

[71] Marković, N., Christiansen, C., Mack, A. M., Huber, W. H., and Goldman, A. M. (1999). Superconductor-insulator transition in two dimensions. *Phys. Rev. B*, 60:4320–4328.

[72] Meevasana, W., King, P. D. C., He, R. H., Hashimoto, M., Tamai, A., Songsiriritthigul, P., and Baumberger, F. (2011). Creation and control of a two-dimensional electron liquid at the bare SrTiO 3 surface. 10(February):114–118.

[73] Mehta, M. M., Dikin, D. a., Bark, C. W., Ryu, S., Folkman, C. M., Eom, C. B., and Chandrasekhar, V. (2012). Evidence for charge-vortex duality at the LaAlO3/SrTiO3 interface. *Nature communications*, 3:955.

[74] Muniz, R. A. and Martin, I. (2011). Method for detecting superconducting stripes in high-temperature superconductors based on nonlinear resistivity measurements. *Phys. Rev. Lett.*, 107:127001.

[75] Nakagawa, N., Hwang, H. Y., and Muller, D. a. (2006). Why some interfaces cannot be sharp. *Nature Materials*, 5(3):204–209.

[76] Neville, R. C. (1972). Permittivity of Strontium Titanate. *Journal of Applied Physics*, 43(5):2124.

[77] Ohtomo, a. and Hwang, H. Y. (2004). A high-mobility electron gas at the LaAlO3/SrTiO3 heterointerface. *Nature*, 427(6973):423–6.

[78] Ovchinnikov, Y. N., Wolf, S. A., and Kresin, V. Z. (2001). *Physical Review B*, 63(064524).

[79] Parendo, K. A., Tan, K. H. S. B., Bhattacharya, A., Eblen-Zayas, M., Staley, N. E., and Goldman, A. M. (2005). Electrostatic tuning of the superconductor-insulator transition in two dimensions. *Phys. Rev. Lett.*, 94:197004.

[80] Park, S. Y. and Millis, A. J. (2013). Charge density distribution and optical response of the LaAlO_{3}/SrTiO_{3} interface. *Physical Review B*, 87(20):205145.

[81] Pavlenko, N., Kopp, T., and Mannhart, J. (2013). Emerging magnetism and electronic phase separation at titanate interfaces. *Physical Review B*, 88(20):201104.

[82] Pentcheva, R. and Pickett, W. E. (2010). Electronic phenomena at complex oxide interfaces: insights from first principles. *Journal of Physics: Condensed Matter*, 22(4):043001.

[83] Popović, Z. S., Satpathy, S., and Martin, R. M. (2008). Origin of the two-dimensional electron gas carrier density at the laalo$_3$ on srtio$_3$ interface. *Phys. Rev. Lett.*, 101:256801.

[84] Rakhmilevitch, D., Neder, I., Shalom, M. B., Tsukernik, A., Karpovski, M., Dagan, Y., and Palevski, A. (2013). Anomalous response to gate voltage application in mesoscopic laalo$_3$/srtio$_3$ devices. *Phys. Rev. B*, 87:125409.

[85] Ram-Mohan, L. R. (2002). *Finite Element and Boundary Element Applications in Quantum Mechanics*. Oxford University Press.

[86] Ram-Mohan, L. R. (2004). The Schrödinger-Poisson self-consistency in layered quantum semiconductor structures. *Journal of Applied Physics*, 95(6):3081.

[87] Reyren, N., Thiel, S., Caviglia, a. D., Kourkoutis, L. F., Hammerl, G., Richter, C., Schneider, C. W., Kopp, T., a S Rüetschi, Jaccard, D., Gabay, M., Muller, D. a., Triscone, J.-M., and Mannhart, J. (2007). Superconducting interfaces between insulating oxides. *Science (New York, N.Y.)*, 317(5842):1196–9.

[88] Richter, C., Boschker, H., Dietsche, W., Fillis-Tsirakis, E., Jany, R., Loder, F., Kourkoutis, L. F., Muller, D. a., Kirtley, J. R., Schneider, C. W., and Mannhart, J. (2013). Interface superconductor with gap behaviour like a high-temperature superconductor. *Nature*, 502(7472):528–31.

[89] Ristic, Z., Capua, R. D., Luca, G. M. D., Chiarella, F., Ghiringhelli, G., Cezar, J. C., Brookes, N. B., Richter, C., Mannhart, J., and Salluzzo, M. (2011). Nanoscale modulation of the density of states at the conducting interface between laalo 3 and srtio 3 band insulators. *EPL (Europhysics Letters)*, 93(1):17004.

[90] Salluzzo, M., Cezar, J., Brookes, N., Bisogni, V., De Luca, G., Richter, C., Thiel, S., Mannhart, J., Huijben, M., Brinkman, a., Rijnders, G., and Ghiringhelli, G. (2009). Orbital Reconstruction and the Two-Dimensional Electron Gas at the LaAlO3/SrTiO3 Interface. *Physical Review Letters*, 102(16):166804.

[91] Santander-Syro, A. F., Copie, O., Kondo, T., Fortuna, F., Pailhès, S., Weht, R., Qiu, X. G., Bertran, F., Nicolaou, A., Taleb-Ibrahimi, A., Le Fèvre, P., Herranz, G., Bibes, M., Reyren, N., Apertet, Y., Lecoeur, P., Barthélémy, A., and Rozenberg, M. J. (2011). Two-dimensional electron gas with universal subbands at the surface of SrTiO(3). *Nature*, 469(7329):189–93.

[92] Scopigno, N., Bucheli, D., Caprara, S., Biscaras, J., Bergeal, N., Lesueur, J., and Grilli, M. (2016). Phase separation from electron confinement at oxide interfaces. *Phys. Rev. Lett.*, 116:026804.

[93] Shi, X., Lin, P. V., and Sasagawa, T. (2014). Two-stage magnetic-field-tuned superconductor– insulator transition in underdoped $La_{2-x}Sr_xCuO_4$. (May):1–7.

[94] Siemons, W., Koster, G., Yamamoto, H., Harrison, W. A., Lucovsky, G., Geballe, T. H., Blank, D. H. A., and Beasley, M. R. (2007). Origin of charge density at laalo$_3$ on srtio$_3$ heterointerfaces: Possibility of intrinsic doping. *Phys. Rev. Lett.*, 98:196802.

[95] Sondhi, S. L., Girvin, S. M., Carini, J. P., and Shahar, D. (1997). RMP Colloquia. *Reviews of Modern Physics*, 69(1):315–333.

[96] Spivak, B., Oreto, P., and Kivelson, S. A. (2008). Theory of quantum metal to superconductor transitions in highly conducting systems. *Phys. Rev. B*, 77:214523.

[97] Steffen, K., Loder, F., and Kopp, T. (2015). Spin-orbit controlled quantum capacitance of a polar heterostructure. *Physical Review B*, 91(7):075415.

[98] Stornaiuolo, D., Gariglio, S., Couto, N. J. G., Fête, A., Caviglia, A. D., Seyfarth, G., Jaccard, D., Morpurgo, A. F., and Triscone, J.-M. (2012). In-plane electronic confinement in superconducting $laalo_3/srtio_3$ nanostructures. *Applied Physics Letters*, 101(22).

[99] Suli (2000). Finite Element Methods for Partial Differential Equations. *University of Oxford*.

[100] Sulpizio, J. a., Ilani, S., Irvin, P., and Levy, J. (2014). Nanoscale Phenomena in Oxide Heterostructures. *Annual Review of Materials Research*, 44(1):117–149.

[101] Wilson, K. G. and Fisher, M. E. (1972). Critical exponents in 3.99 dimensions. *Phys. Rev. Lett.*, 28:240–243.

[102] Winkler, R. (2003). *Spin-Orbit Coupling Effects in Two-Dimensional Electron and Hole Systems*, volume 191 of *Springer Tracts in Modern Physics*. Springer Berlin Heidelberg, Berlin, Heidelberg.

[103] Yazdani, A. and Kapitulnik, A. (1995). Superconducting-insulating transition in two-dimensional a-moge thin films. *Phys. Rev. Lett.*, 74:3037–3040.

[104] Yoshimatsu, K., Yasuhara, R., Kumigashira, H., and Oshima, M. (2008). Origin of Metallic States at the Heterointerface between the Band Insulators LaAlO3 and SrTiO3. *Physical Review Letters*, 101(2):026802.

[105] Yu, L. and Zunger, A. (2014). A polarity-induced defect mechanism for conductivity and magnetism at polar-nonpolar oxide interfaces. *Nature communications*, 5:5118.

[106] Zhong, Z., Tóth, A., and Held, K. (2013). Theory of spin-orbit coupling at LaAlO 3 /SrTiO 3 interfaces and SrTiO 3 surfaces. *Physical Review B*, 87(16):161102.

Appendix A

Effective Medium Theory

A.1 Derivation of the Effective Medium Theory

We here derive the Effective Medium Theory (EMT) expressions of the resistivity of an inhomogeneous binary medium resulting from the mixture of two phases, following the method introduced by Landauer-Bruggeman.

The effective medium approximation enables the description of a macroscopically inhomogeneous medium, such as an emulsion or a powder mixture, through the calculation of its conductivity, its dielectric function or other quantities that vary in space. If the substance is made of finely dispersed particles , it is often reasonable to consider only quantities averaged on a certain small, but still macroscopic, volume. In the following, we will use the effective medium theory to derive an expression for the dielectric function of a binary mixture of spherical grains with dielectric constant ε_A and ε_B, but the same equations remain valid for any effective coefficient connecting a curl-free driving field to a divergence-free current density. If an external constant electric field $\mathbf{E_0}$ is applied to the mixture, the local field $\mathbf{E}$ will depend on the position of all particles and in general it will not be constant in space.

The mean field approach considers a single grain embedded in an effective medium, whose dielectric constant is determined by the condition that the average field in the medium has to be equal to the external field $\mathbf{E_0}$.

The electric field $\mathbf{E}$ inside a nonconducting sphere of dielectric constant ε_i, embedded in an homogeneous medium of permittivity ε_e is [66]

$$\mathbf{E_i} = \frac{D\varepsilon_e}{(D-1)\varepsilon_i + \varepsilon_e}\mathbf{E_0} \tag{A.1}$$

where D is the dimension of the space (for a three dimensional sphere, $D = 3$). If w_A is the fraction of particle of type A and w_B that of particles B, the average field in the medium is

$$\bar{\mathbf{E}} = \frac{N_A}{N}\mathbf{E_A} + \frac{N_B}{N}\mathbf{E_B} = w_A\mathbf{E_A} + w_b\mathbf{E_B} \tag{A.2}$$

which has to be equated to the external field $\mathbf{E_0}$

$$w_A \frac{D\varepsilon_{EMT}}{(D-1)\varepsilon_A + \varepsilon_{EMT}}\mathbf{E_0} + w_b \frac{D\varepsilon_{EMT}}{(D-1)\varepsilon_B + \varepsilon_{EMT}}\mathbf{E_0} = \mathbf{E_0}. \tag{A.3}$$

This equation can be easily generalized for an arbitrary number of different particles as

$$\sum_i w_i \frac{D\varepsilon_{EMT}}{(D-1)\varepsilon_i + \varepsilon_{EMT}}\mathbf{E_0} = \mathbf{E_0}. \tag{A.4}$$

Using the relation $\sum_i w_i \frac{(D-1)\varepsilon_i + \varepsilon_{EMT}}{(D-1)\varepsilon_i + \varepsilon_{EMT}} = 1$ the equation is rewritten as

$$\sum_i \frac{\varepsilon_{EMT} - \varepsilon_i}{(D-1)\varepsilon_{EMT} + \varepsilon_i}\mathbf{E_0} = \mathbf{E_0}. \tag{A.5}$$

A.2 Derivation of EMT formulas for Hall conductivity

Here we derive the Effective Medium Theory (EMT) expressions of the Hall conductance for an inhomogeneous binary medium resulting from the mixture of two phases, following the method based on rotation transformations (see Ref.[3] for a detailed description of this method). We first define the elements of the conductivity tensor for each of the two phases in a magnetic field of amplitude B,

$$\begin{aligned}
\sigma_{xx}^{(1)}(B) &= \frac{\sigma^{(1)}}{1+\beta_1(B)^2}, \\
\sigma_{xx}^{(2)}(B) &= \frac{\sigma^{(1)}}{1+\beta_1(B)^2} + \frac{\sigma^{(2)}}{1+\beta_2(B)^2},
\end{aligned}$$

$$\begin{aligned}
\sigma_{xy}^{(1)}(B) &= \frac{\sigma^{(1)}\beta_1(B)}{1+\beta_1(B)^2}, \\
\sigma_{xy}^{(2)}(B) &= \frac{\sigma^{(1)}\beta_1(B)}{1+\beta_1(B)^2} + \frac{\sigma^{(2)}\beta_2(B)}{1+\beta_2(B)^2},
\end{aligned}$$

where $\beta_i(B) \equiv \mu_i B/c$ and $\sigma^{(i)} = en_i\mu_i$ (μ_i is the electron mobility in the i-th phase). Notice that both electrons in bands 1 and 2 contribute to the conductivities in the phase 2. According to the analysis of chapter 2 we assume that $w \equiv \frac{1}{2} - \varepsilon$ is the fraction of the more conducting phase 2. ε is the excess over the percolation threshold and in two dimensions changes sign when the minority phase ($w < \frac{1}{2}$, $\varepsilon > 0$) crosses the percolation threshold and becomes the majority phase ($w > \frac{1}{2}$, $\varepsilon < 0$).

First of all one defines the diagonal elements of the EMT conductivity tensor

$$\begin{aligned}\sigma_{xx}^{EMT}(B,\varepsilon) &= \varepsilon\left(\sigma_{xx}^{(2)}(B) - \sigma_{xx}^{(1)}(B)\right) \\ &+ \left[\varepsilon^2\left(\sigma_{xx}^{(1)}(B) - \sigma_{xx}^{(2)}(B)\right)^2 + \sigma_{xx}^{(1)}(B)\sigma_{xx}^{(2)}(B)\right]^{\frac{1}{2}}.\end{aligned} \tag{A.6}$$

Then, exploiting duality relations that connect the various elements of the conductivity tensor when the minority and majority phases are interchanged (see Ref.[3]), one obtains the EMT expression for the off-diagonal elements of the conductivity tensor

$$\begin{aligned}\sigma_{xy}^{EMT}(B,\varepsilon) = \Bigg[&\frac{\left(\sigma_{xx}^{EMT}(B,\varepsilon) + \sigma_{xx}^{EMT}(B,-\varepsilon)\right)\left(\sigma_{xx}^{(1)}(B)\sigma_{xy}^{(2)}(B) + \sigma_{xy}^{(1)}(B)\sigma_{xx}^{(2)}(B)\right)}{\sigma_{xx}^{(1)}(B) + \sigma_{xx}^{(2)}(B)} \\ &- \frac{\left(\sigma_{xx}^{EMT}(B,\varepsilon) - \sigma_{xx}^{EMT}(B,-\varepsilon)\right)\left(\sigma_{xx}^{(1)}(B)\sigma_{xy}^{(2)}(B) - \sigma_{xy}^{(1)}(B)\sigma_{xx}^{(2)}(B)\right)}{\sigma_{xx}^{(1)}(B) - \sigma_{xx}^{(2)}(B)}\Bigg]\frac{1}{2\sigma_{xx}^{EMT}(B,-\varepsilon)}\end{aligned}$$

From this the expression of the Hall resistance can be derived

$$R_H^{EMT}(B,\varepsilon) = \frac{\sigma_{xy}^{EMT}(B,\varepsilon)}{\sigma_{xy}^{EMT}(B,\varepsilon)^2 + \sigma_{xx}^{EMT}(B,\varepsilon)^2}. \tag{A.7}$$

Appendix B

Finite Size Scaling calculation

The resistance is rewritten as $R(\delta,t) = R_c F(|\delta|t)$ with t an unknown parameter that depends only on the temperature T, and $\delta = (V_G - V_{G_c})$ is the distance to the critical point. The parameter t is then found at each temperature T by optimizing the collapse around the critical point between the curve $R(\delta,t(T))$ at the temperature T and the curve $R(\delta,t(T_0))$ at the lowest temperature considered T_0, with $t(T_0) = 1$. The dependence of t with the temperature should be a power law of the form $t = (T/T_0)^{-1/z\nu}$ in order to have a physical sense, thus giving the critical exponent product $z\nu$. The interest of this procedure is to perform the scaling without knowing the critical exponents beforehand.

Appendix C

The Finite Elements Method

In our work we used the Finite Elements Method (FEM) to solve the Scrödinger boundary value problem. Without claiming to be complete, we resume briefly the ideas behind the method, leaving to the appropriate literature a more detailed discussion. In what follows, we refers to Ram-Mohan [85, 86] and Süli [99].

C.1 Weak solution and boundary value problems

The first step in constructing a finite element method for a boundary value problem of the type E.1, together with the associated boundary conditions E.4, is to convert the problem into its weak formulation[1]. If V is the solution space (e.g. $H_0^1(\Omega)^2$ for the homogeneous Dirichlet boundary value problem), $a(\cdot,\cdot)$ is a bilinear functional on $V \times V$ and $l(\cdot)$ is a linear functional on V, then a weak formulation consist in finding $u \in V$ such that $a(u,v) = l(v) \quad \forall v \in V$.

Once we have rewritten the equation in an integral formulation, we proceed replacing the space V by a finite-dimensional subspace $V_h \subset V$ which consist, for example, of all the continuous piecewise polynomial functions of a fixed degree associated with a subdivision of the computational domain. In this way the problem related to our equation becomes to find $u_h \in V_h$ such that $a(u_h, v_h) = l(v_h) \quad \forall v_h \in V_h$. In practice, we can imagine to chose a set V_h such that

$$dim\ \ V_h = N(h) \quad V_h = span\{\phi_1, \cdots, \phi_{N(h)}\}$$

---

[1] For a definition of weak formulation, Sobolev spaces and related topics of functional analysis see [Brezis].

[2] $H_0^1(\Omega)$, a Sobolev space, is defined as

$$H_0^1(\Omega) = \left\{ u \in L_2(\Omega) : \frac{\partial u}{\partial x_i} \in L_2(\Omega), \quad i = 1, \cdots, n, \quad u = 0 \ \ on \ \ \partial\Omega \right\}$$

where the $\{\phi_i\}$ is a basis of functions that have a small support[3] We can expand the solution of the approximated problem on this basis as

$$u_h(x) = \sum_{i=1}^{N(h)} U_i \phi_i(x) \tag{C.1}$$

where the coefficients $U_i \in \mathbb{R}$ are to be determined so that

$$\sum_{i=1}^{N(h)} U_i a(\phi_i, \phi_j) = l(\phi_j) \quad j = 1, \cdots, N(h). \tag{C.2}$$

This is a system of linear equations for the vector $U = (U_1, \cdots, U_{N(h)})$, with the matrix of the system $A = (a(\phi_i, \phi_j))$, of size $N(h) \times N(h)$, that exhibits the (computationally) nice property to be a sparse matrix[4]. Once the linear equations are solved, the coefficients U_i can be put in C.1 providing the required approximation to u. Usually the functions ϕ_i are compactly supported on sub-domains of the entire domain Ω; these sub-domains are called *elements*, from which the name *Finite Element Method.*

Among all kinds of boundary value problems, the self-adjoint one is the most important for our purposes because it is closely related to a principle of stationary action. As an example, we will illustrate in the following how it is possible to restate a (self-adjoint) boundary value problem as a variational one when we are dealing with an elliptic operator, leaving the solution of the Schroedinger equation to C.2.1.

C.2 The self-adjoint elliptic problem and the principle of stationary action

Let us consider an the boundary value problem

$$-\sum_{i,j=1}^{n} \frac{\partial}{\partial x_j}\left(a_{ij}(x)\frac{\partial u}{\partial x_i}\right) + \sum_{i=1}^{n} b_i(x)\frac{\partial u}{\partial x_i} + c(x)u = f(x) \quad x \in \Omega, \tag{C.3}$$

$$u = 0 \quad on \ \partial\Omega \tag{C.4}$$

where Ω is a bounded open set in $\mathbb{R}^n$, $a_{ij} \in L_\infty(\Omega)$, $i, j = 1, \cdots, n$; $b_i \in W^{1,\infty}(\Omega)$, $c \in L_\infty(\Omega)$, $f \in L_2(\Omega)$.

The ellipticity condition reads

---

[3] As we will see below, the ϕ_i are usually chosen compactly supported.

[4] Inasmuch the ϕ_i has small support, $a(\phi_i, \phi_j) = 0$ for most pairs of i and j.

$$\exists \tilde{c} : \sum_{i,j=1}^{n} a_{ij}(x)\xi_i\xi_j \geq \tilde{c} \sum_{i,j=1}^{n} \xi_i^2 \quad \forall x \in \bar{\Omega}. \tag{C.5}$$

while the boundary value problem is self-adjoint if

$$a_{ij}(x) = a_{ji}(x), \quad i, j = 1, \cdots, n \quad x \in \bar{\Omega} \tag{C.6}$$

$$b_i(x) \equiv 0, \quad i, j = 1, \cdots, n \quad x \in \bar{\Omega} \tag{C.7}$$

The self-adjointness condition let us to restate the problem as

$$-\sum_{i,j=1}^{n} \frac{\partial}{\partial x_j}\left(a_{ij}(x)\frac{\partial u}{\partial x_i}\right) + c(x)u = f(x) \quad x \in \Omega, \tag{C.8}$$

$$u = 0 \quad on \;\; \partial\Omega \tag{C.9}$$

and the weak formulation of this problem, taking into account C.7, consist in finding $u \in H_0^1(\Omega)$ such that

$$a(u,v) = l(v) \quad \forall v \in H_0^1(\Omega), \tag{C.10}$$

where the bilinear functional $a(\cdot,\cdot)$ is symmetric

$$a(u,v) = a(v,u) \quad \forall u, v \in H_0^1(\Omega)$$

and it is defined by

$$a(u,v) = \sum_{i,j=1}^{n} \int_{\Omega} a_{ij} \frac{\partial u}{\partial x_i}\frac{\partial v}{\partial x_j} dx + \int_{\Omega} c(x)uv dx \tag{C.11}$$

while the linear functional $l(\cdot)$ is

$$l(v) = \int_{\Omega} f(x)v(x)dx. \tag{C.12}$$

The theory of elliptic partial differential equations states that, for a self-adjoint problem, the condition $c(x) \geq 0, \quad x \in \bar{\Omega}$, is enough to ensure that the weak problem has a unique solution in $H_0^1(\Omega)$.

We want to show that the weak problem we have just stated is equivalent to a minimization problem. Let us define the quadratic functional $J : H_0^1(\Omega) \to \mathbb{R}$ by

$$J(v) = \frac{1}{2}a(v,v) - l(v), \quad v \in H_0^1(\Omega). \tag{C.13}$$

The following two lemmas, whose demonstration we omit, express the equivalence of the weak formulation

find $u \in H_0^1(\Omega)$ such that $a(u,v) = l(v) \quad \forall v \in H_0^1(\Omega)$

and the minimization problem

find $u \in H_0^1(\Omega)$ such that $J(u) \leq J(v) \quad \forall v \in H_0^1(\Omega)$.

Lemma 1 *Let u be the (unique) weak solution to C.10 in* $H_0^1(\Omega)$ *and suppose that* $a(\cdot,\cdot)$ *is a symmetric bilinear functional on* $H_0^1(\Omega)$*; then u is the unique minimizer of* $J(\cdot)$ *over* $H_0^1(\Omega)$.

Lemma 2 *Suppose that* $u \in H_0^1(\Omega)$ *minimizes* $J(\cdot)$ *over* $H_0^1(\Omega)$*; than u is the (unique) solution of C.10. The problem C.9 is called the Euler-Lagrange equation for the minimization problem.*

These arguments can be used to give a variational formulation of the self-adjoint problem whether we intend to use the finite elements approximation $u_h \in V_h$ instead of $u \in V$. It can be shown that the approximated solution shares the same energy minimization possessed by the weak solution $u \in H_0^1(\Omega)$ so that

$$J(u_h) = \min_{v_h \in V_h} J(v_h). \tag{C.14}$$

In general $J(u) \leq J(u_h)$.

In the case which is relevant to the present work, the Schroedinger equation

$$-\frac{\hbar^2}{2m}\nabla^2\psi(\mathbf{r}) + V(\mathbf{r})\psi(\mathbf{r}) = E\psi(\mathbf{r}) \tag{C.15}$$

is obtained from the functional $\mathscr{A}(\psi)$, that is nothing more than the action integral

$$\mathscr{A} = \int_{t_a}^{t_b} L(q,\dot{q},t)dt, \tag{C.16}$$

where L is the Lagrangian for the Schroedinger equation and

$$\mathscr{A} = \int dr^3 \left[\frac{\hbar^2}{2m}\nabla\psi^*(\mathbf{r})\cdot\nabla\psi(\mathbf{r}) + \psi^*(\mathbf{r})(V(\mathbf{r}) - E)\psi(\mathbf{r})\right]. \tag{C.17}$$

Here ψ^* and ψ can be considered as two independent fields and the Schroedinger equation results from varying $\mathscr{A}$ with respect to $\psi^*(\mathbf{r})$, while the the canonical equal time commutation rules can be found by varying the end points[5].

C.2.1 A finite element method for the 1D.Schrödinger equation

Suppose we want to solve equation C.15 in a certain interval $[x_{min}, x_{max}]$ with certain BCs. The application of the finite element method starts dividing the region into smaller regions called *elements*, so that the action integral C.17 is rewritten as

$$\mathscr{A} = \sum_{(iel)}^{nelem} \mathscr{A}^{(iel)}. \tag{C.18}$$

The approximated problem is found replacing the exact solution $\psi(x)$ with the approximated solution

$$\tilde{\psi}(x) = \sum_i \psi_i N_i(x)$$

where the functions $N_i(x)$ are the interpolation polynomials of $\psi(x)$ and are chosen in such a way their support corresponds to a certain element and the coefficients ψ_i are the values of the solution at special points within the elements called *nodes*. To be more clear, we construct the approximating set V_n taking n^{iel}_{polyn} interpolation polynomials[6] for each element *iel*, where they are compactly supported.

In the i_{el}th element the wave function is given by

$$\tilde{\psi}(x) = \sum_j^{n^{iel}_{polyn}} \psi^{iel}_j N^{iel}_j$$

and the approximated problem is solved when all the ψ^{iel}_j are found for each element.

---

[5] In his initial paper Schroedinger showed equation C.15 could be obtained finding the extremum of the integral

$$\mathscr{I} = \int dr^3 \left[\frac{\hbar^2}{2m} \nabla \psi^*(\mathbf{r}) \cdot \nabla \psi(\mathbf{r}) + \psi^*(\mathbf{r}) V(\mathbf{r}) \psi(\mathbf{r}) \right]$$

with respect of variation of $\psi^*(\mathbf{r})$ and subject to the subsidiary condition

$$\int dr^3 \psi^*(\mathbf{r}) \psi(\mathbf{r}) = 1$$

that is nothing more than the well-known normalizability condition. It ensures that the probability of finding one particle in the physical region is unity. The energy parameter E in equation C.15 has the role of a Lagrange multiplier that is used to incorporate the condition 5 directly in the integral $\mathscr{I}$.

[6] The number of polynomials n^{iel}_{polyn} is usually taken to be independent from the element *iel*

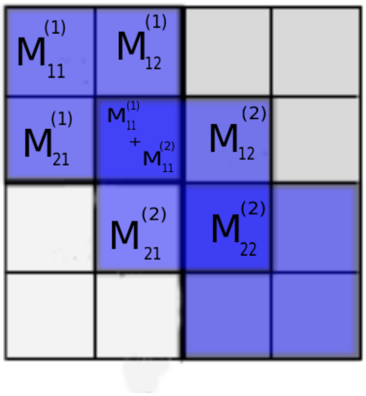

Fig. C.1 The global matrix constructed from local element matrices using overlap of the matrices is shown for a 1D problem treated with linear interpolation over three elements [85].

Since the spatial dependence in the action integral is carried only by the interpolation polynomials, which are compactly supported, it can be integrated away independently in each element and the action can be rewritten as C.18, where

$$\mathscr{A}^{(iel)} = \sum_{i,j}^{n_{polyn}} \psi_i^* \left[\int dx N_i(x) \mathscr{L} N_j(x) \right] \psi_j = \sum_{i,l}^{n_{polyn}} \psi_i^* \mathscr{M}_{ij}^{iel} \psi_j$$

and $\mathscr{L}$ is the Lagrangian density operator. The total action can be put in a matrix form through a global matrix $\mathscr{M}$, that is built taking into account the continuity conditions at the nodes between the elements[7][8]. For the case of a linear interpolation, $\mathscr{M}$ is depicted in figure C.1.

Once $\mathscr{M}$ has been constructed, a more fruitful approach to the minimization of the action integral is to switch from a description element-by-element to a nodal point of view, where the interpolation polynomials are referred to the nodes rather than to elements. It can be done renaming conveniently the polynomials and being careful about the overlapping conditions between adjacent nodes. Therefore the action integral is rewritten as

$$\mathscr{A} = \sum_{\alpha,\beta}^{n_{glob}} \psi_\alpha^* \mathscr{M}_{\alpha\beta} \psi_\beta$$

and the *principle of least action* is

---

[7] For example, if n_{nodes} is the number of nodes for each element, we impose $\psi_{n_{nodes}}^{iel} = \psi_1^{iel+1}$

[8] The continuity condition at the nodes resides in the continuity of the wavefunction. Since for many physical situation also the first derivative of the wavefunction is continuous, the polynomials N_i are chosen so that they can also interpolate ψ'

$$\frac{\delta \mathscr{A}}{\delta \psi_\alpha^*} = \sum_\beta \mathscr{M}_{\alpha\beta} \psi_\beta = 0.$$

The set of linear equations C.2.1 cannot be solved trivially because of the presence of the undetermined Lagrange multiplier E, as explained in C.2. It means we have to go further and decompose the problem, isolating the terms that are multiplied by E. If we define the matrices $\mathscr{H}$ (terms of $\mathscr{M}$ that do not depend on E) and $\mathscr{U}$ (terms of $\mathscr{M}$ that do depend on E), the principle of stationary action takes the form

$$\delta \mathscr{A} = 0 = \sum_{\alpha\beta} \delta \psi_\alpha^* \left(\mathscr{H}_{\alpha\beta} - E \mathscr{U}_{\alpha\beta} \right) \psi_\beta = 0$$

and the generalized eigenvalue equation

$$\sum_\beta \left[\mathscr{H}_{\alpha\beta} \psi_\beta - E \mathscr{U}_{\alpha\beta} \psi_\beta \right] = 0.$$

Finally we can impose the boundary conditions setting to the appropriate values the entries in the matrices $\mathscr{H}$ and $\mathscr{U}$. In our case, since we require $\psi(x_{min}) = \psi(x_{max}) = 0$, the initial and the final nodal values ψ_1, $\psi_{nelem+1}$, ψ_1^*, $\psi_{nelem+1}^*$ have to be zero; this is achieved setting to zero the entries in the first and last columns, and in the first and last rows of $\mathscr{H}$ and $\mathscr{U}$.

The equation C.2.1 is then solved numerically using an appropriate computational method[9].

---

[9] E.g. those founds in LAPACK/EISPACK libraries

Appendix D

Bands Structure of 2D systems: $\mathbf{k} \cdot \mathbf{p}$ Theory and Envelope Function Approximation

The $\mathbf{k} \cdot \mathbf{p}$ method enables the calculation of the band structure of a crystal, with arbitrary precision, in the vicinity of a given point $\mathbf{k}_0$ of the reciprocal space. When used together with symmetry arguments, it show that band structure in a small region of $\mathbf{k}$ space depends only on few parameters. Once these parameters are known (they can be extracted from experiments) for some value k_0, it is possible to use $\mathbf{k} \cdot \mathbf{p}$ theory to determine the band structure at least for $\mathbf{k}$ close to $\mathbf{k}_0$.

However, while $\mathbf{k} \cdot \mathbf{p}$ theory deals with bulk semiconductors, where the infinite lattice allows the use of $\mathbf{k}$ as a good quantum number and the Bloch theorem applies, heterostructures are not periodic and usually their Schrödinger equation contains potential with very different scaling behavior. It turns out that $\mathbf{k} \cdot \mathbf{p}$ theory can be generalized in the so called Envelop Function Approximation (EFA).

The Envelop Function Approximation is a well established method to investigate the properties of a layered heterostructure. It can be used to describe the band structure of a crystal in the presence of external electric and magnetic fields or strain. In these conditions, EFA gives a comprehensive description of electron and hole states, while the details of the crystal potential are included in terms of bulk band structure parameters. In the following section we will present a small resume of both $\mathbf{k} \cdot \mathbf{p}$ theory and EFA[1].

---

[1] We mainly follow [102],[48].

D.1 k · p Method and Effective Mass Approximation

The Schrödinger equation for the Block functions $e^{i\vec{k}\cdot\vec{r}}u_{\nu\vec{k}}(\vec{r}) \equiv e^{i\vec{k}\cdot\vec{r}}\left\langle\vec{r}|\nu\vec{k}\right\rangle$ in the microscopic lattice-periodic crystal potential $V_0(\vec{r})$ is

$$\left[\frac{p^2}{2m_0}+V_0(\vec{r})\right]e^{i\vec{k}\cdot\vec{r}}u_{\nu\vec{k}}(\vec{r}) = E_{\nu\vec{k}}e^{i\vec{k}\cdot\vec{r}}u_{\nu\vec{k}}(\vec{r}) \tag{D.1}$$

where m_0 is the bare electron mass and ν is the band index. The exponential factor can be eliminated and D.1 is rewritten as

$$\left[\frac{p^2}{2m_0}+V_0+\frac{\hbar^2k^2}{2m_0}+\frac{\hbar}{m_0}\vec{k}\vec{p}\right]\left|\nu\vec{k}\right\rangle = E_{\nu\vec{k}}\left|\nu\vec{k}\right\rangle \tag{D.2}$$

The spin-orbit interaction[2] can be included using a common quantum number n for the orbital and spin degrees of freedom (that are no longer separately conserved), associated to the irreducible representation of the double group. In this case the Schrödinger equation reads

$$\left[\frac{p^2}{2m_0}+V_0+\frac{\hbar^2k^2}{2m_0}+\frac{\hbar}{m_0}\vec{k}\vec{\pi}+\frac{\hbar}{4m_0^2c^2}\vec{\sigma}\vec{p}\times(\nabla V_0)\right]\left|n\vec{k}\right\rangle = E_{n\vec{k}}\left|n\vec{k}\right\rangle \tag{D.4}$$

where $\vec{\pi}=\vec{p}+\frac{\hbar}{4m_0c^2}\vec{\sigma}\times(\nabla V_0)$ and $\vec{\sigma}=(\sigma_x,\sigma_y,\sigma_z)$ is the vector of Pauli spin matrices. Let us suppose we want to describe the band structure in a neighborhood of the wave vector $\vec{k}_0$, for example $\vec{k}_0=0$.

If we define the vectors $|\nu\sigma\rangle = |\nu\mathbf{0}\rangle\otimes|\sigma\rangle$, where $\sigma=\uparrow,\downarrow$, we can use both $\left\{\left|n\vec{k}\right\rangle\right\}$ and $\left\{\left|\nu\vec{k}\right\rangle\right\}$ as a complete and orthonormal basis for D.2-D.4. Moreover, we can perform the expansion

$$\left|n\vec{k}\right\rangle = \sum_{\nu'\sigma'}c_{n\nu'\sigma'}(\vec{k})\left|\nu'\sigma'\right\rangle. \tag{D.5}$$

This expansion is useful since we want to use a perturbative approach to treat the SO interaction. Multiplying D.4 by $\langle\nu\sigma|$ from the left (the integration is performed over a unit cell) we obtain an algebraic eigenvalue problems for $E_n(\vec{k})$:

---

[2] In the **k** · **p** and EFA methods the spin-orbit enters solely in terms of matrix elements of the Pauli term

$$H_{SO} = -\frac{\hbar}{4m_0^2c^2}\vec{\sigma}\vec{p}\times(\nabla V_0) \tag{D.3}$$

where m_0 and c are respectively the bare electron mass and the speed of light.

$$\sum_{\nu'\sigma'}\left\{\left[E_{\nu'}(\vec{0})+\frac{\hbar^2k^2}{2m_0}\right]\delta_{\nu\nu'}\delta_{\sigma\sigma'}+\frac{\hbar}{m_0}\vec{k}\vec{\mathscr{P}}_{\nu\nu'\sigma\sigma'}+\Delta_{\nu\nu'\sigma\sigma'}\right\}c_{n\nu'\sigma'}(\vec{k})=E_n(\vec{k})c_{n\nu\sigma}(\vec{k}) \tag{D.6}$$

where

$$\vec{\mathscr{P}}_{\nu\nu'\sigma\sigma'} = \langle\nu\sigma|\vec{\pi}\,|\nu'\sigma'\rangle = \frac{(2\pi)^3}{V_{cell}}\langle\sigma|\int_{V_{cell}} d\vec{r}u^*_{\nu0}(\vec{r})\vec{\pi}u_{\nu'0}(\vec{r})\,|\sigma'\rangle \tag{D.7}$$

$$\Delta_{\nu\nu'\sigma\sigma'} = \frac{\hbar}{4m_0^2c^2}\langle\nu\sigma|\,[\vec{p}\vec{\sigma}\times(\nabla V_0)]\,|\nu'\sigma'\rangle \tag{D.8}$$

In D.7 we can often neglect the SO coupling and use the approximations $\vec{\pi}=\vec{p}$, $\vec{\mathscr{P}}_{\nu\nu'\sigma\sigma'}=\delta_{\sigma\sigma'}\vec{\mathscr{P}}_{\nu\nu'}$. We also note that in D.6 the mixing of different bands $\left|\nu\vec{0}\right\rangle$ is more relevant between closer band edges and large values of $\vec{k}$. Usually the presence of the term $\Delta_{\nu\nu'\sigma\sigma'}$ is able to remove the degeneration of the energy levels $E_{\nu0}$ even at $\vec{k}=0$. Another relevant point to discuss is the dimensionality of the eigenvalue problem related to the **k**·**p** model: the set of equations D.6 is not finite dimensional, but since in many application we are interested only in a small number of adjacent bands we can consider a finite set of closer band edges and treat the contribution of the remote bands by means of the Löwdin perturbation theory [70] with the off-diagonal terms $\hbar/m_0\vec{k}\vec{\mathscr{P}}_{\nu\nu'\sigma\sigma'}$ taken as small perturbations. In this way the resulting Hamiltonian is finite-dimensional and contains extra terms of higher order in $\vec{k}$.

For example, a diagonalization of the D.6 using second order perturbation theory[3] gives, neglecting spin:

$$E_\nu(\vec{k})=E_\nu(\vec{0})+\frac{\hbar^2}{2}\sum_{\alpha\beta}k_\alpha(m^*)^{-1}_{\alpha\beta}k_\beta, \tag{D.9}$$

where

$$\left(\frac{m_0}{m^*_\nu}\right)_{\alpha\beta}=\delta_{\alpha\beta}+\frac{2}{m_0}\sum_{\nu'\neq\nu}\frac{(\mathscr{P}_{\nu\nu'})_\alpha(\mathscr{P}_{\nu'\nu})_\beta+(\mathscr{P}_{\nu\nu'})_\beta(\mathscr{P}_{\nu'\nu})_\alpha}{E_\nu(\vec{0})-E_{\nu'}(\vec{0})} \tag{D.10}$$

defines the *effective mass tensor* m^*.

Assuming an isotropic, parabolic band, the effective-mass Hamiltonian reads

---

[3] We can use both the Löwdin theory or the classical nondegenerate perturbation theory. In the latter case, the hypothesis of a nondegenerate band has to be made.

$$E_\nu(\vec{k}) = E_\nu(\vec{0}) + \frac{\hbar^2 k^2}{2m_\nu^*}, \tag{D.11}$$

where

$$\frac{m_0}{m_\nu^*} = 1 + \frac{2}{m_0}\sum_{\nu'} \frac{\mathscr{P}^2_{\nu\nu'}}{E_\nu(\vec{0}) - E_{\nu'}(\vec{0})}. \tag{D.12}$$

D.2 Envelope Function Approximation

Thanks to the possibility to reach any desirable precision simply accounting for a larger number of bands, the **k** · **p** method is very powerful. Nevertheless, if we want to describe electrons and holes in the presence of external electric and magnetic fields that vary slowly on the length scale of the lattice constant, we have to generalize it introducing another parametrization for the set of eigenfunctions, more suitable than the Block form $e^{i\vec{k}\cdot\vec{r}}u_{\nu\vec{k}}(\vec{r})$. This is done in the Envelope Function Approximation (EFA) by means of the expansion

$$\Psi(\vec{r}) = \sum_{\nu'\sigma'} \psi_{\nu'\sigma'}(\vec{r})\, u_{\nu'\vec{0}}(\vec{r}) \left|\sigma'\right\rangle \tag{D.13}$$

where the position-dependent coefficients $\psi_{\nu\sigma}$ are the *envelope functions* and $\Psi(\vec{r})$ is the solution of the EFA Schroedinger equation

$$\left[\frac{(-i\hbar\nabla + e\vec{A})^2}{2m_0} + V_0(\vec{r}) + \frac{\hbar}{4m_0^2c^2}(-i\hbar\nabla + e\vec{A})\cdot\vec{\sigma}\times(\nabla V_0) + V(\vec{r}) + \frac{g_0}{2}\mu_B\vec{\sigma}\vec{B}\right]\Psi(\vec{r}) = E\Psi(\vec{r}). \tag{D.14}$$

In these expressions V_0 is the crystal potential, $V(\vec{r})$ an additional slowly varying potential[4] and $\vec{A}(\vec{r})$ is the vector potential associated to the magnetic field $\vec{B} = \nabla \times \vec{A}$, while $\mu_b = e\hbar/2m_0$ is the Bohr magneton and g_0 is the gyromagnetic factor for a free electron.

The multiband EFA Hamiltonian is obtained by an analogous procedure as in the **k**·**p** method: we multiply D.14 from the left by $\langle \nu\sigma|$, performing the integration on a unit cell and taking in account that $V(\vec{r})$ and $\vec{A}(\vec{r})$ are constant on the scale of the lattice parameter.

The resulting Hamiltonian is

---

[4] Actually, there are more elaborate derivations [20],[44] of the EFA equation in which the hypothesis of a slowly varying potential is not needed, such as for discontinuous band parameters.

$$\sum_{\nu'\sigma'} \left\{ \left[E_{\nu'}(\vec{0}) + \frac{(-i\hbar\nabla + e\vec{A})^2}{2m_0} + V(\vec{r}) \right] \delta_{\nu\nu'} \delta_{\sigma\sigma'} \right. \tag{D.15}$$

$$+ \frac{1}{m_0}(-i\hbar\nabla + e\vec{A}) \cdot \mathscr{P}_{\nu\nu'\sigma\sigma'} \tag{D.16}$$

$$\left. + \Delta_{\nu\nu'\sigma\sigma'} + \frac{g_0}{2}\mu_B \vec{\sigma}\vec{B}\delta_{\nu\nu'} \right\} \psi_{\nu'\sigma'}(\vec{r}) = E\psi_{\nu\sigma}(\vec{r}). \tag{D.17}$$

Here we have again an infinite-dimensional eigenvalue problem. It can be reduced to a finite one if we consider only closer band edges, using Löwdin partitioning to treat the other bands. As for the **k** · **p** model, the second order perturbation theory gives the *effective-mass Hamiltonian*

$$H = \frac{(-i\hbar\nabla + e\vec{A})^2}{2m_n^*} + V(\vec{r}) + \frac{g_n^*}{2}\mu_B \vec{\sigma} \cdot \vec{B} \tag{D.18}$$

where we have assumed a nondegenerate, isotropic, parabolic band, for simplicity.

Appendix E

The Schrödinger-Poisson problem

E.1 Electrostatic doping

The charge transferred at the interface by applying the external electric field can be calculated assuming that the LXO/STO heterostructure behaves as a plane capacitor, where the role of the plates are played by the top (back) gate electrode and the 2DEG respectively.

In a top top gating configuration, the charge transferred at the interface by the external voltage is thus given by

$$\delta n = \varepsilon_0 \varepsilon_{LXO} \frac{V_g}{d},$$

where d is the thickness of the LXO layer, ε_0 the vacuum dielectric constant and $\varepsilon_{LXO} \sim 20$ the LXO one.

In the back gating case, the transferred charge δn is a non linear function of the gating. This happens because in the low temperature region[1], the dielectric constant of STO is a highly non-linear function of the electric field of the form

$$\varepsilon_{STO}(E) = \varepsilon_\infty + \frac{1}{A + B|E|}$$

where ε_∞ is the saturation value for very hight field, $A \sim 4 \times 10^{-5}$ and $B \sim 5 \times 10^{-10} [mV^{-1}]$ are temperature dependent parameters and $|E|$ is the amplitude of the electric field.

In order to calculate the transferred charge $\delta n(V_g)$, one has to integrate the capacitance per unit surface $\varepsilon_0 \varepsilon_{STO}/d$ from zero voltage to V_g, getting the expression

$$\delta n = \frac{\varepsilon_0 a^2}{e} \left[\frac{\varepsilon_\infty V_g}{d_S} + \frac{V_g}{B\left|V_g\right|} \log\left(1 + \frac{B\left|V_g\right|}{A d_S}\right) \right]$$

---

[1] We solved the Schrödinger-Poisson equations only for $T = 0$.

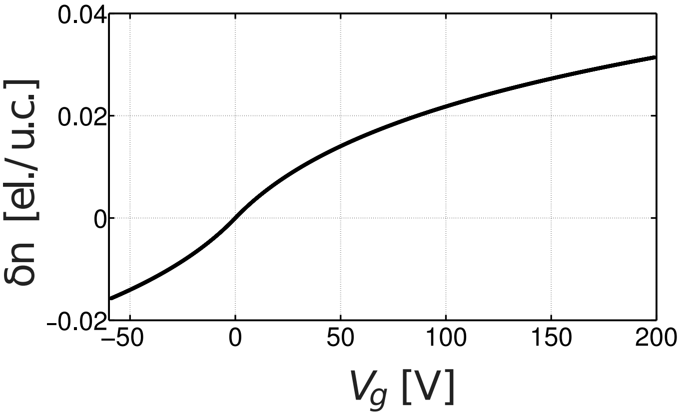

Fig. E.1 Field-effect charge modulation in the STO bulk as a function of gate voltage.

where A and B are those given above. δn as a function of V_g is plotted in figure E.1.

E.2 Schrödinger-Poisson equations for the self-consistent electronic well

A well-tested approach to an eigenvalue problem in electronic quantum wells at the interface of two semiconductors is reported in [46]. It consist in the simultaneous solution of the coupled Poisson and Schrödinger (in the effective mass approximation) equations

$$\left[\frac{\hbar^2}{2m^z_\alpha}\frac{d^2}{dz^2}+e\phi(z)+\varepsilon_{i\alpha}\right]\zeta_{i\alpha}(z) \;=\; 0, \quad i=1,2,3,... \tag{E.1}$$

$$\frac{\varepsilon_0 a^2}{e}\frac{d}{dz}\left[\varepsilon_r(E)\frac{d}{dz}\phi(z)\right] \;=\; n(z) \tag{E.2}$$

which gives us both the eigenfunctions and the confining potential well. The index $\alpha = xy, xz, yz$ labels the three Ti t_{2g} orbitals, d_{xy}, d_{xz}, d_{yz}, where the electrons mostly reside. The full 2D band structure is

$$\varepsilon_{i,\alpha,k} = \frac{\hbar^2 k_x^2}{2m^x_\alpha} + \frac{\hbar^2 k_y^2}{2m^y_\alpha} + \varepsilon_{i\alpha}.$$

The sub-band level $\varepsilon_{i\alpha}$ includes an energy offset Δ_α splitting the various t_{2g} levels. Taking $\Delta_{xy} = 0$ as a reference level, the energy offset $\Delta_{xz,yz} \equiv \Delta$ of the $d_{xz,(yz)}$ bands is experimentally found to be $\Delta \approx 50\,\text{meV}$ [90]. Similar values are found in first-principle calculations between the highest occupied d_{xy} sub-band and the lowest $d_{xz,yz}$ sub-bands [106]. Here we have to adjust $\Delta \approx 0-10\,\text{meV}$ in order to self-consistently obtain the energy difference between the d_{xy} and the $d_{xz,yz}$ sub-bands of order $50-60\,\text{meV}$, showing that the energy offset mostly

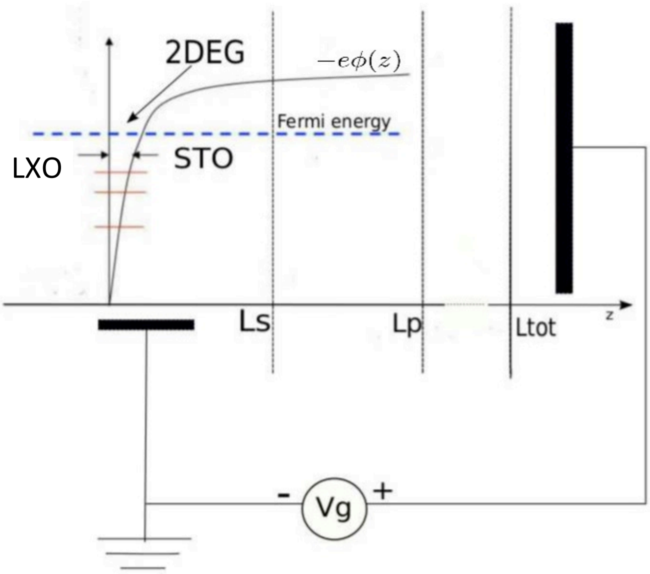

Fig. E.2 Schematic view of the back-gating configuration in LXO/STO.

arises from the different mass along the z direction. We take the masses of the various bands as $m_{xy}^{x,y} = m_l$, $m_{xy}^{z} = m_h$; $m_{xz}^{x,z} = m_l$, $m_{xz}^{y} = m_h$; $m_{yz}^{y,z} = m_l$, $m_{yz}^{x} = m_h$.

The close analogy between semiconductors and oxide interfaces allows us to apply this method to the LXO/STO potential as well. The boundary conditions for the set of equations (E.1)-(E.2) can be understood considering the schematic picture of the interface shown in figure (E.2) for the back-gating case. Within this approach, the electric field and the displacement field are by symmetry only directed along the z axis. Therefore henceforth we will indicate with E and D the z components of the fields.

The energy difference between the LXO and STO conduction band edges is about 1 eV, so that in the low-filling regime it is safe to approximate the potential step at the LXO/STO interface as an infinite energy barrier. In addition the eigenfunctions have to be normalizable, therefore we are led to set of boundary conditions

$$\zeta_{i\alpha}(0) = 0, \qquad \zeta_{i\alpha}(\infty) = 0. \tag{E.3}$$

The second condition can be implemented numerically exploiting the fact we are dealing with a confining potential: in a region far enough from the interface the eigenfunctions are exponentially decreasing. Taking a distance from the interface L_s well inside this region, the set (E.3) can be replaced by

$$\zeta_{i\alpha}(0) = 0, \qquad \zeta_{i\alpha}(L_s) = 0. \tag{E.4}$$

The boundary conditions for the Poisson equation depend on both the (positive) countercharges left in the LXO valence band and on the gating voltage. Experimental evidences show that the width of the 2DEG is only few nanometers, while the trapped charges extend over a few tens of nanometers [9, 11]. If L_p is the thickness of the region in which all the charge is confined, we can solve the Poisson equation analytically in the interval (L_p, L_{tot}) and find appropriate boundary conditions by the reasoning reported below. We take $L_p = 100$ nm, that is large enough to consider also long-tail distributions of the trapped charges.

We first discuss here the case of back-gating (see figure E.2). Let us consider the interval $[0^-, +\infty)$. For the solution of the Poisson Equation in the region $z > 0$ where the 2DEG resides, the precise distribution and extension of the positive countercharges on the LXO side is immaterial: they can be at the topmost layer of LXO in the case of the polar catastrophe reconstruction or they can be homogeneously distributed in the LXO layer if they are given by the oxygen vacancies. In both cases their electric field in $z > 0$ only depends on their density projected on the interface. For simplicity we therefore assume in both cases that the countercharges are located on the $z = 0^-$ plane. Thus the overall charge contained in the $[0^-, +\infty)$ region is zero and the system is neutral neutral and we can reasonably impose the condition

$$E(-\infty) = E(+\infty) = 0 \tag{E.5}$$

on the electric field, for any gating potential V_g. In $[0^+, +\infty)$ the neutrality does no longer hold, because the positive charges are now excluded. Thus the electric field verifies the condition

$$\int_{0^+}^{+\infty} dz \frac{d}{dz}(\varepsilon_r E) = +\frac{en_0}{a^2\varepsilon_0} \Rightarrow \varepsilon_r(0^+)E(0^+) = -\frac{en_0}{a^2\varepsilon_0} \tag{E.6}$$

where n_0 is the density of the positive countercharges per interfacial unit cell and we have used Eq. (E.8) to cancel the term $\varepsilon_r(+\infty)E(+\infty)$. Since all the electronic charges (mobile $n^m = n_0^m + \delta n$, and trapped n_0^t) are between 0^+ and L_p, the electric field in $z \in (L_p, L_{tot})$ is uniform even for the non linear experimental form of the relative dielectric constant of STO, $\varepsilon_r = (A + B|E|)^{-1} + \varepsilon_\infty$, [$A$, B and ε_∞ are experimentally measured constants [76]]. The

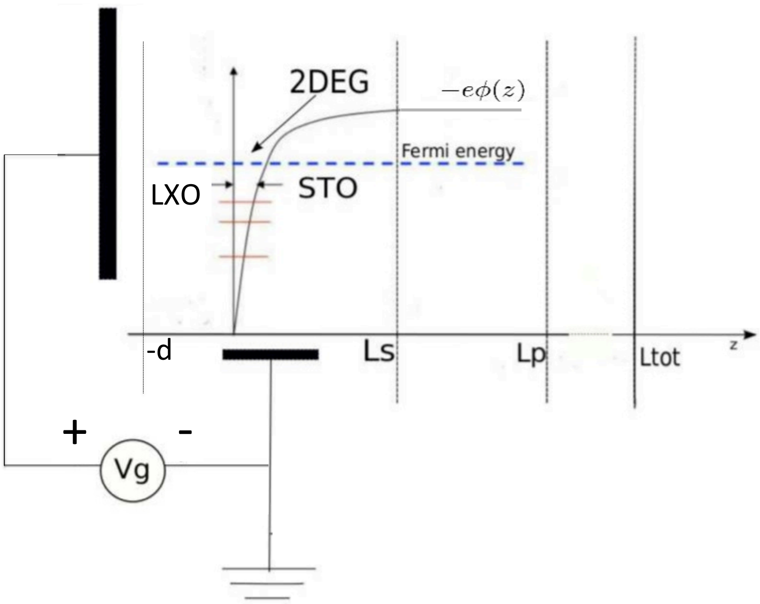

Fig. E.3 Schematic view of the top-gating configuration in LXO/STO.

boundary value for the potential thus reads

$$\phi(L_p) = \frac{V_g}{L_{tot}} L_p, \tag{E.7}$$

where V_g is the external gating.

We now move to the discussion of the top-gating case (see figure E.3). Let us consider the interval $[0^-, +\infty)$. For the solution of the Poisson Equation in the region $z > 0$ where the 2DEG resides, the precise distribution and extension of the intrinsic positive countercharges on the LXO side is again immaterial, and for convenience we still suppose them to be confined on an infinitely thin layer at $z = 0^-$. The free charges of the metallic electrode of the gate are now located on a layer at $z = -d$, where d is the thickness of the LXO layer. Thus the overall charge contained in the $[-d, +\infty)$ region is zero and the system is neutral and we can reasonably impose the condition

$$E(-\infty) = E(+\infty) = 0 \tag{E.8}$$

on the electric field, for any gating potential V_g. In $[0^+, +\infty)$ the neutrality no longer holds, because the positive charges and the charges on the gating electrode are now excluded. Thus the electric field verifies the condition

$$\int_{0^+}^{+\infty} dz \frac{d}{dz}(\varepsilon_r E) = +\frac{e(n_0 + \delta n)}{a^2 \varepsilon_0} \Rightarrow \varepsilon_r(0^+)E(0^+) = -\frac{e(n_0 + \delta n)}{a^2 \varepsilon_0} \tag{E.9}$$

where n_0 is again the density of the intrinsic positive countercharges per interfacial unit cell, while $\delta n = 2ea^2 \varepsilon_0 \varepsilon_{LXO} V_g/(ed)$. Again we used Eq. (E.8) to cancel the term $\varepsilon_r(+\infty)E(+\infty)$. Since all the electronic charges (mobile $n^m = n_0^m + \delta n$, and trapped n_0^t) residing between 0^+ and L_p, compensate the charges on the LXO side (both the intrinsic countercharges and the charges in the electrode), the system looks neutral in the (L_p, L_{tot}) region and the electric field vanishes. The boundary value for the potential thus reads

$$\phi(L_p) = 0. \tag{E.10}$$

E.2.1 Numerical solution

Because of the nonlinear behavior of (E.1)-(E.2), an analytic approach is not viable and we adopted a numerical iterative procedure to perform the calculation through the following steps:

- The starting point is the potential at the *nth* iteration, $\phi_n(z) = \phi_{old}^n(z)$, and its derivative, the electric field $E_n(z) = E_{old}^n(z)$, $z \in [0, L_s]$. We solve Eq. (E.1) using a Finite Element Method (*FEM*) algorithm [86] (but also see appendix C), finding the energies $\varepsilon_{i\alpha}$ and the eigenfunctions $\zeta_{i\alpha}$, which verify the conditions (E.4). We recall that L_s has to be taken far enough from the interface to ensure that the eigenfunctions are in a region in which they have an evanescent behavior. This can be done choosing different values for L_s and checking them *a posteriori*. The envelope functions are normalized imposing the condition $\int_0^{L_s} |\zeta(z)|^2 dz = 1$.

- From the knowledge of the eigenvalues, the Fermi level can be calculated inverting numerically (e.g, using a bisection method) the relation $n^m = \int_{-\infty}^{\varepsilon_F} g(\varepsilon) d\varepsilon$, and from $n^m(z) = \sum_{i\alpha} |\zeta_{i\alpha}(z)|^2 \int_{-\infty}^{\varepsilon_F} d\varepsilon\, g_{i\alpha}(\varepsilon)$ we have the density profile along z of the 2DEG. Here only the mobile electrons contribute to define the Fermi energy since the trapped charges reside in impurity levels, deep or localized enough to be safely considered as a stable quenched charge distribution.

- The profile of the potential well is found once one knows both the distribution of the 2DEG and the trapped (negative) charges. While the first is calculated self-consistently, the second is fixed once for all at the zero*th* step. There are no experimental evidences that determine univocally the distribution of the trapped charges, but a reasonable choice is a decreasing exponential distribution of the form

$$n_0^t(z) = \left(\frac{n_0^t}{\lambda}\right) e^{-\frac{z}{\lambda}}. \qquad \text{(E.11)}$$

Its shape is controlled by two parameters: the decay length λ and the maximum value n_0^t/λ.

- The Poisson equation is solved in the interval $[0^+, L_p]$. This gives a new potential $\phi(z) = \phi_{new}^n(z)$ and a new electric field $E(z) = E_{new}^n(z)$.
- The update at the next step is performed defining the quantities

$$\begin{aligned} \phi_{n+1}(z) &= s\phi_{old}^n(z) + (1-s)\phi_{new}^n(z) \\ E_{n+1}(z) &= sE_{old}^n(z) + (1-s)E_{new}^n(z) \end{aligned}$$

where the parameter $s \in [0,1]$ is used to control the difference between the old potential and the new one; this reduces the risk that the iterative procedure escapes from the self-consistent solution and does not converge. The calculation stops as soon as the condition

$$\int_0^{L_p} |\phi_{n+1} - \phi_n|^2 dz < \delta \qquad \text{(E.12)}$$

is fulfilled, for a suitably chosen accuracy δ.

Through the previous five steps we obtain the potential well $V(z) = -e\phi(z)$ (with the corresponding Fermi energy ε_F), the electric field $E(z)$ and the density $n^m(z)$ of the 2DEG for a given value of n_0.

In principle the numerical solution may depend on the choice of the error δ in (E.12), the initial potential $\phi_0(z)$ and the discretization length (according to the standard FEM, we discretized in N_{elem} intervals the region in which we solve the Schrödinger equation. See appendix C). We performed different tests to ensure the reliability of the numerical solution. In order to exclude the dependence on the initial potential, we varied the initial condition ϕ_0 in a reasonable class of functions and kept n_0 and V_g fixed. We find that the numerical solution is stable with respect to the initial data. N_{elem} and δ has been fixed to reach the uniform convergence. The solution is almost independent of δ while the choice of the first parameter is critical to obtain the uniform convergence. In our work we took N_{elem} so that

$\sup_{n_0} |\varepsilon_F(N_{elem}+1) - \varepsilon_F(N_{elem})|$ is of order $\approx 10^{-5}$, a suitable request to reduce the error under the typical variations ($\sim 10^{-3}$ eV) of the chemical potential $\mu(n)$.

E.3 Electrostatic energy

The chemical potential of the system is defined as

$$\mu = \mathscr{E}(N+1) - \mathscr{E}(N) \approx \partial_N \mathscr{E}$$

where N represents the number of electrons and $\mathscr{E} = \mathscr{E}_{sp} + \mathscr{E}_{es} + \mathscr{E}_{sr}$ is the total energy. Here, $\mathscr{E}_{sp}$ is the purely quantum contribution of the mobile electrons, $\mathscr{E}_{sr}$ the energy cost arising from the short range interaction between positive countercharges in the LXO side (see caption of figure 3.3), and $\mathscr{E}_{es}$ is the purely classical electrostatic term.

While the previous section solved the quantum problem of electrons in a self-consistent potential, here we provide details of the calculation of the other electrostatic contributions to the total energy of the system arising form the fixed charges (the countercharges, the charges on the gating electrodes, and the charges trapped in the impurity states inside the STO) and from the mobile charges at the interface.

We consider two possible gating configurations. For the back-gating, the near region is the interval $z \in [0, L_p]$, while the far region is the $(L_p, L_{tot}]$ interval. On the other hand, for the top-gating, while the so-called near region is the same, the “far” (actually not so far) region corresponds to the LXO side of the heterostructure, i.e. to the $[-d, 0)$ interval, d being the thickness of the LXO slab.

In the near region (which is the same both for the top- and back-gating cases) we solve the Poisson equation

$$\frac{d}{dz} D(z) = n^m(z) + n_0^t(z) \tag{E.13}$$

to find the electric displacement field $D(z) = D^m(z) + D^f(z)$ due to the mobile and fixed charges. In this region the only fixed charges are those trapped on the STO side, while the charges on the electrodes and the countercharges on the LXO side only enter as boundary conditions. Due to the non-linear character of the STO dielectric constant, the electric field reads

$$\begin{aligned} E &= \frac{-\operatorname{sgn}(D)\,[1+\varepsilon_\infty A - \operatorname{sgn}(D) BD]}{2B\varepsilon_0\varepsilon_\infty} \\ &+ \frac{\sqrt{[1+\varepsilon_\infty A - \operatorname{sgn}(D) BD]^2 + \operatorname{sgn}(D) 4\varepsilon_\infty ABD}}{2B\varepsilon_0\varepsilon_\infty}. \end{aligned} \tag{E.14}$$

The total electric displacement field is obtained by numerically integrating Eq.(E.13), while the field due to the fixed charges is analytically found from

$$\frac{d}{dz}D^f(z) = n_0^t(z). \tag{E.15}$$

The result is

$$D^f(z) = -\frac{-en_0^t}{2a^2}\left(1-2e^{-\frac{z}{\lambda}}\right)+\frac{en_0}{2a^2}-\frac{e\delta n}{2a^2} \tag{E.16}$$

Once D and D^f are known, the electric displacement due to the mobile charges is obtained from $D^m = D - D^f$. The electric fields of the fixed and mobile charges are

$$E^{f,m} = \frac{D^{f,m}}{\varepsilon_0}\frac{A+B|E|}{1+\varepsilon_\infty(A+B|E|)}. \tag{E.17}$$

Notice that the non-linearity of ε_r entails the dependence of $D^{f,m}$ and $E^{f,m}$ on the total electric field $E = E^f + E^m$ given by Eq. (E.14).

In the far region we have different expressions for the top- and back-gating configurations. For the latter the far region coincides with the bulk of the STO substrate, where

$$D^m(z) = \frac{en_0^t}{2a^2}-\frac{e\delta n}{2a^2}-\frac{en_0}{2a^2}, \tag{E.18}$$

$$D^f(z) = -\frac{en_0^t}{2a^2}+\frac{en_0}{2a^2}-\frac{e\delta n}{2a^2} \tag{E.19}$$

are constant. The corresponding electric fields are then obtained by solving Eqs. (E.14) and (E.17).

The far region in the top-gating configuration is instead given by the whole LXO side, where the dielectric constant ε_{LXO} is really constant so that

$$E^m(z) = \frac{e\delta n}{2\varepsilon_0\varepsilon_{LXO}a^2}-\frac{en_0^t}{2\varepsilon_0\varepsilon_{LXO}a^2}+\frac{en_0}{2\varepsilon_0\varepsilon_{LXO}a^2}, \tag{E.20}$$

$$E^f(z) = \frac{e\delta n}{2\varepsilon_0\varepsilon_{LXO}a^2}+\frac{en_0^t}{2\varepsilon_0\varepsilon_{LXO}a^2}-\frac{en_0}{2\varepsilon_0\varepsilon_{LXO}a^2}. \tag{E.21}$$

E.4 Importance of the trapped charges for the numerical convergence

In the model used here to describe the interface, a relevant role is played by the trapped charges. We already mentioned (see 1.5.1) that there are experimental evidences of the presence of trapped electrons in the region around the STO interface. One more reason to add them to the model is hidden in the role they play in the numerical calculation itself, since they seem to be necessary to find a stable solution of the Poisson equation, especially at positive grid tensions. In fact, if we consider only the gas, at $V_g = 0$ the Poisson equation imposes the Fermi level to be just on the top of the potential, at the maximum value of the conduction band. This solution is highly unstable, thanks to the presence of quasi-bounded states whose eigenfunctions are extended far from the LXO-STO junction: as soon as the gate tension becomes positive the electrons escape from the well toward the electrode in the STO side, so that the calculation can not converge[2]. This reflects the fact that the trapped charges, far from being a purely mathematical trick, actually arise from the escaping of charges after a first (positive) polarization of the grid: when the well is completely filled at $V_g = 0$, the addition of more charges causes a leak of electrons towards the impurity levels, increasing the number of trapped charges.

Since the parameters A and λ, describing the distribution of trapped charges, are experimentally unknown, we decided to fix them to a value that simultaneously ensures the stability of the self-consistent procedure up to the maximum gate voltage reached experimentally, an interfacial electric field of $\sim 10^8 V/m$ and a gas extension compatible with experimental evidences [32, 21].

In the light of an hysteretical behavior of the 2DEG's resistance (see 1.5.1), the choice of a unique gating-independent distribution for the trapped charges corresponds to a description of the system after a preliminary sweep of the gate potential, from $V_g = 0V$ to $V_g = +200V$, when the external voltage is decreased from the maximum value to the minimum one and the resistance increases (see figure 1.13 of chapter 1).

---

[2] Otherwise it converges to a non-physical solution.